

12-2021

GaAs Growth on Sapphire Substrates (C and R Plane) for Integrated Microwave Photonics (IMWP)

Samir Kumar Saha
University of Arkansas, Fayetteville

Follow this and additional works at: <https://scholarworks.uark.edu/etd>



Part of the [Condensed Matter Physics Commons](#), and the [Optics Commons](#)

Citation

Saha, S. K. (2021). GaAs Growth on Sapphire Substrates (C and R Plane) for Integrated Microwave Photonics (IMWP). *Graduate Theses and Dissertations* Retrieved from <https://scholarworks.uark.edu/etd/4347>

This Dissertation is brought to you for free and open access by ScholarWorks@UARK. It has been accepted for inclusion in Graduate Theses and Dissertations by an authorized administrator of ScholarWorks@UARK. For more information, please contact uarepos@uark.edu.

GaAs Growth on Sapphire Substrates (C and R Plane) for Integrated Microwave Photonics
(IMWP)

A dissertation submitted in partial fulfillment
of the requirements for the degree of
Doctor of Philosophy in Physics

by

Samir Kumar Saha
University of Dhaka
Bachelor of Science in Physics, 2011
University of Dhaka
Master of Science in Physics, 2013

December 2021
University of Arkansas

This dissertation is approved for recommendation to the Graduate Council.

Gregory J. Salamo, Ph.D.
Dissertation Director

Shui-Qing (Fisher) Yu, Ph. D.
Committee member

Hugh Churchill, Ph. D.
Committee member

Huaxiang Fu, Ph. D.
Committee member

Abstract

The microwave signal processing in the optical domain creates new opportunities for information and communication technology (ICT) and networks by increasing speed, bandwidth, and processing capability. IMWP incorporates the functions of microwave photonics components/subsystems in monolithic or hybrid photonic circuits to meet future needs. Sapphire platforms have the potential to integrate all-in-one, for instance, light source, analog signal processing, light detection, CMOS control circuit, silicon on sapphire to achieve high-performance, low-cost mixed-signal optical links etc. Molecular beam epitaxy (MBE) has been used to grow GaAs on sapphire substrates to integrate optoelectronic devices in the same platform.

The initial stage of GaAs thin film growth has been investigated extensively in both c and r plane sapphire substrates. Direct growth of GaAs on both sapphires results in three-dimensional (3D) islands. In c-plane sapphire, 50% twin volume of GaAs islands, and in r-plane sapphire, two primary domains of GaAs islands are observed. A strong interaction between the growth of GaAs on r-plane sapphire is observed than the growth of GaAs on c-plane sapphire. A thin AlAs nucleation layer improves the wetting of both substrates. After inserting the AlAs nucleation layer, in c- plane sapphire, twin volume is reduced to 16%, and in r-plane sapphire twin is introduced. Further, we investigated the effect of growth temperature, pre-growth sapphire substrate surface treatment, and in-situ annealing on the quality of GaAs epilayer on c-plane sapphire substrates. We have been able to reduce the twin volume to below 2% and an XRD rocking curve linewidth to 223 arcsec in a c-plane sapphire substrate.

To grow high quality GaAs (111)A buffers on an atomically flat sapphire substrate, a two-step growth method has been introduced where, at an early stage, a GaAs layer has been grown at low

temperature, followed by a second high-temperature GaAs growth layer. In addition to the two-step process, an AlAs nucleation layer and multiple annealing steps have been employed. Relaxed, smooth surface morphology and high-quality GaAs is achieved with the presence of the LT GaAs layer. A two-dimensional InGaAs quantum well (QW) was epitaxially grown on the 70 nm GaAs buffer and compared with a reference to two-dimensional InGaAs QW grown on GaAs (111)A substrate. Along with X-ray and high-resolution cross-section transmission electron microscopy, comparable QW photoluminescence intensity and linewidth confirmed our growth strategies effectiveness to produce high-quality GaAs on sapphire.

The film thickness was improved up to almost 500 nm by changing the growth parameters such as growth temperature and annealing temperature. We have achieved the room temperature (RT) photoluminescence. The 16 μm microdisk laser was fabricated on GaAs/sapphire system and characterize by micro-PL measurements. The lasing was not successful. The higher surface roughness needs to be optimized to get lasing. We will fabricate GaAs/sapphire QW for electrically pumped laser and realize the photonic chip on the sapphire platform in a long-term goal.

©2021 by Samir Kumar Saha
All Rights Reserved

Acknowledgment

First and foremost, praise and felicitation to the eternal and most gracious God for showering His blessings and kindness throughout my research work to complete the research successfully.

I would like to express my highest gratitude and appreciation to my research advisor, Dr. Gregory J. Salamo, for his continuous support, motivation, and invaluable guidance throughout the research. His deep knowledge of basic science and research inspired me a lot. The discussion between us always gave me the courage to face challenging tasks during my research work. It was a great privilege and honor for me to work and study under his guidance. I would also like to thank him for his amity, empathy, and great sense of humor. My sincere thanks also go to my research committee members Dr. Shui-Qing(Fisher) Yu, Dr. Huaxianfg Fu, and Dr. Hugh Churchill, for upholding me with their valuable guidance, inspiration, and feedback to improve my research work.

A special thanks to Dr. Rahul Kumar, a post-doctoral fellow, who has an excellent support and significant impact on my research work. It was a pleasure for me to work with my UHV-MBE growth fellows Dr. Pijush K. Ghosh, Dr. Chen Li, and Mohammad Zamani Alavijeh. Together, we maintained the UHV-MBE system clean and free from contamination to produce high-quality samples. The quality time we spent in or outside the lab, is ever rememberable. Thanks to Krishna Pandey, and Rafique Un Nabi Roni for helping me use their lab furnace for the substrate annealing. I would like to extend my thanks and respect to Dr. Mourad Benamara, Dr. Andrian Kuchuk, and Dr. Yuri Mazur from the institute for Nanoscience and Engineering for teaching me how to make sample preparation and how to operate it independently photoluminescence setup, x-ray diffraction machine, and transmission and scanning electron microscope.

I am grateful to my parents for their continuous support, prayers, love, and sacrifices for taking care of me to achieve my desired success. I would like to take the special privilege to thank my elder brothers and sisters for keeping faith on me. Without their support, it would not have been possible for me to reach this point. Apart from them, there are many others who have also helped me in difficult times in different ways; I apologize for having a little scope to mention the names one by one, but I would like to express my heartfelt gratitude to all of them on this occasion.

Last but not least, I would like to express special thanks to my beautiful wife for her constant support, caring, love, and believing in me. Without her, I would not have had the courage to face the hardest difficulties during my graduate life and become a better scientist.

Table of Contents

Chapter 1: Introduction	1
1.1 Integrated Microwave photonics	1
1.2 Motivation	4
1.3. Background	6
1.3.1 GaAs	6
1.3.2 Optical properties	8
1.3.3 Sapphire	9
1.4 GaAs growth on sapphire.....	12
Chapter 2: Crystal growth and Growth techniques	14
2.1 Epitaxy	14
2.1.1 Homo and heteroepitaxial systems.....	14
2.2 Thin film growth modes.....	16
2.3 Molecular Beam Epitaxy	19
2.3.1 Reflection high energy electron diffraction (RHEED).....	21
2.3.2 Substrate temperature measurement.....	24
Chapter 3: Characterization Method.....	26
3.1 Structural material measurement	27
3.1.1 Atomic force microscopy (AFM).....	27
3.1.2 X-ray diffraction (XRD).....	29
3.1.3 Transmission electron microscopy (TEM).....	31
3.2 Optical characterization	34
3.2.1 Raman Spectroscopy	34

3.2.2 Ellipsometry	36
3.2.3 Photoluminescence	40
3.3 Device Fabrication	43
3.3.1 GaAs Microdisk Fabrication on Al ₂ O ₃ (0001)	43
Chapter 4: Results and discussion.....	46
4.1 GaAs growth on c plane sapphire	46
4.1.1 Introduction	46
4.1.2 Direct growth of GaAs/Sapphire	49
4.1.3 Introduction of thin AlAs nucleation layer.....	56
4.1.4 Effect of Pre-growth Substrate Surface Treatment	59
4.1.5 Effect of growth temperature	62
4.1.6 Effect of in-situ annealing	64
4.2 Two-step growth	68
4.2.1 Surface characterization	71
4.2.2 Structural characterization.....	75
4.2.3 Photoluminescence (PL).....	80
4.3 Thickness Optimization	82
4.3.1 Growth temperature variation	82
4.3.2 Effects of annealing.....	86
4.3.3 Micro disk laser characterization	90
4.4 GaAs growth on R-plane sapphire	93
4.4.1 Comparison of GaAs growth on c and r-plane sapphire	96
4.4.2 Effect of growth temperature on GaAs/r-plane sapphire	99

4.4.3 Introduction of AIAs layer	102
Chapter 5: Conclusions and Future work	106
5.1. Conclusions.....	106
5.2. Future work.....	108
References.....	109

List of Figures

Figure 1: Integrated microwave photonics system [11]	2
Figure 2: Three platforms for integrated microwave photonics (a) silicon-on-insulator (SOI) for programmable signal processor [20], (b) indium phosphide for all-integrated tunable filter [20], and (c) silicon nitride for high spectral resolution bandpass filter [21].	3
Figure 3: Sapphire based 3D integrated microwave photonics architecture.....	4
Figure 4: A comparison of refractive index and absorption coefficient for Si_3N_4 , Al_2O_3 , and SiO_2 [22].	5
Figure 5: FCC unit cell of GaAs crystal structure.	6
Figure 6: GaAs crystal planes (a) (001); (b) (111); (c) (110).	7
Figure 7: Energy band diagram of GaAs [31].	9
Figure 8: (a) Schematic of the arrangements of Al^{3+} and O^{2-} layers in sapphire [32]; (b) sapphire unit cell and different crystal planes [33].	10
Figure 9: Basal or C- plane sapphire substrate.	11
Figure 10: R-plane sapphire substrate [38]......	11
Figure 11: Schematic representation of (a) lattice- matched, (b) strained, and (c) relaxed (misfit dislocation) epitaxial growth.....	16
Figure 12: Schematic illustration of three growth modes. (a) Frank-Van der Merwe, (b) Volmer-Weber, and (c) Stranski-Krastanov. Substrate (overlayer) atoms are shown in grey (red) where the lighter red is on the first adsorbate layer. Θ represent the amount of deposited material ($\Theta=1$ represent one monolayer deposited atom on substrate atom) [44].	17
Figure 13: Surface energies and angle between islands and substrate.....	19
Figure 14: Three MBE chambers are connected by transfer line [55]......	21
Figure 15: (a) An illustration of the reciprocal lattice roads of the 2D sample surface, perpendicular to atom rows. The intersection of the reciprocal lattice planes with Ewald's sphere, (b) streaky RHEED image from the 2D surface. (c) a static streaky RHEED image [64].	23
Figure 16: Schematic illustration of laser, tip, and photodiode in AFM system [74]......	28
Figure 17: PANalytical X'Pert MRD diffractometer situated at University of Arkansas.....	30

Figure 18: A schematic diagram of the geometrics of thin film X-ray diffraction measurement, showing relations between the lattice planes of a thin film sample and x-ray geometrics [79]. ..	31
Figure 19: Schematic diagram of (a) HR-TEM imaging mode, (b) HAADF-STEM imaging mode [83]......	33
Figure 20: Different steps of TEM sample preparation. (a) A small rectangular piece of sample; (b) face to face gluing; (c) mechanical polishing; (d) small hole generation by ion milling; (e) birds eye view of the hole and transparent areas around it [86].	34
Figure 21: Three types of scattering that can occur when light interacts with a molecule.	35
Figure 22: Schematic diagram of the Raman setup with 532 nm and 632 nm laser.....	36
Figure 23: Schematic diagram of Ellipsometry basic concept. The refractive index of the sample influences the transmission of light.	38
Figure 24: Experimental and model fitting ellipsometry data of GaAs/AlAs/sapphire sample. ..	40
Figure 25: Graphical presentation of energy states, band gap and three recombination process. 41	
Figure 26: Schematic diagram of PL system setup. Two optical sources, detectors, beam alignment for both room temperature and low temperature measurements are illustrated and is not in scale.	43
Figure 27: Four main steps of GaAs microdisk laser fabrication on sapphire substrate: (1) 1.8 μm AZ 4110 photoresist by spin coating; (2) pattern photoresist by optical lithography and developing; (3) wet etching by H_2SO_4 : H_2O_2 : H_2O =1:5:8 solution; (4) photoresist removed by acetone cleaning.	44
Figure 28: The optical image of (a) a small surface area after fabricating 16 μm micro disk lasers, red circles indicate the position of the disk, the rectangular boxes and long arms are for finding the position of the disks during measurements, (b) a 16 μm micro disk laser.....	45
Figure 29: Schematic diagram of (a) heteroepitaxial, and (b) dissimilar epitaxy systems [108]	47
Figure 30: (a) AFM image of annealed sapphire substrate with prominent steps and terraces are shown; (b) line profiles of the image.	48
Figure 31: RHEED images (a) from atomically flat sapphire substrate; after (b) 1 nm, (c) 10 nm, and (d) 50 nm GaAs deposition.	50
Figure 32: AFM images of samples (a) 1 nm GaAs, (b) 10 nm GaAs, and (c) 50 nm GaAs.	52

Figure 33: (a) out of plane measurements of 50 nm GaAs (b) FWHM of (111) rocking curve versus GaAs thickness (c) Low-temperature PL from 50 nm GaAs (C50). This indicated improved crystal quality with increased growth and using an AlAs 5 nm nucleation layer (in red) discussed below.

..... 54

Figure 34: phi scan of (a) (10.4) plane of sapphire and (b) (220) plane of GaAs/Sapphire (C50) and (c) GaAs/AlAs/Sapphire (S1). This indicates reduced twinning with an AlAs 5 nm nucleation layer..... 55

Figure 35: Real time growth study from sample S1 during (a) AlAs growth, (b) GaAs growth on sapphire (original phase is referred by “O” whereas twin phase is referred by “T”), and (c) different RHEED spots identified for corresponding crystal planes of GaAs (111) growth. Both (a) and (b) RHEED patterns indicate twinning. RHEED spots in rectangle do not belong to GaAs (111) orientation. 57

Figure 36: Columns show the data for (a) corrugated surface sample, (b) weakly defined step-terrace surface sample, and (c) well-defined step-terrace surface sample. Row (I) is an AFM image of the initial sapphire substrate; Row (II) is an AFM images of the GaAs film; Row (III) is the RHEED pattern after AlAs growth, while Row (IV) is the RHEED pattern after GaAs growth. Both (a) and (b) RHEED patterns indicating twinning, while the RHEED pattern in (C) indicate that twinning is absent only for AlAs (row III) growth. 60

Figure 37: (a) phi-scan, (b) (111) omega-2theta scan, and (c) (111) omega-scan of samples grown on the different starting substrate surfaces. Inset in the Figure 37(c) shows the Gaussian fitting of omega-scan of S1 into two peaks having different broadness. 62

Figure 38: AFM images of GaAs samples grown at three different growth temperature (a) 600°C (T1), (b) 550°C (T2) and (c) 500°C (T3). 63

Figure 39: (a) (220) phi-scan, (b) (111) omega-2theta scan, and (c) (111) omega-scan of samples grown on different growth temperatures. 64

Figure 40: RHEED pattern from sample A1 (a) after the GaAs growth and (b) after in-situ annealing; 5 μm x 5 μm AFM image of (c) 50 nm GaAs (S50), (d) after in-situ annealed sample (S50-annealed) (e) 1 μm x 1 μm AFM images of the in-situ annealed sample. Symbol “*” shows a triangular pit whereas symbol “#” shows an irregular shape pit. 66

Figure 41: Phi scan of (10.4) plane of Sapphire and (220) plane of 50 nm GaAs sample (S50) and in-situ annealed sample (S50-annealed). 67

Figure 42: (a) High-resolution cross-sectional TEM image of the In_{0.78}Ga_{0.22}As/ LT-InGaAs/GaAs interface regions, (b) dislocation bending is shown by green, red and yellow lines, (c) a brief schematic model of dislocation bending [143]. 69

Figure 43: Schematic diagrams of misfit dislocations generation. Left: defects are introduced before the island's coalescence. Right: defects are introducing after the island's coalescence [41].
..... 70

Figure 44: (a) Schematic diagram of sample structure presented in this work; (b) schematic structure of InGaAs QW. 71

Figure 45: AFM images (5 μm x 5 μm) of (a) S1, (b) S2, (c) S3; RHEED images along [110] direction of GaAs (d) after growth of entire structure of S1 and S2, 0th, 1/2th and 1st order RHEED streaks are marked, longer broken lines show the integer-order RHEED streaks whereas shorter broken lines show fractional-order RHEED streaks; and (e) after growth of S3, spots riding on streaks can be seen, few spots are shown by arrows..... 72

Figure 46: Ehrlich-Schwoebel barrier shows the high-energy barrier at the step..... 73

Figure 47: Side view of GaAs (111) A surface. In the (111) A plane each surface Ga atom bonded to the bulk crystal with three bonds and As atom bonded with only one bond to the bulk GaAs. For the (100), Ga and As are bonded to the bulk GaAs with two bonds..... 74

Figure 48: (a) Omega/2theta scan of samples grown with three different LT layer thickness', GaAs peak is centered at same 2 θ angle to show the shape variation and fringes of GaAs (111) plane diffraction peak in three samples; (b) (111) symmetric Omega/2theta scan showing the shift of GaAs (111) peak with respect to sapphire (0006) peak; (c) Raman spectra of these samples with homoepitaxial GaAs (111)A sample, arrows pointing the GaAs longitudinal optical (LO) phonon peaks of these three samples show the gradual shift of LO peak from homoepitaxial GaAs, TO stands for transverse optical phonon peak; and (d) phi-scan of (220) plane for these three samples showing the twinning in GaAs film, dotted line show the peak position for 60° twins, Arrows show the peak positions of (10.4) planes of sapphire, the Inset shows the representative RHEED along [110] direction after LT GaAs growth in S1 and S2, some spots corresponding to rotational twins have been shown by arrows while spots corresponding to reflection twins have been shown by dashed circles. 76

Figure 49: (a) Cross-sectional HRTEM image of S1 near film/substrate interface, SF is the abbreviation for stacking fault; (b) RC of all three samples (c) HRTEM image showing the formation of a pit on the surface due to extended defect. 79

Figure 50: (a) PL spectra of samples having three different thicknesses of LT layer and (b) PL of GaAs buffer (S1), InGaAs QW on sapphire (S1-QW), and InGaAs QW on GaAs substrate (p-InGaAs-QW). S1 PL repeated to show the shift of QW peak from GaAs, dashed arrow shows the GaAs PL peak position from homoepitaxial GaAs and GaAs on sapphire samples. 80

Figure 51: Schematic diagram of the sample structure..... 82

Figure 52: Surface morphologies of the samples grown at (a) 650°C and (c) 700°C. Real time growth image after the growth at (b) 650°C and (d) 700°C. Red arrows show the spots on the streaks. 83

Figure 53. (a) only (111) crystal orientation is observed in out of plane measurements; (b) Sample S2 shows the lowest FWHM; (c) Phi scan shows the twinning on both samples; (d) PL measurements of both samples at 10 K.....	85
Figure 54: Room temperature PL from sample S2.	86
Figure 55: (a) schematic diagrams of the samples A1, A2 and A3; (b) TCA steps.....	87
Figure 56: AFM images of samples grown (a) without annealing; (b) two times annealing; (c) TCA.....	88
Figure 57: (a) Out of plane orientation confirmed only (111) single crystal orientation; (b) sample A1 shows the highest FWHM from the rocking curve measurements; (c) Twinning is observed from all samples; (d) RT PL emission from A1, A2 and A3 samples.	89
Figure 58: PL measurements of samples A1, A2 and A3 at (a) LT, (b) RT.....	90
Figure 59: Power dependent PL spectra for two lasers (a) 532 nm cw; (b) 700 nm fs.....	91
Figure 60: Integrated PL intensity vs incident power for two cw laser and pulsed laser.	92
Figure 61: Atomic arrangement of (a) r-plane sapphire, (b) GaAs (110) plane, and (c) GaAs (111) plane.....	94
Figure 62: AFM images of (a) c plane and (b) r plane sapphire substrates. Inset shows the substrate RHEED just before the growth.	95
Figure 63: AFM Surface morphology on 2 μm x 2 μm scan area of 10 nm GaAs growth on (a) c-plane (C-600) and (b) r-plane sapphire substrate (R-600); (c) Phi-scans of both samples, arrows (red for R-600 and black for C-600) showing GaAs (220) peaks, corresponding RHEED images after the growth are shown in the inset of figure.	98
Figure 64: XRD omega-2theta scan of C-600 and R-600. Sharp and intense peaks are related to sapphire substrates.	99
Figure 65: AFM and RHEED of (a) R-500 (b) R-600 (c) R-650.	100
Figure 66: (a) Omega-2theta scan of R-500, R-600 and R650; (b) phi-scan of R-600 and R-650.	102
Figure 67: AFM surface morphology of (a) RA-1 (b) RA-3.5 (c) RA-6.....	103
Figure 68: (a) Omega-2theta scan and (b) phi-scan of RA-1, twin peaks are denoted by rectangles, angles between different types of peaks are shown in the figure. Pole figure of the same sample is shown in the inset with sample tilt ranging from 0-70 $^{\circ}$	104

Figure 69: Arrangement of Al atoms in r plane sapphire (blue dots) and two possible in-plane orientations of GaAs separated by approximately 28° 105

List of Table

Table 1: Structural details and growth parameters of samples presented in this work.....	49
Table 2: GaAs island size, density, and percentage surface coverage with a deposition amount. 52	
Table 3: Thickness of III-As film on sapphire.....	74
Table 4: Linewidth and integrated intensity ratio of broader and sharper curves from Gaussian fitting of RC for samples S1, S2, and S3	79
Table 5: Integrated intensity, linewidth, and peak position of QW PL peak from both QW samples.	81
Table 6: Surface roughness, thickness, and FWHM of the samples A1, A2 and A3 are listed ...	88
Table 7: Step height, terrace width, and unintentional miscut angle of c and r plane substrates are listed.....	96
Table 8: Island height, density, and total volume on 2 μm x 2 μm AFM scan area.	98
Table 9: Growth temperature, GaAs island height and density for three GaAs/r-plane sapphire samples.....	101

Chapter 1: Introduction

1.1 Integrated Microwave photonics

Microwave (MW) frequency lies at the higher frequency end of the radio waveband, and its frequency ranges from 300 MHz to 300 GHz, which is used for wireless and satellite communications, radar, cellular, Wi-Fi, cable television, medical imaging, and cooking [1]–[3]. In microwave photonics (MWP) systems, laser, modulator, waveguide, and photodetector are used to modify, control, transmit, and distribute MW and millimeter-wave [2–7]. The photonic technology has broadband and minimum loss facilities, which can process the complicated signal and added value to the conventional RF systems. The MWP improves the RF communication system by increasing speed, bandwidth, dynamic range, and processing capability [8]–[10]. It opens a new window of research where extensive device integration would be possible by reducing device size. It also creates new opportunities for ICT and networks.

IMWP integrates optoelectronics and passive like Triplex technology in monolithic or hybrid photonic circuits, which reduces footprint, complexity and improves the light-matter interaction due to the small mode volume by the nonlinear optical process [4], [11], [12]. Figure 1 shows an IMWP system where a modulator converts an RF wave to an optical signal and a continuous wave laser is modulated according to the RF wave. The modulator is connected with an optical signal processor by a waveguide where the processing task is being executed. Then the processed signal is transferred to a photodetector and converted into an electrical signal. An RF receiver (is not shown in figure) extracts the information from the electrical signal.

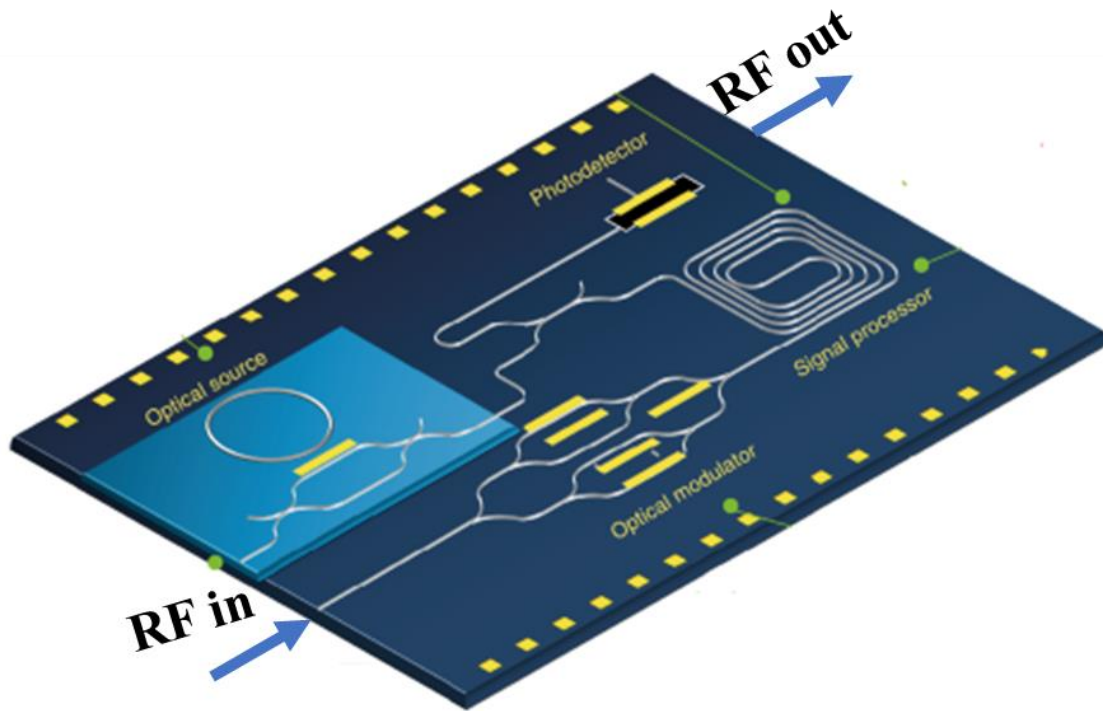


Figure 1: Integrated microwave photonics system [11] .

In the last ten years, mainly three key platforms have been focused for the monolithic integration of MWP circuits: Indium Phosphide (InP), silicon-on-insulator (SOI), and silicon nitride (Si_3N_4) (Figure 2). Every platform has its strengths and weaknesses. InP is a desirable and complex platform because it is the only platform where monolithic integration of active and passive components, including lasers, modulators, tunable devices, optical amplifiers, and photodetectors, is possible. However, the propagation loss in InP optical waveguides is relatively high of the order of 1.5-3 dB/cm [13], [14]. Si photonics compatibility with Complementary Metal Oxide Semiconductor (CMOS) fabrication process and the high refractive index contrast between Si and SiO_2 , which offer strong optical confinement give the real possibility of electronic-photonics co-integration. Si photonics have matured optical components such as optical modulators, waveguides, and photodetectors. The main hurdle for Si photonics is its poor light emission property [15], [16]. TriplexTM is a well-known technology for low loss passive components like

waveguide fabrication. The alternating well defined and highly stable silicon nitride Si_3N_4 and SiO_2 are used in TriplexTM technology [17]. The CMOS compatible Si_3N_4 and SiO_2 waveguide are gaining popularity because of ultra-low loss operation and low-cost volume production [17]–[19]. TriPlexTM technology provides low loss on silicon and glass substrates in the broad wavelength range between 405 nm up to 2.35 μm . For the integration optical sources, modulators, amplifiers, and detectors integration TriPlexTM platform relies on InP.

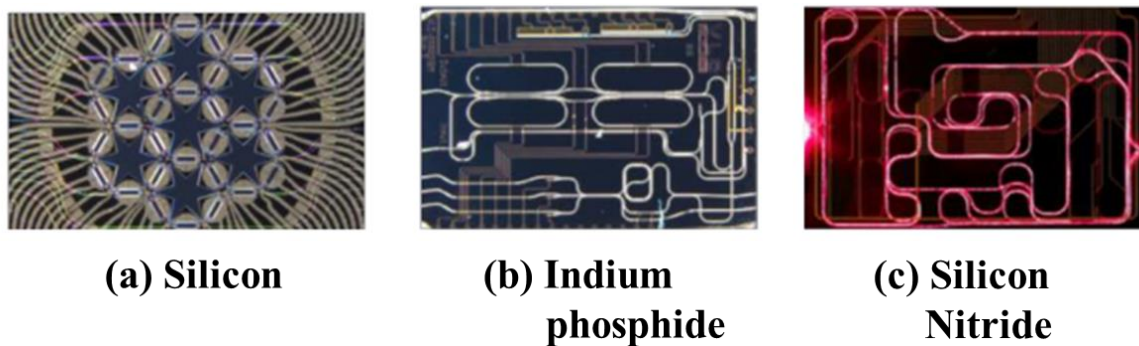


Figure 2: Three platforms for integrated microwave photonics (a) silicon-on-insulator (SOI) for programmable signal processor [20], (b) indium phosphide for all-integrated tunable filter [20], and (c) silicon nitride for high spectral resolution bandpass filter [21].

It is obvious that individual platforms are still not matured enough for the full integration of IMWP. Therefore, researchers have been looking for a suitable and alternate platform where a hybrid or monolithic integration is possible. Here, we propose highly resistive and optically transparent from UV to IR sapphire as a 3D integrated microwave photonics platform as shown in Figure 3, where laser source, modulator, waveguide, photodetector, and RF circuits can be monolithically fabricated by utilizing current technology.

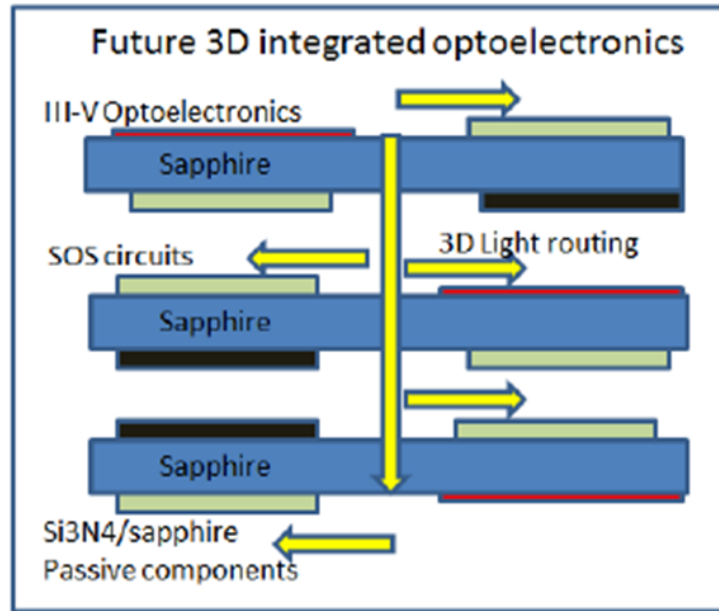


Figure 3: Sapphire based 3D integrated microwave photonics architecture.

1.2 Motivation

There are several reasons for the consideration of sapphire as a platform for integrated microwave photonics. The CMOS compatible Si on sapphire (SOS) is a matured technology. It can embrace all the features of Si photonics and RF high-frequency circuit technology featuring low power consumption. The TriPleX™ is a well-known technology for the low loss (0.1db/cm down to 0.1 db/m) passive components which covers a wide wavelength range and is widely used in MWP, visible light applications, and sensors [17]. The high refractive index contrast and the low material absorption is prerequisite for optical confinement and low loss passive components. In both cases, sapphire substrates can be a good competitor for the quartz substrates in TriPleX™ technology. The comparison of refractive index and absorption coefficient for Si₃N₄, SiO₂, and sapphire is shown in Figure 4. From the figure, the refractive index difference between sapphire and Si₃N₄ is

0.3, which is sufficient for building a tightly confined waveguide. For optical loss, sapphire is a transparent material, and its absorption coefficient is very low.

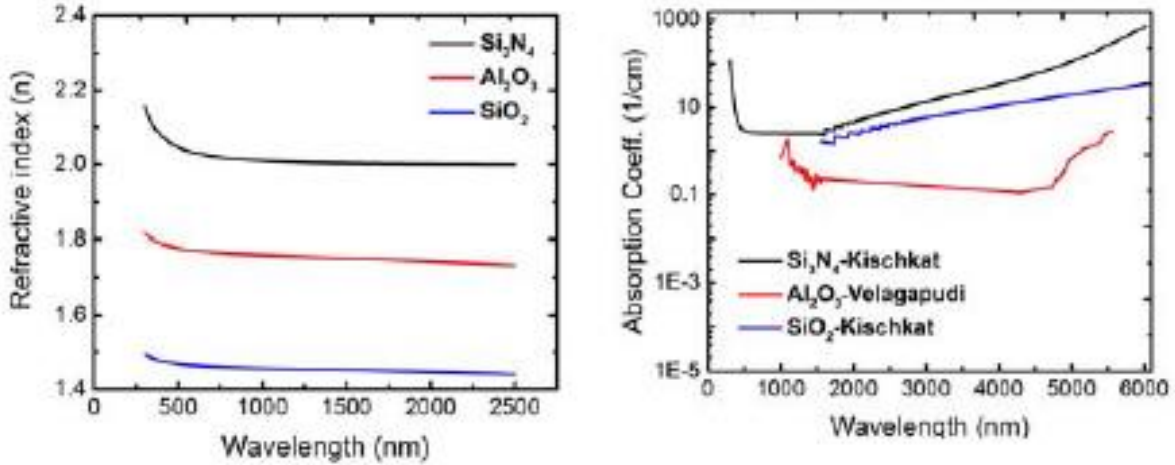


Figure 4: A comparison of refractive index and absorption coefficient for Si₃N₄, Al₂O₃, and SiO₂ [22].

For optoelectronics, the sapphire platform relies on III-V monolithic growth. The growth of III-V, especially GaAs and GaSb on sapphire, is a challenging task because of high lattice mismatch and different crystal structures (GaAs, GaSb-Zinc blende, and sapphire-hexagonal) [23], [24]. For the high-quality crystal growth, a similar thermal expansion coefficient of film and substrate is significant because it does not give any extra crack or defects during the cooling of the film [25]–[27]. The thermal expansion coefficient of GaAs ($5.73\text{E-}6\text{ K}^{-1}$) and GaSb ($7.75\text{E-}6\text{ K}^{-1}$) is closely matched to sapphire ($6.66\text{E-}6\text{ K}^{-1}$ parallel to the optical axis and $5\text{E-}6\text{ K}^{-1}$ perpendicular to optical axis). With a sophisticated crystal growth technique, it could be feasible to grow high lattice mismatch III-V thin film on foreign substrates. In my Ph.D. work, I have been working on the growth of GaAs on c and r plane sapphire substrates for the optoelectronic material of IMWP. In the following sections I will discuss the crystal structure of GaAs and sapphire, challenges of growth of GaAs on sapphire, advantages of the system, etc.

1.3. Background

1.3.1 GaAs

Goldschmidt first created GaAs in the 1920s, and it is a compound semiconductor consisting of Ga and As elements as shown in Figure 5 [28]. It has a cubic sphalerite (zinc blende) crystal structure, and the lattice constant is 5.656\AA . GaAs has a face-centered cubic (FCC) translational symmetry. The coordinate of one atom is $(0,0,0)$, and the other atom is $(1/4,1/4,1/4)$.

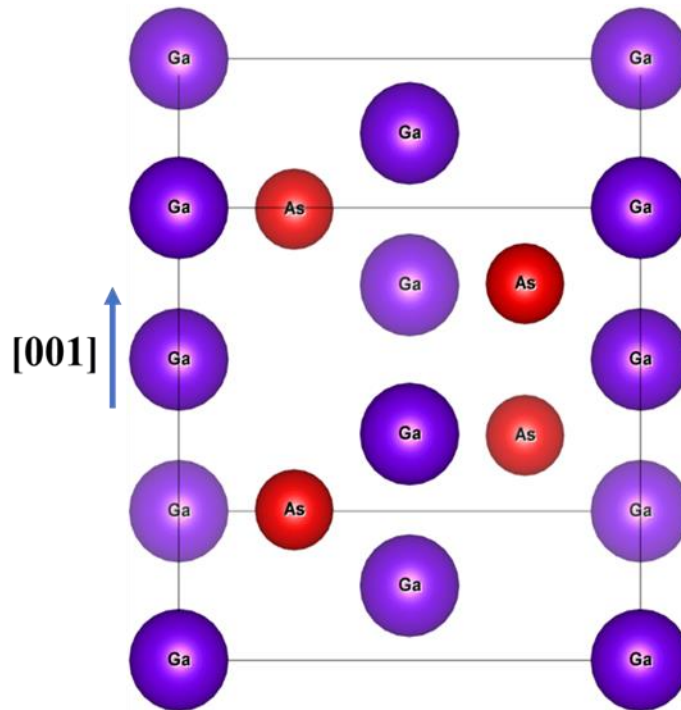


Figure 5: FCC unit cell of GaAs crystal structure.

Gallium arsenide's zinc blende structure can be considered superimposed of two FCC lattices, one of Ga and the other of As, offset by the basis vector. There are 14 gallium atoms and four arsenic atoms in the GaAs unit cell from the above figure.

However, each of the corner Ga atoms is shared by eight neighbors' cells and faces Ga atoms are shared by two cells. Therefore, there are total 4 gallium atoms and 4 arsenic atoms in the GaAs unit cell. The nearest neighbor distance in GaAs is $r_o=(\sqrt{3} a/4)$, where a is the lattice constant and Ga (As) makes four tetrahedral bond angle $\varphi=\cos^{-1}\left(-\frac{1}{3}\right)=109.47^\circ$ with four As (Ga). The most studied and important crystal planes of GaAs are (001), (111), and (110), as shown in Figure 6. From the figure, the atomic arrangements of each crystal plane are different.

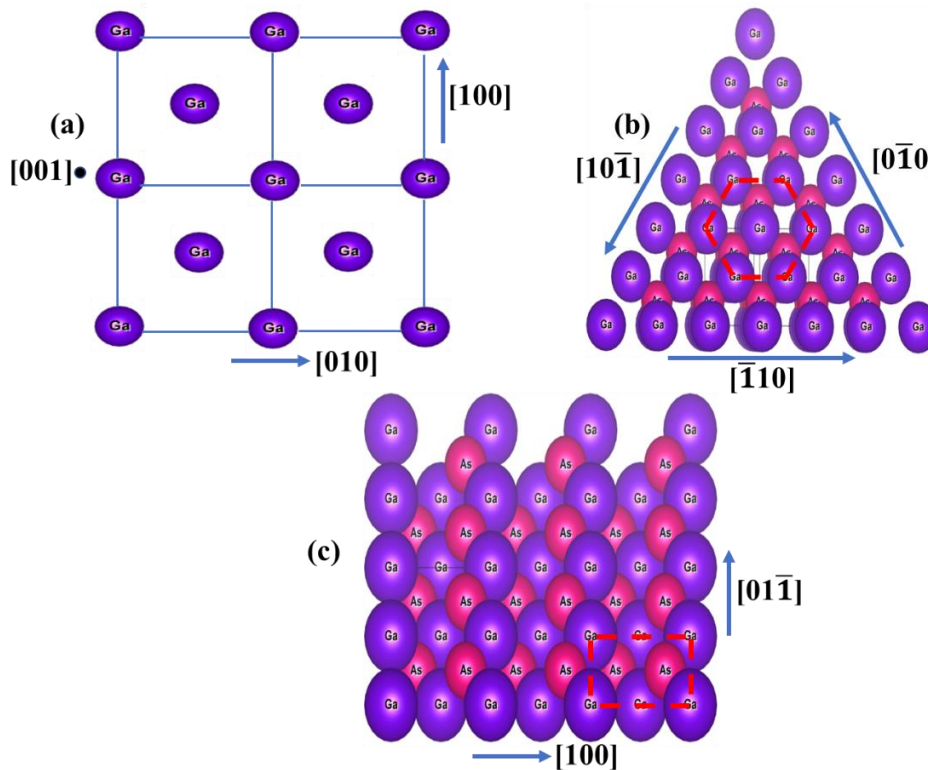


Figure 6: GaAs crystal planes (a) (001); (b) (111); (c) (110).

These atomic arrangements are directly related to the crystal planes' surface energy, which is an important factor for the 2D crystal growth. In (001) crystal plane, 4 Ga (As) atoms are at the corner of the crystal plane and an Ga (As) atom at the center (Figure 6 (a)). Figure 6 (b) shows the (111) GaAs plane. The unit cell of GaAs contains four (111)A and four (111)B crystal planes. The atomic

distance in the (111) crystal plane is 3.99 Å. The atomic arrangement in (110) crystal plane forms a rectangular crystal structure as shown in Figure 6 (c) [28]. The (110) crystal plane contains the same number of gallium and arsenic atoms and it is intrinsically neutral [29]. The atomic distance along the [010] and [110] directions are 5.656 Å and 3.999 Å respectively.

1.3.2 Optical properties

GaAs is a direct band gap material. Higher electron mobility and wider direct band gap make it an essential material for optoelectronic devices, light-emitting sources, photovoltaic devices, high power microwave, and millimeter-wave devices. The E-K diagram of GaAs direct band gap is shown in Figure 7. The valence band's maximum energy and the lowest energy of the conduction band are at the same value of momentum. The value of the GaAs bandgap at room temperature and under normal atmospheric pressure is 1.42 eV. The bandgap value is true for high purity GaAs, and band gap becomes smaller with doping materials. The bandgap is also a function of temperature and can be written as-

$$E_g(T) \approx E_g(0) - \frac{\alpha T^2}{T + \beta} \quad \text{Equation 1}$$

where $E_g(0)$, α , β are materials constants. At $T=0$ K, the bandgap energy of GaAs approaches 1.52 eV. The optical properties of GaAs can be changed by incorporating materials like In, Al. This allows bandgap tuning and introduces new electrical and optical properties to the materials. For example, ternary alloy $\text{Ga}_{1-x}\text{In}_x\text{As}$ band gap can be adjusted over an energy range to adjust the low attenuation region of many optical fibers [30].

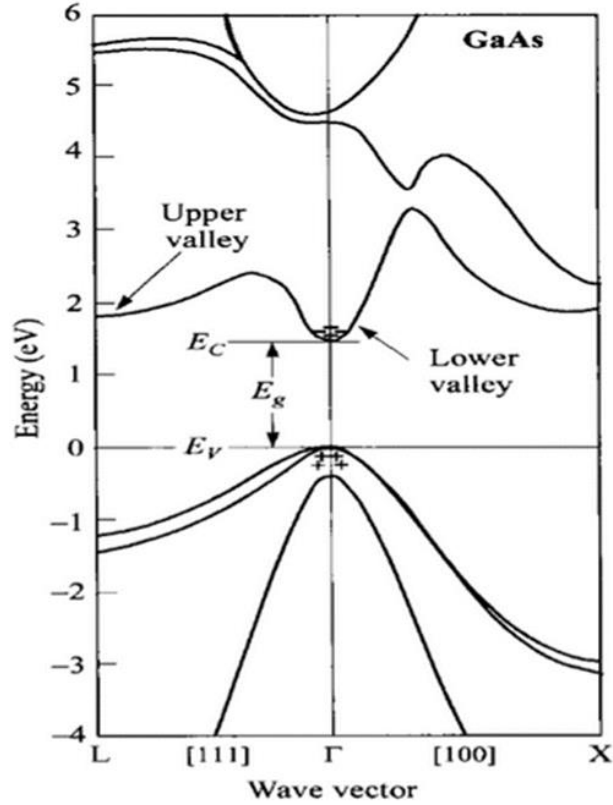


Figure 7: Energy band diagram of GaAs [31].

1.3.3 Sapphire

The sapphire crystal lattice is formed by Al^{3+} and O^{2-} ions. The coordination numbers of Al^{3+} and O^{2-} are 6 and 4, respectively. Single crystal sapphire belonging to the space group of $R\bar{3}C$ has a hexagonal/rhombohedral crystal structure. The hexagonal unit cell of sapphire is formed by alternating close-packed planes of oxygen with a hexagonal array of aluminum planes. Due to crystal lattice distortions, Al^{3+} cations are in a crystalline field that has no symmetry center. It lies in the octahedral hollows between the closely packed O^{2-} , filling two-thirds of these hollows as shown in Figure 8 (a), such that $2/3$ is the stoichiometric ratio of Al/O in sapphire. Along the $[0001]$ direction the aluminum atoms and vacancies have a threefold symmetry. Due to the high optical transmission, mechanical strength, insulating nature, sapphire is popular as a substrate in

the semiconductor industry for thin film growth and device fabrication, e.g., high-power-radio-frequency applications, high power, and high-frequency CMOS integrated circuits. The thermal expansion coefficient of a substrate is significant for the thin film growth. For sapphire along an axis, the thermal expansion coefficient is $6.2 \times 10^{-6} \text{ K}^{-1}$, while that along c-axis is $7.07 \times 10^{-6} \text{ K}^{-1}$. The unit cell of sapphire and different crystal planes is shown in Figure 8 (b). For the IMWP optical source, we have been growing GaAs on both c and r plane sapphire substrates. The atomic arrangements of both crystal planes are discussed below-

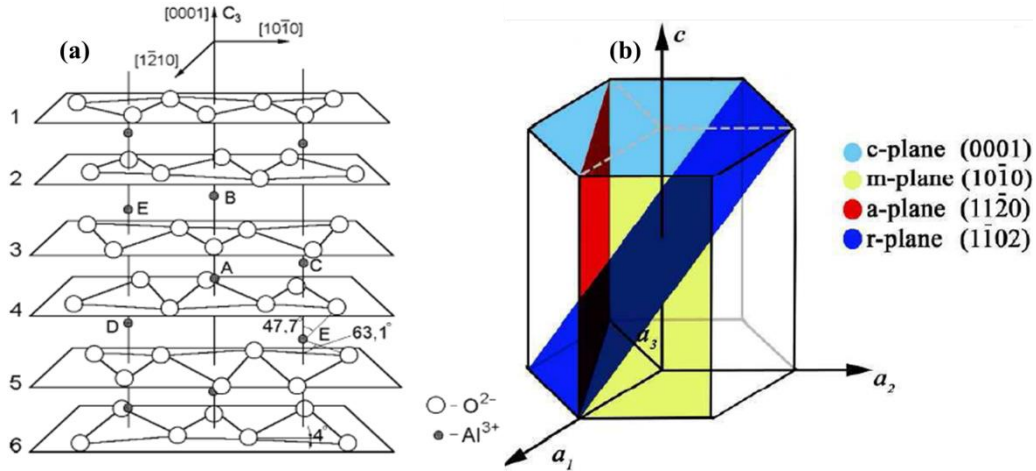


Figure 8: (a) Schematic of the arrangements of Al^{3+} and O^{2-} layers in sapphire [32]; (b) sapphire unit cell and different crystal planes [33].

The c plane is the sapphire substrate's basal plane, and the r plane is inclined 57.5667 degrees to the optic axis [33]. The c plane and r plane sapphire have hexagonal and rectangular crystal structures, respectively. Octahedral hollows are present for c-plane sapphire as shown in Figure 9, and the distance between the hollows is 4.756 Å. The c-plane sapphire has three-fold rotational symmetry about its normal. The oxygen sublattice is 30 degrees rotated with Al sublattice along with the [0001] direction. The distance between Al-Al sublattice is 2.747 Å.

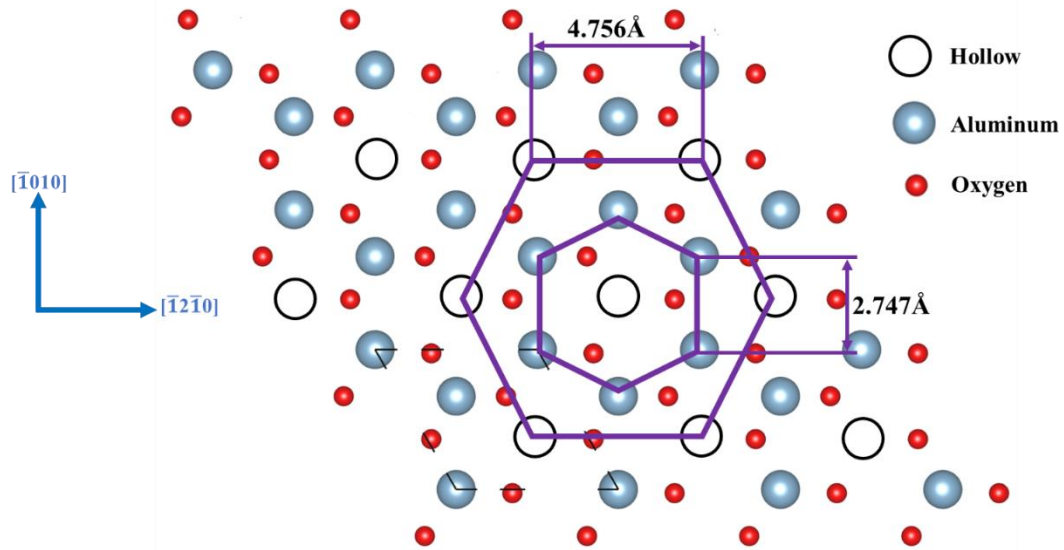


Figure 9: Basal or C- plane sapphire substrate.

In r plane sapphire, Al-Al sublattice distances in $[\bar{1}101]$ and $[11\bar{2}0]$ direction is 5.1272 Å and 4.756 Å, respectively (Figure 10) and the r-plane sapphire has one-fold rotational symmetry about its normal [34]–[37].

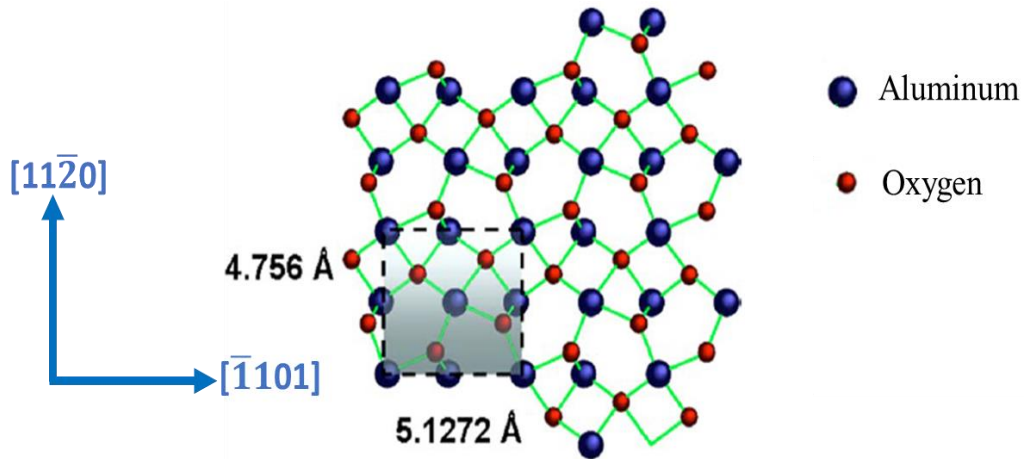


Figure 10: R-plane sapphire substrate [38].

1.4 GaAs growth on sapphire

The functionalities and potential of GaAs film on the sapphire substrate for microwave photonics (MWP), optoelectronics, and electronics motivated us to work on GaAs/sapphire system. As a substrate, the sapphire has an immediate advantage like silicon on sapphire (SOS) is a matured technology or electronic components and an existing body of work on Si_3N_4 on sapphire for passive components and waveguides. The thermal expansion coefficient is an important factor for the growth of crack-free epitaxial film, which is nearly equal to the III-V semiconductor and sapphire. Therefore, III-V growth on a semiconductor can create the possibility of monolithic integration of III-V semiconductor light sources, modulators, detectors, low loss waveguides, passive devices, CMOS, and RF silicon circuits. Besides, the sapphire substrate's high insulating property, high refractive index contrast between GaAs and sapphire system, and optical transmission of the sapphire substrate near III-As band gap provides the potential for 3D photonic systems. The integration of microwave photonic (MWP) functionality and electronics on a single chip can dramatically increase speed, bandwidth, processing capability, and dynamic range [23], [24], [39].

We have been growing GaAs on both c- and r -plane sapphire substrates for the monolithic integration of optical and electronic devices. The growth of single-crystalline GaAs 2D film on sapphire (c and r plane) substrates is challenging because of (i) high lattice mismatch; (ii) dissimilar crystal structure. The large lattice mismatch produces rough surfaces and defects in the epitaxial materials. Since the crystal structure of GaAs and sapphire substrates are different, so the growth film can be [111] oriented on c-plane sapphire substrate because it is a least similar in crystal structure. On the other hand, the rectangular (110) plane of GaAs may align with the

rectangular r-plane of sapphire, while the hexagonal nature of the sapphire might force the epitaxial growth of GaAs to be of (111) orientation, or GaAs might take a totally different orientation.

We must also consider the third feature: the chemical bonding at the interface between two materials. For example, high interfacial energy can lead to poor interaction between the two material surfaces. In this case, with a high lattice mismatch, different crystal structure, and unfavorable interface energy, one may expect poor crystal quality for GaAs on sapphire. On the other hand, GaAs may not even wet the sapphire substrate for a thin GaAs layer, and growth may occur by ignoring the high lattice mismatch and different crystal structures. In this thesis, we discuss the direct growth of GaAs on sapphire (c and r plane); direct growth of GaAs on sapphire (c and r plane) but after an initial thin AlAs nucleation layer; the effect of the pre-growth c plane sapphire substrate surface treatment on GaAs growth, the role of the growth temperature and post growth annealing on GaAs growth on sapphire. Next, the importance of two-step growth to reduce misfit and threading dislocations. The nucleation layer, annealing, and two-step growth provides a highly relaxed, smooth, active surface that produces high-quality photoluminescence at low temperature and room temperature.

Chapter 2: Crystal growth and Growth techniques

Crystals are periodic arrangements of atoms, molecules, or ions in all three dimensions [40]. Crystalline materials have a huge impact in research, industry, optoelectronic devices, and biosensors. Their demands are increasing day by day. The epitaxy is an excellent way for the growth of high-quality crystal materials. In this chapter, different epitaxial systems, growth modes, and growth techniques are discussed.

2.1 Epitaxy

The growth of crystal film with a specific orientation on the top of a crystalline substrate is known as epitaxy. The film is called an epitaxial film or epitaxial layer [41], [42]. The epitaxial growth can result in a 1D, 2D and 3D crystal growth. There are different techniques for the growth of crystal by epitaxial method like- (i) molecular beam epitaxy (MBE); (ii) chemical vapor deposition; (iii) liquid phase epitaxy; (iv) vapor-phase epitaxy. Based on the substrate and layer material, there are two types of epitaxial systems- (i) homoepitaxial system; (ii) heteroepitaxial system [43].

2.1.1 Homo and heteroepitaxial systems

In the homoepitaxial growth, the film and the substrate are of the same material, so there is no lattice mismatch. In the heteroepitaxial system, the grown film and the substrate are of different materials, having different lattice constants but usually having the same crystal structures. Therefore, the strained or fully relaxed epitaxial film can be grown on the substrate depending on the interfacial conditions, lattice parameters, and thickness of the film shown in Figure 11. The heteroepitaxial system is the most interesting to explore their extraordinarily rich interaction,

unknown bonding at their interfaces, and unexpected novel properties. For example, one can imagine semiconductors' growth on semiconductor, semiconductor on insulator, or semiconductor on ferroelectric. The key point is that the degree of coupling at the interface can create systems with remarkable properties, such as geometry-dependent excited-state lifetimes and magnitude of fluorescence, tailored index of refraction and dispersion, non-reflective materials, and control over carrier mobility and coherence. To succeed at the growth of dissimilar materials, conventional wisdom has generally required that the two materials have the same or similar crystal structures, for example, AlAs on GaAs, which is zinc-blende on a zinc-blende substrate. Another common example is GaN on sapphire, which is wurtzite (hexagonal) on a trigonal (hexagonal) substrate.

In fact, one might say that today's semiconductor industry is guided by a "**golden rule**" for new material development: "Starting growth on substrates with similar structures". There is even a "corollary" to this rule which is to "closely lattice-match the two semiconductors for the purpose of high material quality". For example, this is the case for AlAs on GaAs while being not true for InAs on GaAs resulting in very poor growth quality for thick films. Here we propose to **break away** from the rules and take an entirely different approach to the growth of dissimilar materials, such as, combining dissimilar cubic GaAs and hexagonal sapphire. This third kind of epitaxial system is called **dissimilar epitaxy**.

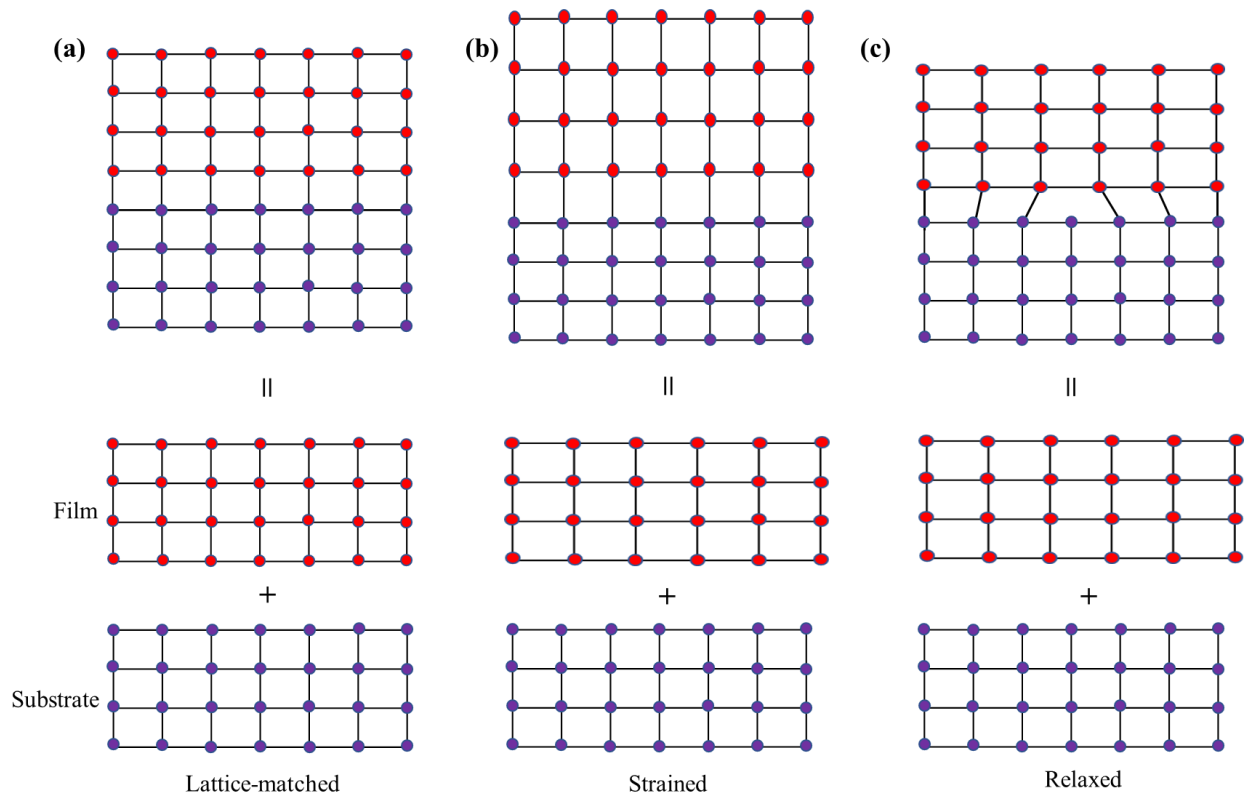


Figure 11: Schematic representation of (a) lattice- matched, (b) strained, and (c) relaxed (misfit dislocation) epitaxial growth.

2.2 Thin film growth modes

For the thin film growth, the atoms are transported to the substrate, and the adatoms (deposited atoms) diffuse on the surface to find nucleation sites like edge, kink, or clusters to minimize energy [44]. The affinity of adatoms to the substrate or each other determine the film morphology on the substrate [45]–[48]. There are three types of growth modes, these are (i) layer-by-layer growth or Frank-van der Merwe (F-M), (b) island growth or Volmer-Weber (V-W), and (c) mixed growth or Stranski-Krastanov (S-K) as shown in Figure 12. In the F-M mode, adatoms are strongly attached to the substrate, which promotes the wetting of the substrate surface and two-dimensional film growth. It usually occurs in the semiconductor and oxide materials growth. When the interaction within adatoms is stronger, 3D islands are formed on the substrate, the growth mode is known as

V-W. The size of islands increases by different coalescence phenomena like Ostwald ripening, sintering and cluster ripening until a film of different grains is obtained. The V-W growth mode typically occurs during the growth of metal and semiconductor (i.e., group IV, III-V, etc.) on oxide or rock salt substrate.

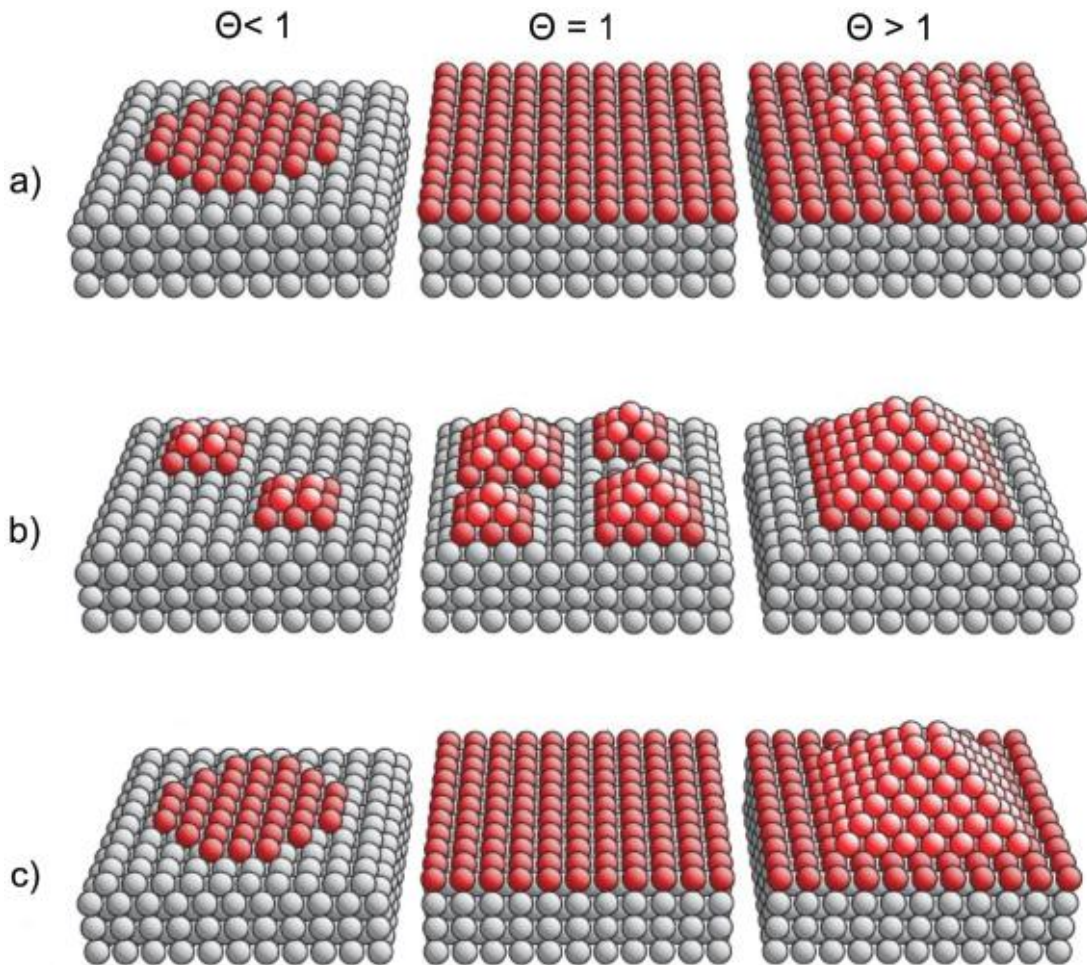


Figure 12: Schematic illustration of three growth modes. (a) Frank-Van der Merwe, (b) Volmer-Weber, and (c) Stranski-Krastanov. Substrate (overlayer) atoms are shown in grey (red) where the lighter red is on the first adsorbate layer. Θ represent the amount of deposited material ($\Theta=1$ represent one monolayer deposited atom on substrate atom) [44].

The S-K growth mode is a mixture of F-W and V-M growth mode. In this mode, film grows layer by layer until it reaches a critical thickness and 3D islands start to grow. Islands grow on a wetting

layer rather than directly on the substrate as in V-W growth mode. The heteroepitaxial systems with small lattice mismatch mainly follow the S-K growth mode [44], [49]–[52]. The following Young's equation are systematically classified the three different modes of growth in terms of their surface energy-

$$\gamma_s = \gamma_{fs} + \gamma_f \cos \theta \quad \text{Equation 1}$$

where, γ_s = substrate surface energy, γ_{fs} = interface energy between film and substrate, γ_f = film surface energy, θ depends on the surface properties of the substrate and impinging atoms/molecules [48]. F-W growth mode occurs when impinged atoms wet the substrate surface, and the contact angle θ becomes zero (Figure 13). Then the equation 2 becomes-

$$\gamma_s = \gamma_{fs} + \gamma_f \quad \text{Equation 2}$$

V-W growth mode occurs when the sum of the film's surface energy and interface energy is higher than the substrate's surface energy. The 3D growth mode happens when the contact angle between islands, and the substrate is greater than zero and the young's equation becomes-

$$\gamma_s < \gamma_{fs} + \gamma_f \quad \text{Equation 3}$$

S-K growth mode occurs when a strained film generates on the substrate and the interface energy increases with film thickness. The following inequality is fulfilled for the S-K growth mode-

$$\gamma_s > \gamma_{fs} + \gamma_f \quad \text{Equation 4}$$

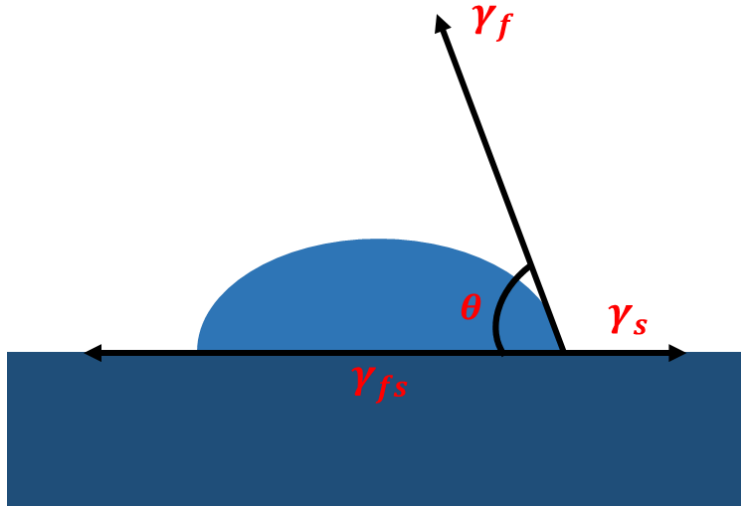


Figure 13: Surface energies and angle between islands and substrate.

In this work, we have used the molecular beam epitaxy (MBE) system for epitaxial growth. In the following section, we will discuss the MBE growth system, and in-situ reflection high energy electron diffraction (RHEED) characterization tool.

2.3 Molecular Beam Epitaxy

Molecular beam epitaxy (MBE) is an advanced technology for high-quality epitaxial material growth. In MBE, the basic concept of crystal growth can be described as follows. The energetic atoms are directed towards a growth surface or substrate. The heated substrate provides sufficient energy for the adatoms' diffusion to find a favorable lower energy site and become incorporated into the crystal lattice. The ultra-high vacuum (UHV) (10^{-10} - 10^{-11} torr) inside the chamber reduces the scattering of incident atoms before reaching the growth surface and the possibility of the incorporation of unwanted impurities. The capability of precise control over growth parameters like growth temperature, growth rate, film thickness, and atomic impingement flux make MBE an ideal system for electronics, optoelectronics, and photovoltaic device materials growth [53]. In-

situ RHEED allows the real-time crystal growth study, atomically flat substrates surface preparation with specific surface reconstruction [43], [48]. Using MBE, we can grow two-dimensional material with an atomically flat surface from the low lattice-matched (<2-3%), and three-dimensional islands with entirely confined structure from the high lattice mis-matched systems.

A Riber MBE 32 is dedicated to arsenide like GaAs, InAs, InGaAs, etc., materials growth at the University of Arkansas. It is connected with the other two chambers by a transfer line (Figure 14). For the other two chambers, one is used to grow oxide materials, and another is for group IV materials. The arsenide chamber's connection to other chambers opens the possibilities for integrating materials of having different properties such as semiconductors on ferroelectrics material.

The ultra-high vacuum in the MBE was achieved by several pumps such as rough pump, turbo pump, and ion pump. Cryopanel is surrounded inside the growth chamber. During growth, liquid nitrogen (LN₂) was supplied through cryopanel, which also acts as a pump by trapping atoms. Cryopanel also provide the temperature isolation between cells. Generally, the effusion cell or Knudsen cell (K-cell) is used for source materials reservoir and heated by electron bombardment or resistance heaters. For Knudsen cell's crucible, they are made of different materials, such as tungsten, stainless steel, nickel, graphite, pyrolytic boron nitride (PBN), quartz, etc., depending on the investigation.

Thermocouples are connected with the cell crucible for the temperature measurements. The cell temperature controls the amount of flux to be emitted. For the As₂ source, the flux is controlled by a combination of the source temperature and the cracker valve position. The temperature controller

and automated shutters were used for growth control. Each effusion cell has a dedicated shutter, for example, during GaAs growth gallium, and arsenic cells shutters were opened. The indium shutter was opened in addition to arsenic and gallium shutters during $\text{In}_x\text{Ga}_{1-x}\text{As}$ growth [54].



Figure 14: Three MBE chambers are connected by transfer line [55].

The in-situ characterization facility of the sample during growth makes MBE a unique growth technique. Our MBE system is equipped with a RHEED, an ion gauge for beam flux monitor, a growth gauge for chamber pressure measurement, a quadrupole gas analyzer (RGA) for the residual gas analysis and leak detection, and optical bandgap thermometry for substrate temperature measurement. All the instruments were valuable for the growth of GaAs on sapphire substrates [56].

2.3.1 Reflection high energy electron diffraction (RHEED)

Since the early days of MBE, RHEED has been a well-established and useful in-situ technique for structural analysis [57]–[59]. It can be used to determine the real time growth information such as

three growth modes, crystal stoichiometry and quality, chemical composition, growth rates, surface reconstruction, V/III flux ratio, and growth temperatures [60]–[62]. A finely collimated high-energy electron beam with energy 10-100 keV is used in RHEED for the surface analysis. The electron beam glances on the growth surface at a low angle ($<3^\circ$), and after reflecting, it strikes a phosphor screen where it makes a diffraction pattern. For a specific diffraction condition, the glancing angle is critical. It should be finely adjusted by inclining the sample to the electron beam or deflection coils one and two. The electron beam penetrates only one or two monolayers of the sample surface making the RHEED be a highly surface sensitive technique [63]. For the real-time growth study of GaAs, the RHEED was operated at a voltage of 20 keV and current 1.5 A. A charged coupled device (CCD) camera interfaced with a computer was used to record the diffraction pattern on the phosphor screen [61]. The KSA 400 software was used to analyze the surface reconstruction, growth rate, and the intensity oscillation of the spots during growth [56].

The Ewald sphere is usually used intuitively to understand the diffraction phenomena from the kinematically scattered electrons. The reciprocal lattice of the sample can be calculated directly from Ewald's sphere geometry. The center of the Ewald's sphere is at the sample surface, and the radius of the sphere is equal to the magnitude of the incident wavevector-

$$K = \frac{2\pi}{\lambda} \quad \text{Equation 5}$$

where, λ is the electrons' de Broglie wavelength.

For the elastic scattering, scattering wave vector has the same magnitude of the incident wave vector,

$$|K| = |K'| \quad \text{Equation 6}$$

Here, K' is the scattering wave vector.

The diffraction condition for the constructive interference,

$$K - K' = G \quad \text{Equation 7}$$

Here, G is the reciprocal lattice vector.

For a two-dimensional crystal lattice, the reciprocal lattice consists of equidistant planes perpendicular to the atom row. The Ewald sphere intersects the lattice planes and generates streaky pattern on the RHEED screen as shown in Figure 15.

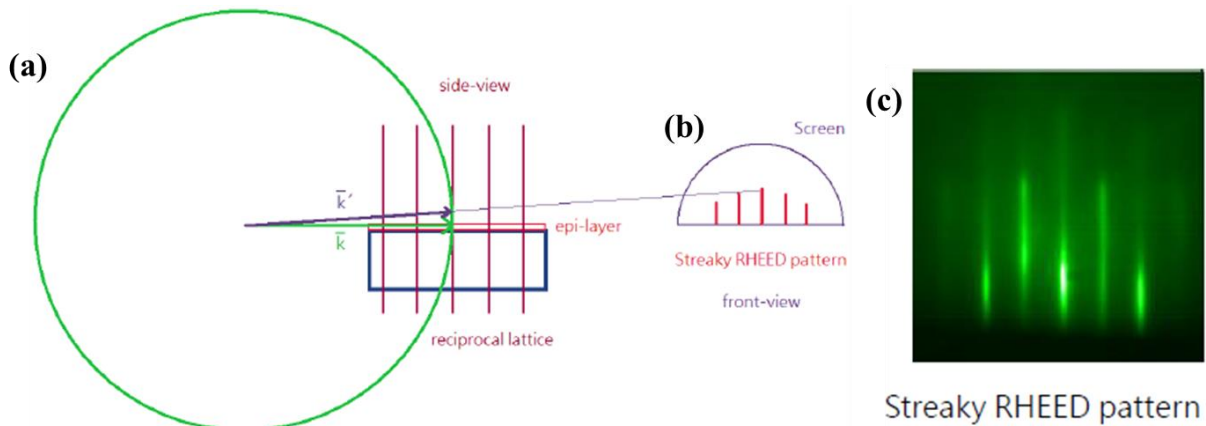


Figure 15: (a) An illustration of the reciprocal lattice rods of the 2D sample surface, perpendicular to atom rows. The intersection of the reciprocal lattice planes with Ewald's sphere, (b) streaky RHEED image from the 2D surface. (c) a static streaky RHEED image [64].

2.3.2 Substrate temperature measurement

During the growth of self-assembled quantum dots, low-temperature material growth, high-quality crystal growth, and the prevention of dopant segregation, accurate substrate temperature measurements are crucial in MBE [65], [66]. There are different ways on how to measure the substrate temperatures, such as a thermocouple, pyrometer, RHEED, and band edge thermometry. The thermocouples are reliable for giving a repetitive growth temperature, although the substrate thermocouple is mounted between the heater and the sample holder. As a result, the substrate thermocouple's temperature measurements always differ from the actual growth surface temperature. On the other hand, a pyrometer is mostly used for the temperature measurement of a distant object. It measures the temperature from the radiation emission of an object. The temperature measurements by pyrometer are influenced by viewport coating and stray light within the system [66]. Pyrometers are not efficient at low-temperature measurements, and it also depends on the emissivity of the materials which is difficult to find out. The substrate temperature can also be measured from the RHEED. The surface reconstruction of the substrate gives an idea about the surface temperature. Sometimes it is challenging to distinguish surface reconstructions and temperature measurements [66]. The bandgap is a fundamental property of a semiconductor, and it varies inversely to the substrate temperature (T_s) [67]. Band edge thermometry (BET) uses the bandgap for the substrate temperature measurement. The band edge thermometry can be employed by two ways, such as (i) reflection mode; and (ii) transmission mode [67]. BET is efficient for small substrates temperature measurements. The viewports coating, radiation from cells do not affect BET temperature measurements. However, BET measurement can generate local heat on the substrates, and make inefficient for doped and /or back side coated substrates.

Sapphire is an optically transmitted substrate from ultraviolet to infrared. The substrates' backside is coated with one-micrometer titanium to prevent the transmission of electromagnetic waves through the substrate from the heater. Therefore, during GaAs' growth, the transmission mode of BET of our MBE system could not be put to use. Also, GaAs growth on c plane sapphire is Ga terminated (111) oriented crystal. The (2×2) surface reconstruction of GaAs (111) A is invariant with growth temperature. Hence, we cannot get the ideal substrate temperature from the RHEED surface reconstruction image. So, we rely on the thermocouple temperature for the substrate surface temperature, and the actual growth temperature can be 80-100°C less than the thermocouple temperature.

Chapter 3: Characterization Method

After GaAs growth on sapphire, the substrate temperature was reduced to room temperature, and the substrate was taken out from the chamber for structural and optical characterizations. The surface morphology was investigated for the surface roughness (film), thickness (3D islands), and density (3D island). The strain, defects, thickness, and lattice constant were studied from the structural analysis. Different structural characterization tools like TEM, XRD, Raman spectroscopy were employed for this purpose. The optical measurement is a great way to study the light emission from the material and to confirm the crystal quality and defects. Both room and low-temperature photoluminescence (PL) measurements were performed for the GaAs crystal quality determination. In this chapter, discussions are focused on the basic principle, working method, and measurement conditions of the techniques that are used for the grown GaAs crystal's structural and optical quality determination. The first section is focused on the techniques for the structural material measurements while optical measurements techniques are discussed in the second section.

3.1 Structural material measurement

3.1.1 Atomic force microscopy (AFM)

Atomic force microscopy (AFM) or scanning force microscopy (SFM) is a powerful surface analysis technique at the nanoscale [68]. It provides qualitative, quantitative, and statistical information on many physical properties, such as surface morphology, texture, size, surface area, roughness, and volume distributions [69]. Typically, a probe, a laser, and a feedback system for collecting data are the main parts of an AFM as shown in Figure 16 [55]. A cantilever with a sharp tip of 10-20 nm diameter is used in AFM to scan the surface. The tip and cantilever are made of silicon and silicon nitride materials [70]. The basic principle of AFM operation is explained and illustrated below. During scanning, the tip as well as the cantilever are deflected by the sample's surface. The cantilever's deflection is measured by a reflected laser light from the back side of the cantilever. The topography or other properties of interest of the material are generated by feeding the deflection information to a computer [70]. There are three measurement modes of AFM: (i) Contact, (ii) Non-contact, (iii) and Tapping mode. In contact mode, the tip touches the surface while scanning, and the cantilever deflection determines the surface morphology [71]. The contact mode can destroy the soft material during the measurements. In noncontact mode, the cantilever oscillates at or close to its resonant frequency just above the surface as it scans [72], [73]. The attractive van der Waals forces, dipole-dipole, or any other long-distance forces between tip and sample are detected, and surface topography is determined from the attractive forces. The tip does not touch the sample surface, and the sample remains fine after measurements.

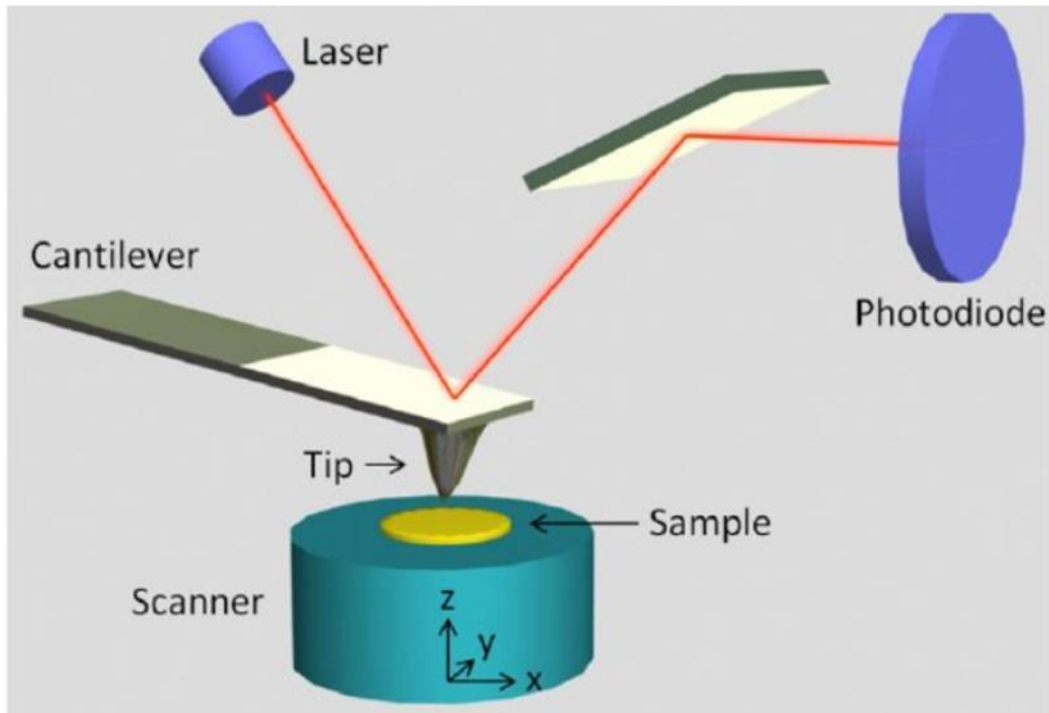


Figure 16: Schematic illustration of laser, tip, and photodiode in AFM system [74].

A liquid layer on the sample surface reduces the accuracy of the noncontact mode measurements. Tapping mode is also known as a dynamic, oscillating, or non-contact mode [75]. The cantilever oscillates at or the near-resonant frequency with a high amplitude (20 nm to 100 nm) and closer to the sample surface than noncontact mode. During oscillation, the tip touches the sample surface at the bottom of its swing. A constant oscillation amplitude is maintained by the PID feedback loop to support a constant interaction between the tip and sample [48]. The intermittent interaction between the tip and the measured surface produces the final image. In this research, the surface morphology of substrates, and the grown epitaxial material was investigated by tapping mode of a Bruker, model number 300-dimension III AFM. Stable and sharp tips made of Si with a tip radius of 10 nm, drive frequency of 300 kHz, and a spring constant of 40 N/m was used [23].

3.1.2 X-ray diffraction (XRD)

X-ray is an electromagnetic wave with wavelength, frequency, and energy ranging from 10 picometers to 10 nanometers, 30 petahertz to 30 exahertz (30×10^{15} Hz to 30×10^{18} Hz), and 124 eV to 124 keV, respectively. X-ray wavelength lies between UV rays and gamma rays. It was discovered by Wilhelm Conard Röntgen in 1895. X-rays are produced by maintaining a high voltage (20 KV) between an anode and cathode. The tungsten filament and high atomic weight metal are used for a cathode (source of electrons) and anode (target), respectively. High energy electrons are emitted from the cathode, strike the target, and the electron kinetic energy is transferred to produce x-rays. The emission of x-ray radiation by this mechanism is known as collision radiation. The high-energy electrons are decelerated by the atoms of the sample, and the kinetic energy of electrons converted into x-rays. This mechanism is known as Bremsstrahlung.

X-ray shows diffraction which is used for characterizing crystal materials [76], [77]. The crystal orientations, phases, distance between planes, grain size, thickness, strain, roughness, and defects related information can be extracted from the diffracted x-ray beam. The scattered x-rays at specific angles from each set of crystal planes generate constructive interference according to Bragg's law.

$$2d \sin \theta = n\lambda; n = 1, 2, 3 \dots \dots \dots \text{Equation 8}$$

where, d is the interplanar spacing, λ is the incident x-ray wavelength. The interplanar spacing d of the crystal planes can be calculated from the Bragg's law [56].

A PANalytical X'Pert MRD diffractometer (PANalytical, Almelo, Netherlands) was used for this work. The diffractometer equipped with a $\text{CuK}_{\alpha 1}$ x-ray source ($\lambda=0.15406$ nm), a four-bounce Ge

(220) monochromator for a collimated x-ray beam, a multilayer focusing mirror, and a Pixel detector to detect the diffraction. The PANalytical X'Pert MRD diffractometer in the Institute for Nanoscience Engineering at University of Arkansas is shown in Figure 17.

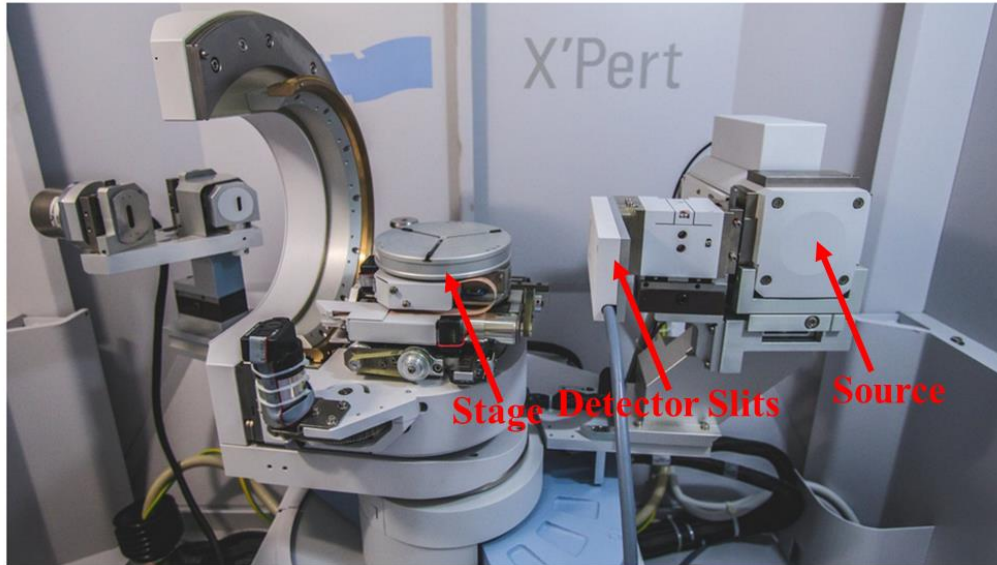


Figure 17: PANalytical X'Pert MRD diffractometer situated at University of Arkansas.

For the research as discussed in this thesis, the crystal orientation of grown film was confirmed by out of plane measurements or ω - 2Θ scan, the crystal quality was confirmed from the full-width half maximum (FWHM) of the rocking curve measurements or ω scan, in-plane registry between film and substrate was confirmed from the phi scan and pole figure measurements. During out of plane measurements, the sample was fixed, x ray tube or source moved by the angle Θ , and the detector moves simultaneously by the angle 2Θ . This gave the diffraction from crystal planes parallel to the sample surface and information about the preferential growth axes. The spreading of a parallel crystal plane from its ideal position was determined from the ω scan. In ω scan, the source and detector were fixed at a Bragg's angle of a crystal plane needed to be measured, and the sample was rocked with respect to growth axis. For the ϕ measurement, the source and detector

were fixed at a Bragg's angle of a crystal plane needed to be measured, the sample was tilted at χ angle and rotated around the growth direction [78]. The measurements conditions for the ω - 2θ scan, ω scan and φ scan are shown in Figure 18.

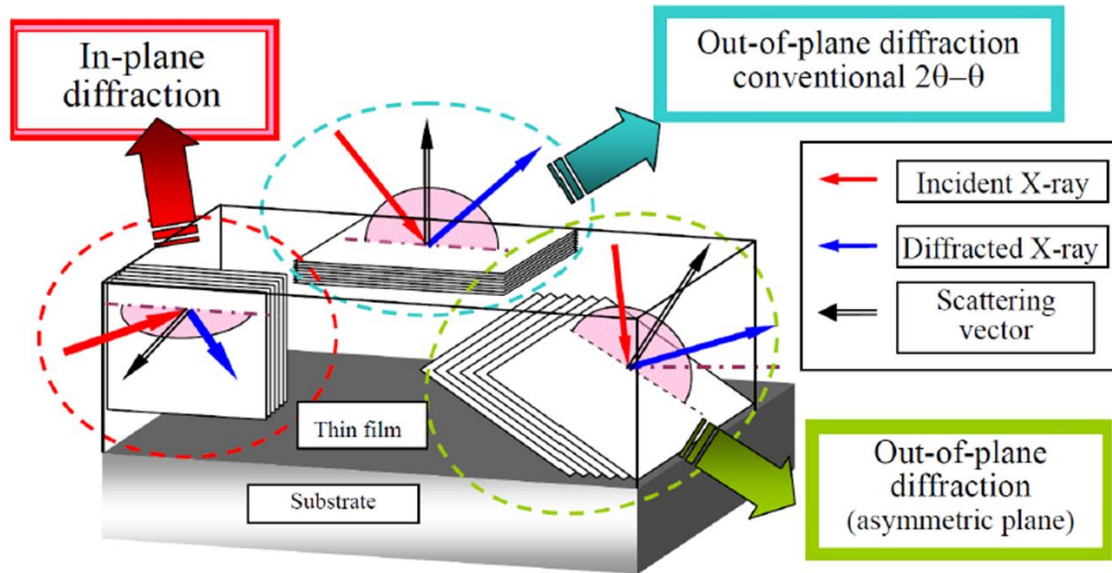


Figure 18: A schematic diagram of the geometries of thin film X-ray diffraction measurement, showing relations between the lattice planes of a thin film sample and x-ray geometrics [79].

3.1.3 Transmission electron microscopy (TEM)

TEM is considered the most popular nondestructive electron microscopy technique [80]. The high energy electron beam is used in TEM to analyze the structure, size, and morphology of a wide range of nanomaterials [81]. The basic structure of TEM consists of an electron emission source, electromagnetic lenses, and a detector. An electron beam is transmitted through a thin sample of thickness less than 100 nm. The interaction of electrons and the sample produce an image. Then the image is magnified and focused onto a fluorescent screen or a layer of photographic film. The TEM image can be used to determine crystal defects, such as misfit and threading dislocation,

small precipitates, dislocation loop, stacking fault, twinning, etc. It is also possible to detect the density of defects and small clusters with diameters $\sim 1-2$ nm [82].

The function principle for TEM and optical microscopy are similar; however, the source and lenses are different. In optical microscopy, photons are used as sources, glass lenses are used to control and focus on the optical beam, and images are viewed by eyepiece. On the other hand, in TEM, electrons are used as source, electromagnetic lenses are used to control and focus of the electron beam, and images are viewed on the screen [81].

There are two modes in TEM for crystal lattice mapping images-(i) high-resolution transmission electron microscope (HR-TEM); (ii) high angle annular dark-field scanning transmission electron microscope (HAADF-STEM). In HR-TEM, the transmission and diffraction occur of the electron beam. The interference between the transmitted and diffracted beam produces the crystal lattice mapping images rather than the actual atomic columns, while the direct crystal lattice mapping images are produced by HAADF-STEM [83]. The schematic diagram of these modes is shown Figure 19. The TEM advantages are powerful magnification, high quality image, and high spatial resolution for nanoscale materials [84]. TEM's disadvantages are regarded high to buying cost, necessity of UHV to avoid the scattering of the electron beam by gas molecules in the air, and the expertise is needed to run it [85].

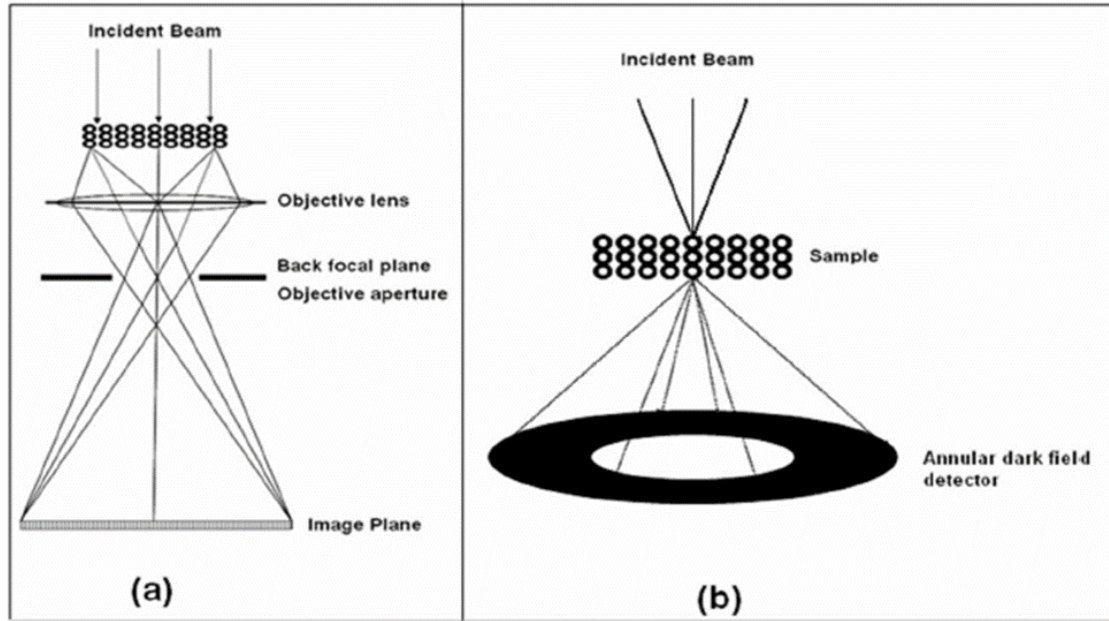


Figure 19: Schematic diagram of (a) HR-TEM imaging mode, (b) HAADF-STEM imaging mode [83].

The sample preparation is the most essential part of a high-quality TEM image. For this TEM image, the sample was cut into two small rectangular pieces and glued face to face, as shown in Figure 20. After gluing, it was transferred to a hot plate and annealed at 180°C. A clamping vise was used to compress the sample for the well gluiness [86]. The sample was then polished until thickness $<20\ \mu\text{m}$ was achieved by using an Allied High Tech Products Inc. polisher. The sample was then placed in a copper grid and then in a Fischione 1010 low-angle ion milling machine for making a hole in the middle of the sample. For our TEM, 50-300 nm thickness of the optically transparent area around the hold is sufficient for high-quality imaging. A Cs corrected Titan 80-300, with a Schottky field emission gun (FEG) that was operated at 300 kV, was used to take cross-sectional high-resolution TEM (HRTEM) images. In addition, A TF20 TEM, with electron source operated at 200 keV was also used [86].

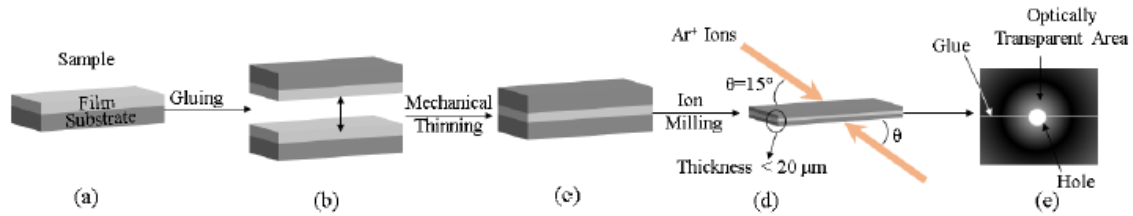


Figure 20: Different steps of TEM sample preparation. (a) A small rectangular piece of sample; (b) face to face gluing; (c) mechanical polishing; (d) small hole generation by ion milling; (e) birds eye view of the hole and transparent areas around it [86].

3.2 Optical characterization

3.2.1 Raman Spectroscopy

Raman spectroscopy was invented by C. V. Raman, is an essential tool in the field of vibrational spectroscopy [87]. It helps to investigate the crystallinity, strain, defects, and composition of the solids [86]. Raman spectroscopy studies the interaction between incident light or photon with lattice vibrations, phonons, or other excitations in the system. When a sample is exposed to a monochromatic light in the visible region, most of the photons are transmitted through the sample, some absorbed, and a very small portion is scattered by the material. The scattered beam is at the right angle of the incident beam and can have either the same frequency or different frequency of the incident beam. Depending on the frequency, the scattering process can be divided into Rayleigh scattering and Raman scattering. In Rayleigh scattering, the scattered beam frequency is the same as the incident beam frequency. If the scattered beam frequency is different from the incident beam frequency, then the scattering process is known as Raman scattering. Therefore, the Raman scattering is based on the inelastic scattering with a transfer energy between the molecule and scattered photon. In Raman scattering, stokes lines and anti-stokes lines are observed when the

scattered light loses or gains energy, respectively. The interaction of light and scattering processes is shown in Figure 21.

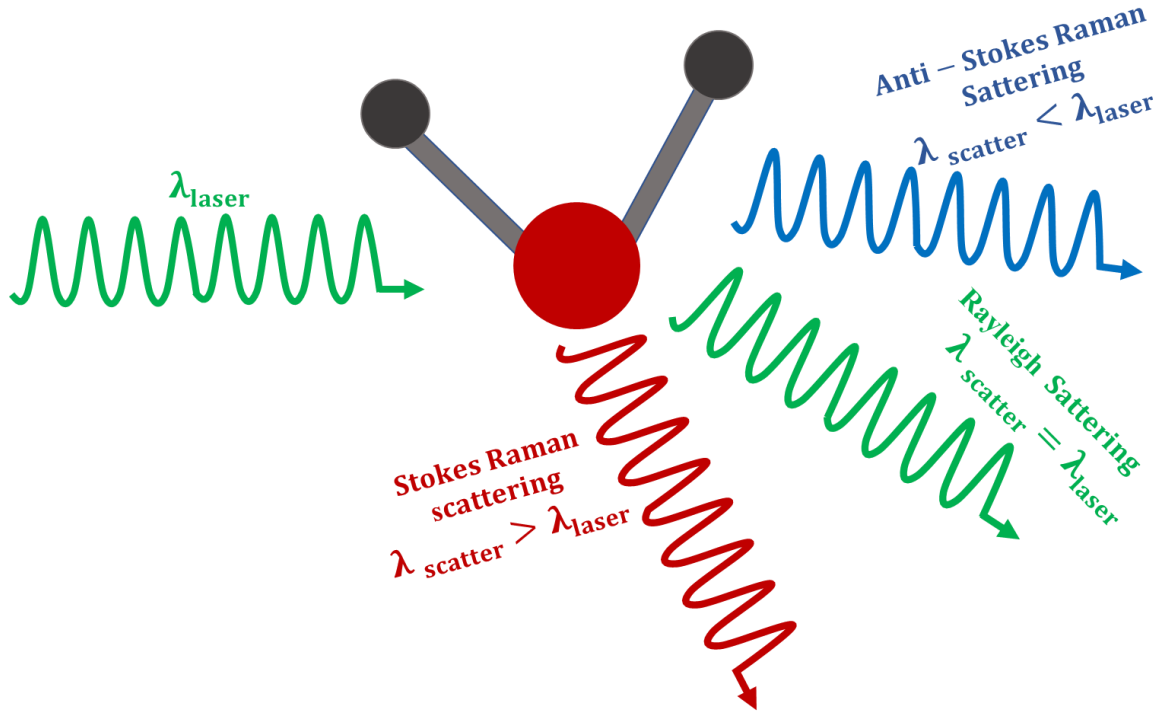


Figure 21: Three types of scattering that can occur when light interacts with a molecule.

Raman shift is calculated from the following equation by using the scattered light wavelength-

$$\Delta\theta = \left(\frac{1}{\lambda_0} - \frac{1}{\lambda_1}\right) \times 10^7 \text{ cm}^{-1} \quad \text{Equation 9}$$

where $\Delta\theta$ is the wavenumber Raman shift in cm^{-1} , λ_0 is the wavelength of the excitation laser beam in nm, and λ_1 is the wavelength of the scattered light in nm.

In this research Raman spectroscopy was used to confirm the crystallinity from the shape of the peak and strain from the shift wave number. In the Raman system, monochromatic light source either 532 nm green laser or 632 nm red laser could be utilized for the illuminating of the sample.

For the GaAs characterization, 632 nm monochromatic light source was used. The diameter of the spot on the sample is around $1\mu\text{m}$ and while the intensity is approximately 5 mW. From the schematic diagram of Raman spectroscopy as shown in Figure 22, the bandpass filters were used for the filtering of the unwanted background. The source light was directed from the source to the sample by aligning specific mirrors. The source beams were split into two directions by double beam splitters. The lenses were used for beam focusing and the reflected light was collected by a liquid nitrogen (LN) cooled charged coupled device (CCD) camera.

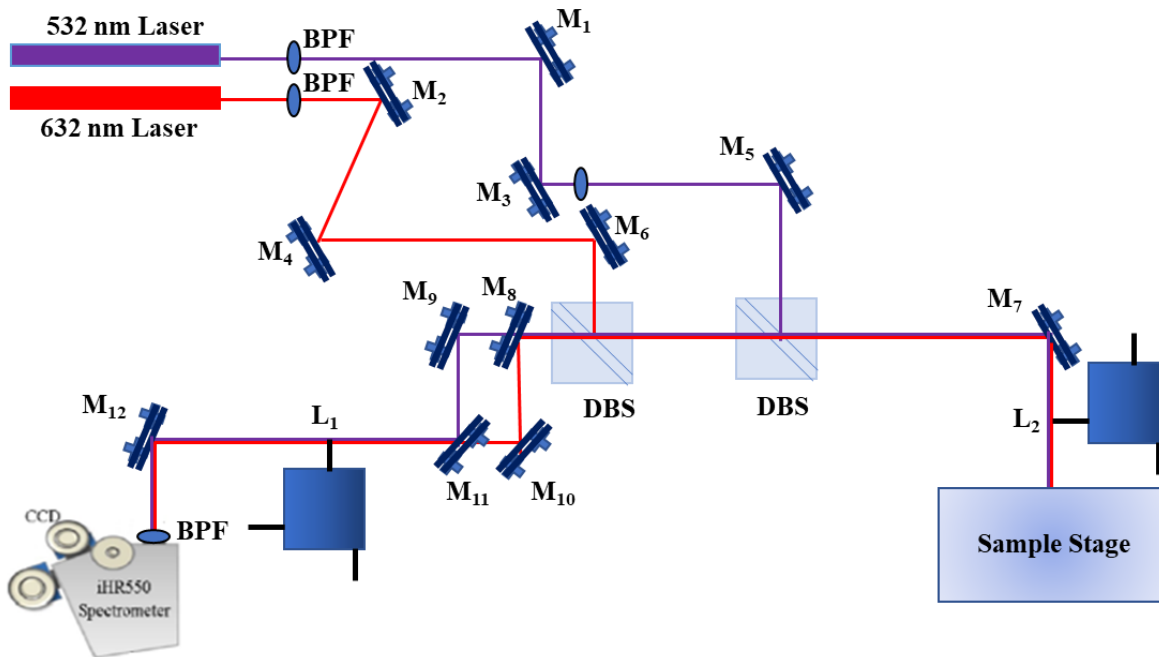


Figure 22: Schematic diagram of the Raman setup with 532 nm and 632 nm laser.

3.2.2 Ellipsometry

When a light reflects or transmits through the sample the polarization of the light changes according to the optical properties and thickness of the sample. Ellipsometry measures the polarization change and helps to characterize crystallinity, roughness, anisotropy, uniformity

thickness, doping concentration and other material properties related with a change in optical response [88]–[90]. It is a nondestructive, highly accurate and reproducible optical technique. The schematic diagram (Figure 23) of an ellipsometry shows a light source to illuminate the sample, a polarizer to pass light of specific polarization, a sample to be characterized, an analyzer to send different polarizations light to the detector, and a detector [91]. The polarization change is measured in terms of amplitude ratio, ψ and a phase difference Δ which are then used to determine the index of refraction and the thickness of the sample [92]. The complex reflectance ratio is calculated from the ψ and Δ ,

$$\rho = \frac{r_p}{r_s} = \tan(\psi) e^{i\Delta} \quad \text{Equation 10}$$

where r_p and r_s are the magnitudes of the two reflection coefficients of polarized light. The r_p is the perpendicular to the plane of incidence and r_s is the parallel to the plane of incidence. The Fresnel equations give,

$$r_p = \frac{E_{rp}}{E_{ip}} = \frac{n_1 \cos(\varphi_o) - n_o \cos(\varphi_1)}{n_1 \cos(\varphi_o) + n_o \cos(\varphi_1)} \quad \text{Equation 11}$$

$$r_s = \frac{E_{rs}}{E_{is}} = \frac{n_o \cos(\varphi_o) - n_1 \cos(\varphi_1)}{n_o \cos(\varphi_o) + n_1 \cos(\varphi_1)} \quad \text{Equation 12}$$

Here, air refractive index, $n_o=1$ and n_1 is the film refractive index. From the reflected light beam we can extract a lot of information about the film such as[93]-

The refractive index of the film can be calculated from the ellipsometric angles φ_o ,

$$\left(\frac{n_1}{n_o}\right)^2 = \sin^2 \varphi_o^2 \left[1 + \left(\frac{1 - \rho}{1 + \rho}\right)^2 \tan^2 \varphi_o^2\right] \quad \text{Equation 13}$$

The optical absorption of the thin film,

$$\alpha = \frac{1}{d} \ln \left(\frac{\sqrt{((1-R)^4 + 4R^2T^2)} - (1-R)^2}{4T^2R^2} \right) \quad \text{Equation 14}$$

where d , R , and T are the film thickness, reflectance, and transmittance, which can be calculated by-

$$d = \frac{\lambda}{2\sqrt{(n_1^2 - \sin^2 \varphi^2)}} = \frac{1}{2n_1 \Delta \left(\frac{1}{\lambda} \right)} \quad \text{Equation 15}$$

$$R = \frac{(n_0 - n_1)^2 + k_1^2}{(n_0 + n_1)^2 + k_1^2} \quad \text{Equation 16}$$

$$T = \frac{1 - R}{1 + R} \quad \text{Equation 17}$$

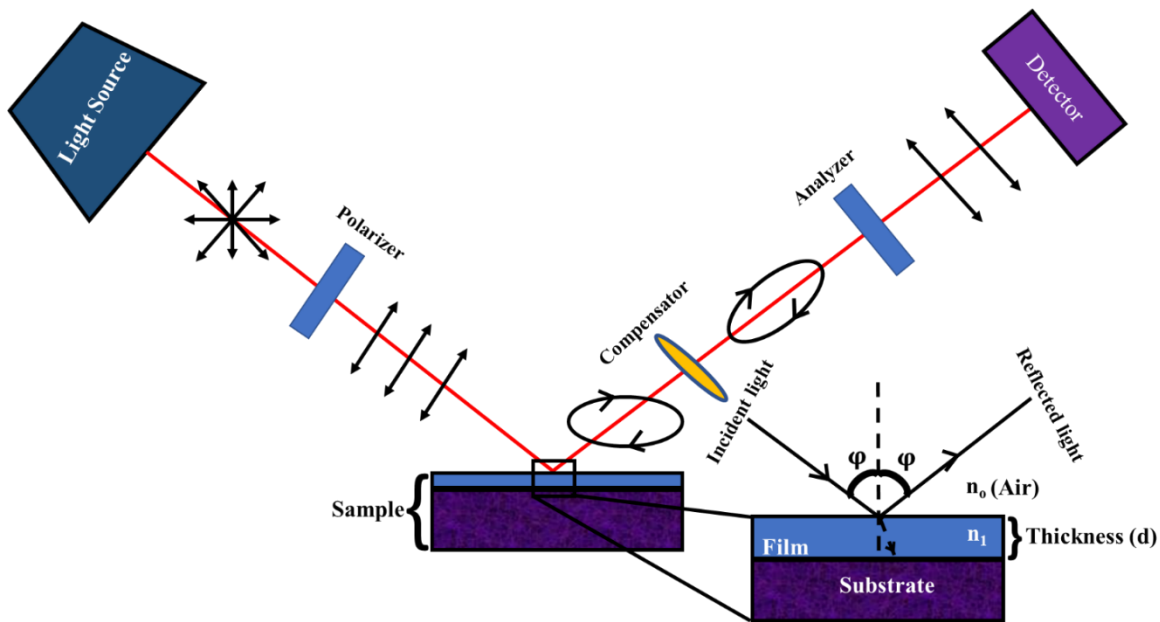


Figure 23: Schematic diagram of Ellipsometry basic concept. The refractive index of the sample influences the transmission of light.

In this research, a Variable-Angle Spectroscopic Ellipsometry (WVASE32) was used to characterize the samples. The spectroscopic data was collected in the range of 400-2000 nm (0.619-3.0996 eV) at different angle of incidence (65°, 70° and/or 75°) with a resolution of 10 nm. After measuring, the data were fitted using a built-in WVASE32® software. For minimizing the mean-square deviation χ^2 between experimental and theoretical results a Marquardt-Levenberg algorithm was used. The Mean Square Error (MSE) χ^2 is expressed as-

$$\chi^2 = \frac{1}{N} \sum_{i=1}^N (\text{Mes}_i - \text{Th}_i)^2 \cdot \frac{1}{\sigma_i^2} \quad \text{Equation 18}$$

where σ_i = standard deviation of the i^{th} data point, N = number of data points, Mes_i = measurement data of the i^{th} data point, Th_i = theoretical model the i^{th} data points.

Most of the time the grown sample was a multiple layer structure of GaAs and AlAs. Therefore, a multiple layer model consisting of sapphire substrate and film was used to analyze each sample. The Johs-Herzinger model was used to describe the dielectric function of each layer. The experimental result of ψ and Δ are compared with the model fit data of sapphire/AlAs/GaAs which are shown in Figure 24.

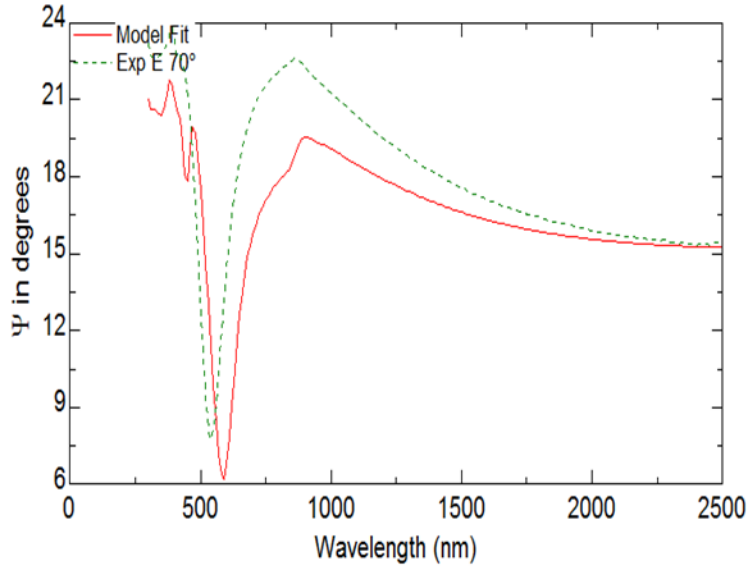


Figure 24: Experimental and model fitting ellipsometry data of GaAs/AlAs/sapphire sample.

3.2.3 Photoluminescence

Photoluminescence (PL) is a noncontact, nondestructive measurement technique. It is used to study the electronic and optical properties of the material. The bandgap, composition, carrier lifetimes, defects and quality of the material can be confirmed by analyzing the spectral distribution emitted by a semiconductor [94]. The basic mechanism of PL operation is explained below. A photon with energy equal or higher than the bandgap of the material, is absorbed by the material. The interaction of the photon and electron excites electrons to the higher energy state and creates a hole in the valence band [95]. The electron-hole pair is known as exciton [96]. The exciton can recombine mainly in three different ways (i) Radiative or band-to-band recombination; (ii) Shockley-Read-Hall (SRH or RHS) recombination; and (iii) Auger recombination. The radiative recombination occurs in the direct band gap semiconductor. In this process, the electron momentum is conserved, and the emitted photon has the energy equal to the bandgap energy of the material. The Shockley-Read-Hall recombination is also known as defect associated or trap

assisted recombination [97]. This recombination occurs in two-step process. In the first step, an electron is trapped by an energy state which is generated by foreign atoms or structural defects. In the second step, the recombination occurs if the hole moves up to the same energy state of the electron before the electron re-emitted to the conduction band [98]. Auger recombination is a nonradiative process and three carriers are involved in this recombination [99]. At first an electron-hole pair combines in a band-to-band transition and the excess energy is transferred to electrons or holes that are subsequently excited to higher energy states within the same band instead of giving off photons [100]. The schematic diagram of three recombination process is depicted in Figure 25.

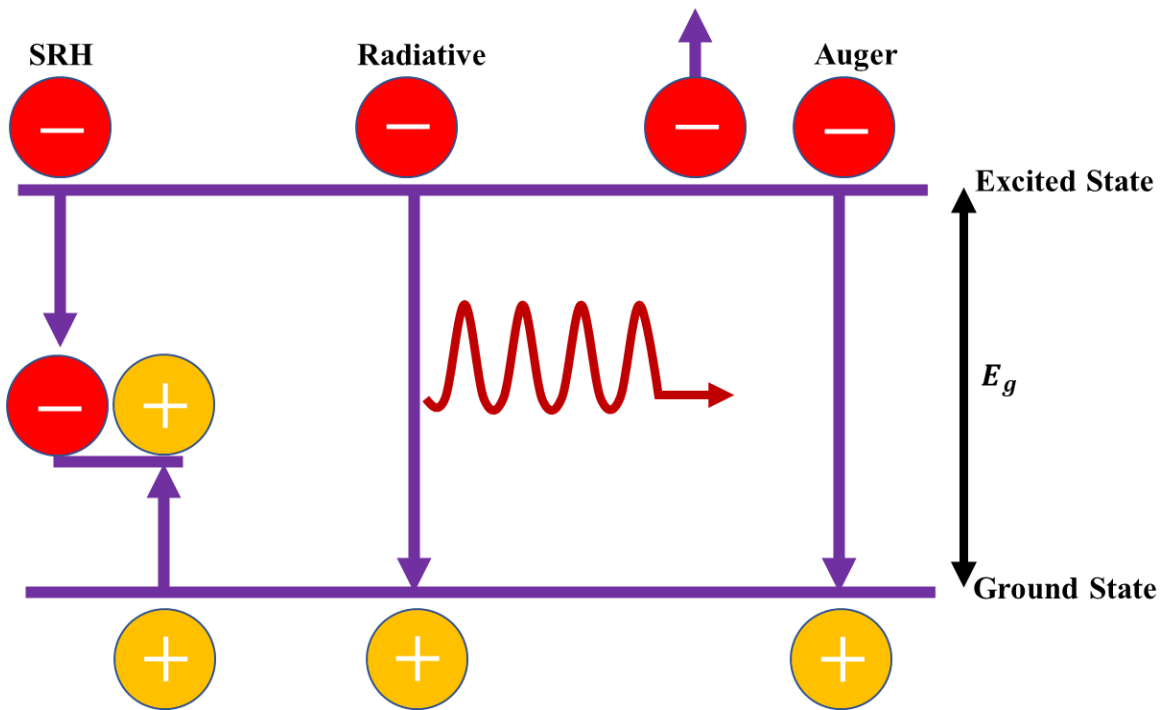


Figure 25: Graphical presentation of energy states, band gap and three recombination process.

In this research, a multifunctional PL system was used where six different light sources, such as 532 nm continuous wave (cw), a 1064 nm cw, 1550 nm cw, 2000 nm cw, 780 nm pulse Ti-

sapphire, Nd:YAG, and a fempto second laser were available to illuminate samples. Different measurements like off-axis PL and micro-PL at both low temperature and room temperature can be performed using separate collection paths. Detection of a wide range of wavelengths was facilitated with three different detectors, namely. PbS, InSb, and InGaAs. GaAs on sapphire system was studied by using a 532 nm continuous wave laser [101]. The laser spot size was 65 μm in diameter and the average pumping power was 500 mW [86]. The light source was modulated by an optical chopper as shown in the schematic diagram of Figure 26. The alignment of the laser beam to the sample was done by a set of pin holes, mirrors and the focusing was performed by a CaF_2 plano-convex lens with focal length of 10 cm. The planoconvex lens can transmit 90% of the incident light in the wavelength range of 500-5000 nm. A Horiba IHR 320 grating-based spectrometer was used to collect the PL emission from the sample and sent it to liquid nitrogen cooled InGaAs detector with the wavelength detection cutting-off at 2.3 μm . To amplify the electrical signal a lock in amplifier system with a chopper was used [96], [102], [103].

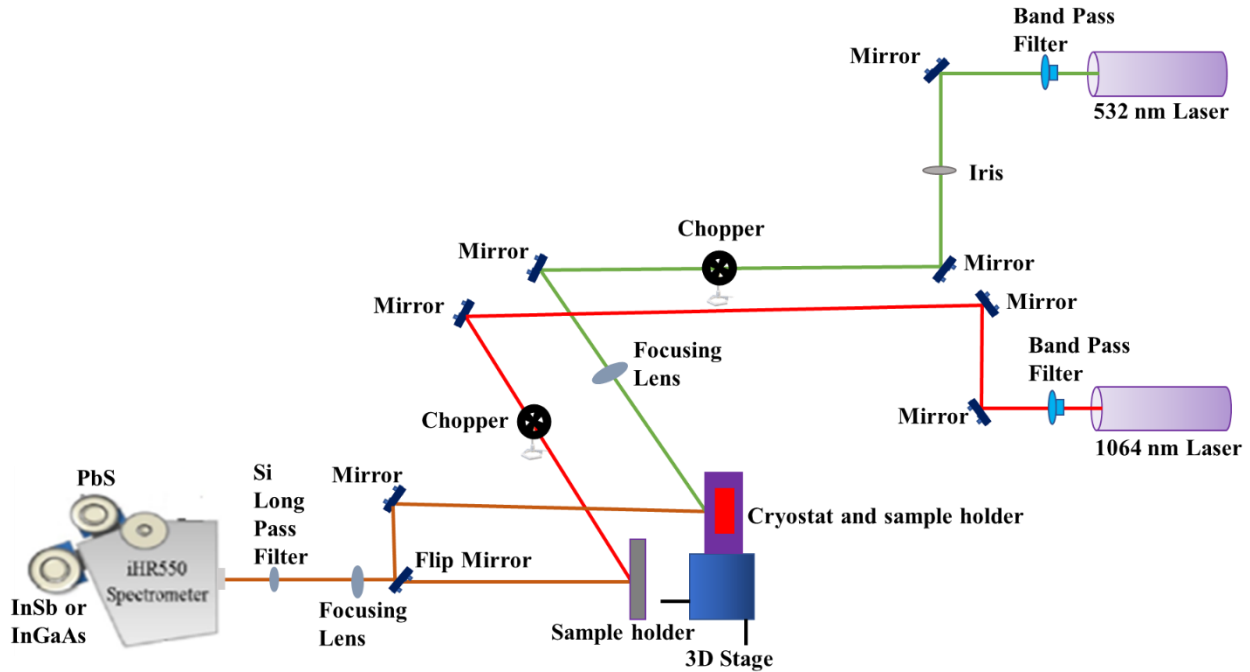


Figure 26: Schematic diagram of PL system setup. Two optical sources, detectors, beam alignment for both room temperature and low temperature measurements are illustrated and is not in scale.

3.3 Device Fabrication

3.3.1 GaAs Microdisk Fabrication on Al₂O₃ (0001)

The process of GaAs microdisk laser fabrication on c plane sapphire can be outlined into four main steps as shown in Figure 27. At first, each sample was sonicated with acetone and isopropyl alcohol. Then with the help of a spin coater machine a nominal 1.8 μm thick AZ4110 photoresist was placed on top of the GaAs film which allowed to settle microdisks. We have already confirmed from our trial experiments that 1.8 μm thickness is sufficient to withstand any wet chemical etching. Using a standard UV lithography with intensity 4.52 mW/cm², the chromium or glass mask pattern was transferred to the photoresist. The UV exposed regions of photoresist were developed by using a developer AZ300 MIF for 45 second.

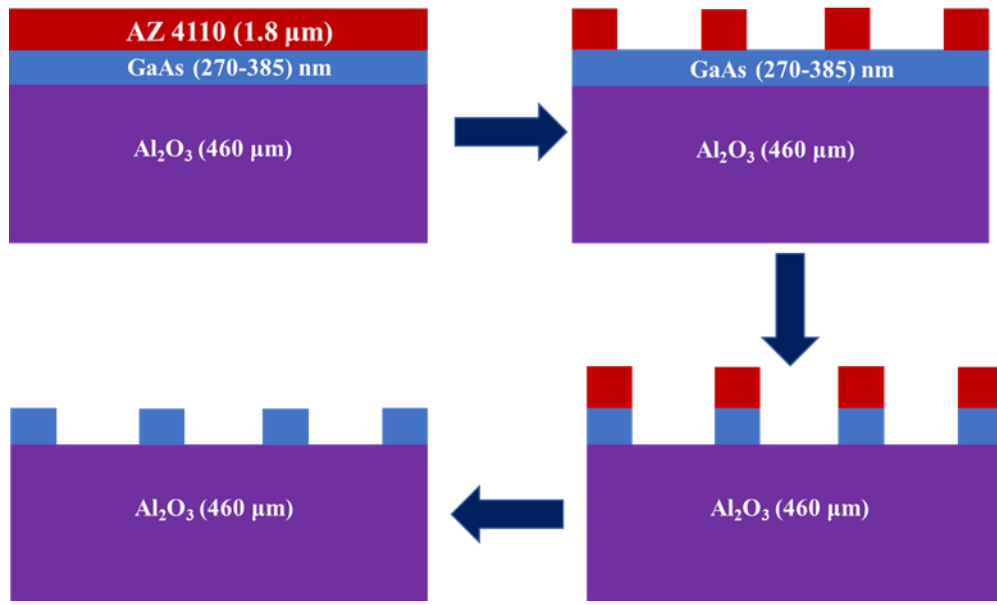


Figure 27: Four main steps of GaAs microdisk laser fabrication on sapphire substrate: (1) 1.8 μm AZ 4110 photoresist by spin coating; (2) pattern photoresist by optical lithography and developing; (3) wet etching by H_2SO_4 : H_2O_2 : H_2O =1:5:8 solution; (4) photoresist removed by acetone cleaning.

Then the GaAs etching was performed by an acid solution of H_2SO_4 : H_2O_2 : H_2O =1:5:8 at room temperature. The etching target was to reach sapphire substrate to remove the background contributions of GaAs to the responsivity measurement. The etching time was 1.18 s and etching depth was 89 nm. After the etching, the photoresist was removed by acetone cleaning. The optical imaging of the GaAs 16 μm micro disk lasers are shown in Figure 28.

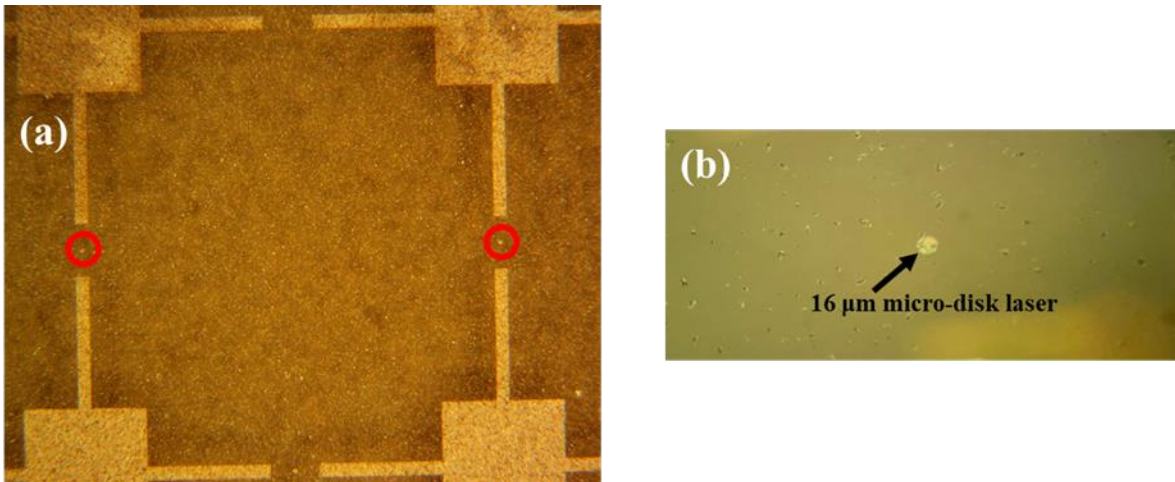


Figure 28: The optical image of (a) a small surface area after fabricating 16 μm micro disk lasers, red circles indicate the position of the disk, the rectangular boxes and long arms are for finding the position of the disks during measurements, (b) a 16 μm micro disk laser.

Chapter 4: Results and discussion

4.1 GaAs growth on c plane sapphire

4.1.1 Introduction

Heteroepitaxy is essential for introducing foreign properties on the epitaxial layer. In heteroepitaxy, the epitaxial material and substrate are different in lattice constant from each other but have the same crystal structure, such as cubic silicon, In(Ga)As on cubic GaAs [104]–[106]. On the other hand, in dissimilar epitaxy, both crystal structure and lattice constant of grown materials are different from the substrate, such as cubic SiGe and GaAs on the trigonal sapphire substrate [107], [108]. The differences between heteroepitaxial and dissimilar epitaxy are schematically shown in Figure 29. In my Ph.D. work, I worked on the growth of GaAs on c plane and r plane sapphire substrates. At first, I will discuss the nucleation of thin GaAs on c plane and later r plane sapphire substrates.

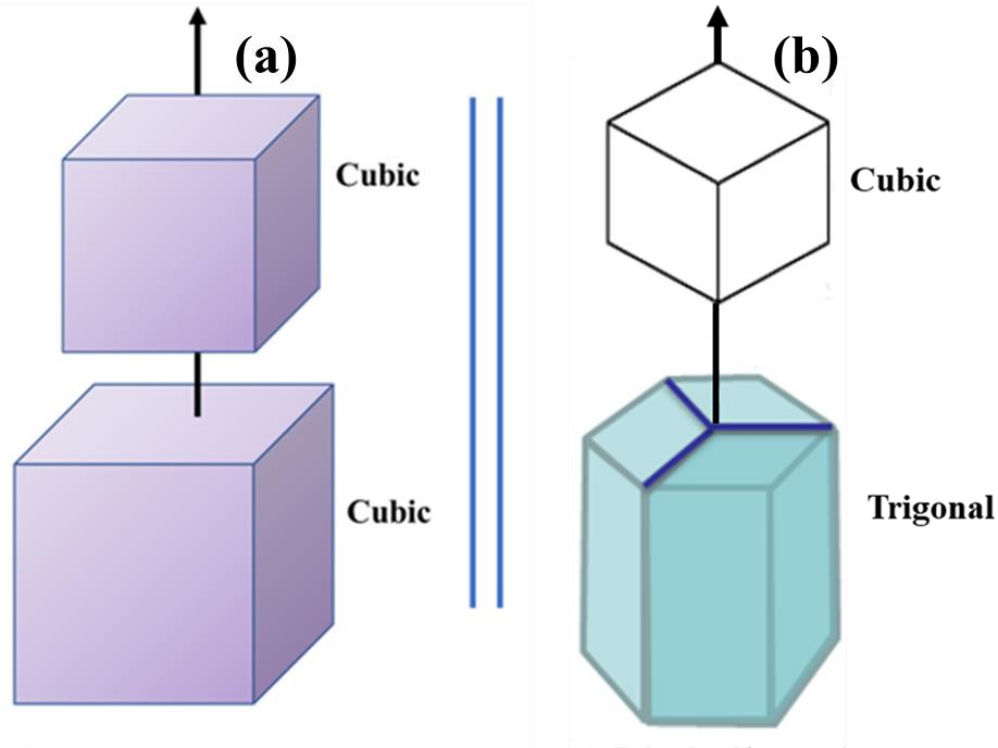


Figure 29: Schematic diagram of (a) heteroepitaxial, and (b) dissimilar epitaxy systems [108] .

I have already mentioned that all samples were grown by using a Riber-32 molecular beam epitaxy (MBE). Before the growth, substrates were annealed in air at 1200°C for 4 hours for the atomically smooth surface preparation. Figure 30 (a, b) shows the 2 $\mu\text{m} \times 2 \mu\text{m}$ AFM images of sapphire substrate as received and after annealing. After annealing, the substrate surface is atomically flat and clean where steps and terraces can be seen. The surface has step heights of 1 monolayer ($\sim 0.216 \text{ nm}$) and terrace widths around 200-300 nm. The unintentional miscut of substrates used was less than 0.1° , as calculated from Figure 30 (b). A line profile of the surface along the perpendicular direction of steps is shown in the top right inset of Figure 30 (b), where one monolayer high step can be easily seen. Bottom right inset of Figure 30 (b) shows the RHEED from the sapphire substrate just before the growth. Narrow streaks and Kikuchi lines validate the cleanliness of the prepared substrate. After annealing each substrate backside was coated with 1

μm Ti by electron beam evaporator. The coating was done for a specific reason. Sapphire is an insulating material with high band gap (~ 9 eV). During heating it transmits most of electromagnetic waves. Therefore, to absorb for efficient heating the substrate backside was Ti coated. Afterwards, substrates were inserted into the load lock chamber and heated at 200°C for two hours to evaporate water vapor. Then substrates were transferred to the degassing chamber and annealed at 850°C for six hours to remove organic contaminants.

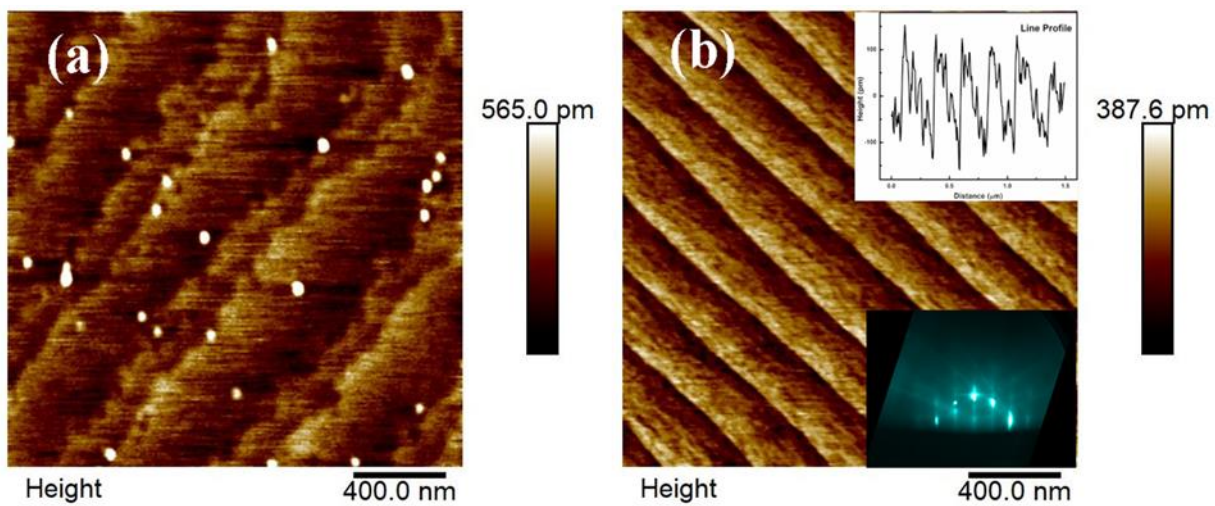


Figure 30: (a) AFM image of annealed sapphire substrate with prominent steps and terraces are shown; (b) line profiles of the image.

In the growth chamber to get a clean and free from unwanted materials substrates were heated to 900° for 3 hours. Before starting the growth, the substrates were exposed with arsenic flux of 2×10^{-6} torr at 650°C for half an hour [109]. Then the substrate temperature was fixed at growth temperature. The substrate temperature was measured by a thermocouple, and it was not in contact with substrates. Therefore, there can be 80°C to 100°C difference between measured temperature and thermocouple temperature. The growth rate of GaAs and AlAs was 0.75 and 0.2 ML/s respectively. The growth rate corresponds to homoepitaxial growth rate, and the V/III ratio was

15. The real time growth was studied by RHEED. In the following Table 1, details of the growth materials, growth temperature and substrate surface are listed.

Table 1: Structural details and growth parameters of samples presented in this work.

Sample ID	AlAs nucleation layer (NL)		GaAs layer		Substrate surface
	Growth temperature (°C)	thickness (nm)	growth-temperature (°C)	thickness (nm)	
C1	NA	NA	600	1	Corrugated
C10	NA	NA	600	10	Corrugated
C50	NA	NA	600	50	Corrugated
S1	700	5	600	10	Corrugated
S2	700	5	600	10	Weak step-terrace
S3	700	5	600	10	Step-terrace
T1	750	5	600	10	Weak step-terrace
T2	750	5	550	10	Weak step-terrace
T3	750	5	500	10	Weak step-terrace
S50	700	5	600	50	Corrugated
S50-annealed	700	5	600	50	Corrugated

4.1.2 Direct growth of GaAs/Sapphire

For the direct growth of GaAs on thermally cleaned c plane sapphire, we have grown three samples of thickness 1 (C1), 10 (C10), and 50 (C50) nm. The growth temperature was 600°C. RHEED

images at different stages of growth are shown in Figure 31. It shows a streaky RHEED pattern from atomically flat sapphire substrate (Figure 31 (a)). The kikuchi lines indicate the surface is clean and smooth. After introducing 1 nm GaAs on clean and smooth substrate, the intensity of the streaks is reduced; ring patterns and spots are observed (Figure 31 (b)).

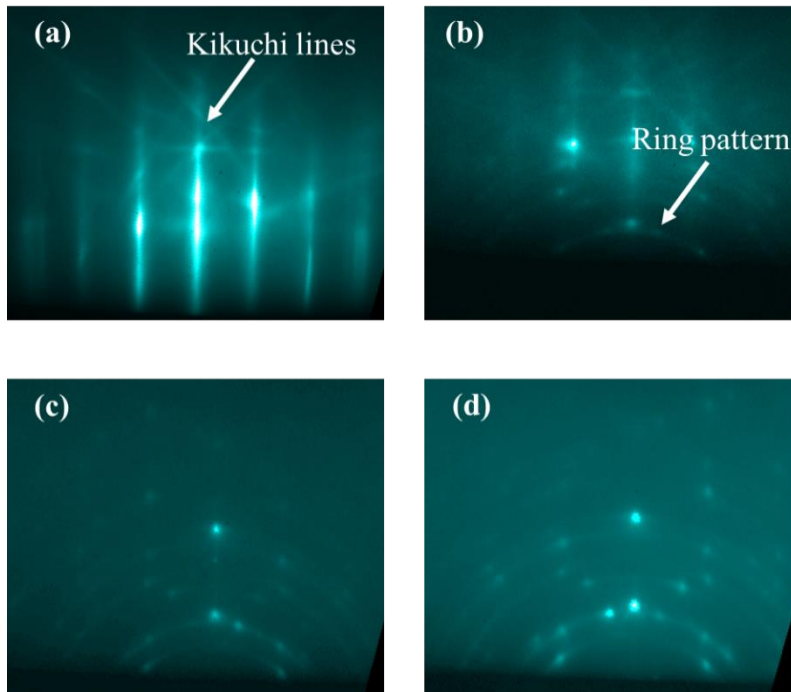


Figure 31: RHEED images (a) from atomically flat sapphire substrate; after (b) 1 nm, (c) 10 nm, and (d) 50 nm GaAs deposition.

The Kikuchi lines are still observed which indicate that most of the substrate surface are uncovered. With increasing thickness, the streaky lines are disappeared, ring pattern and spotty features become prominent as shown in Figure 31 (c, d). The ring patterns indicate the weak in plane correlation between film and substrate, whereas the spotty pattern indicates the 3D growth mode. From the starting of the GaAs growth, spotty features are observed which indicate the direct growth of GaAs that follows Volmer-Weber (VW) growth mode. This happens due to large lattice mismatch, relatively small surface energy of the sapphire substrate with respect to GaAs, and high

interfacial energy. The 3D islands growth with little attachment to the sapphire substrate and by light brushing the GaAs islands could be easily knocked off from the growth surface. Hence, growth is not commensurate in its strict sense. Interface bonding so weak due to dissimilar crystal structure that overgrown layer merely feel the underlying substrate, somewhat like van der Waals epitaxy [110]–[112]. Figure 32 shows the $5\ \mu\text{m}\times 5\ \mu\text{m}$ AFM images of GaAs islands of three different thicknesses. The height and average lateral size of GaAs islands increases with increasing deposition while the density of islands was decreasing. These values are listed in Table 2. These follow the nucleation theory where Ostwald ripening, and coalescence reduce density and increase islands height due to the increased growth time [23], [28]. The facets of the islands from the AFM image indicate the crystallinity of the materials.

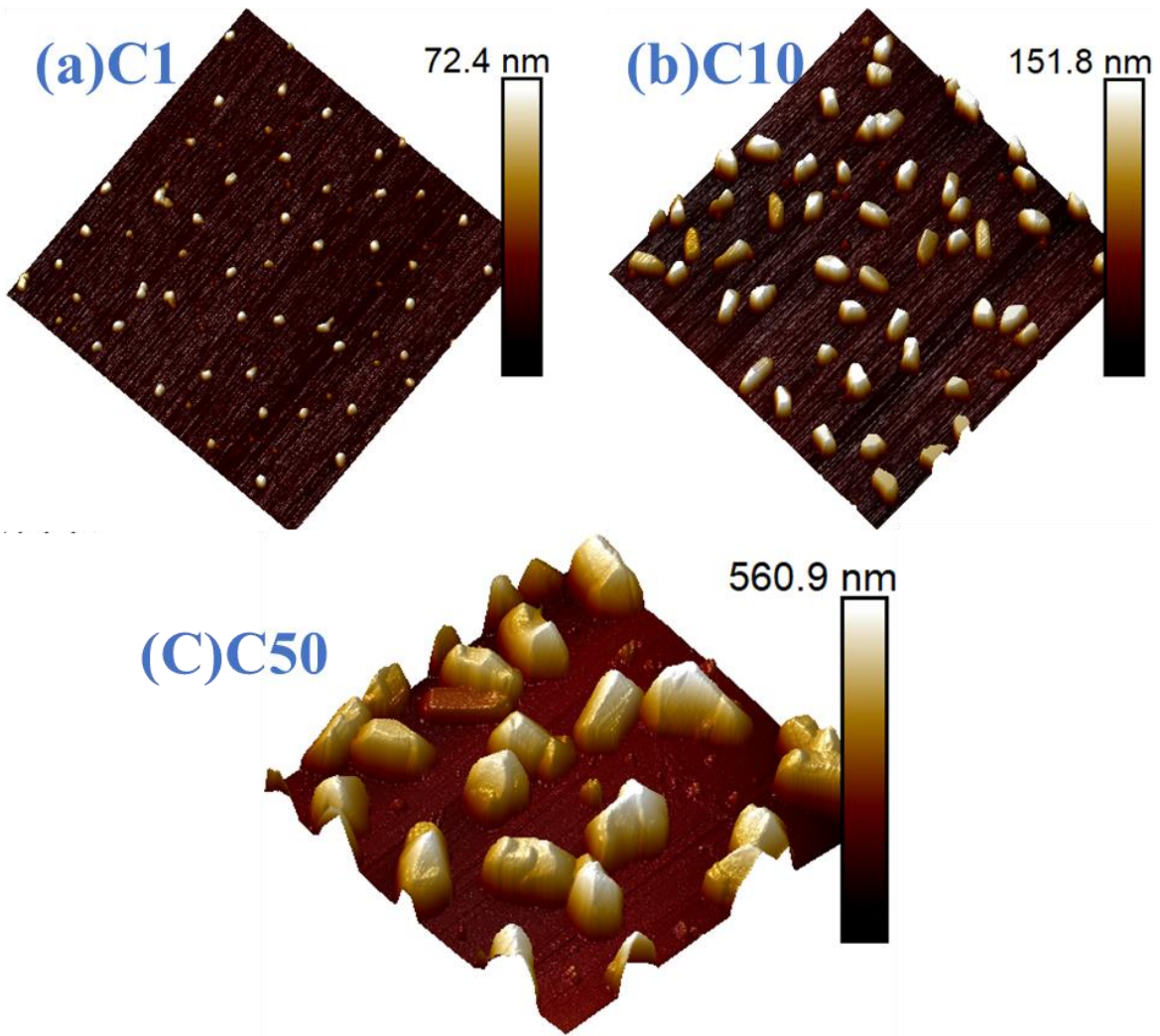


Figure 32: AFM images of samples (a) 1 nm GaAs, (b) 10 nm GaAs, and (c) 50 nm GaAs.

Table 2: GaAs island size, density, and percentage surface coverage with a deposition amount.

GaAs nominal thickness (nm)	Density (cm ⁻²)	Height (nm)	Average lateral size (nm)	Island coverage (%)
1	2E8	63.15	186.4	20
10	2.56E8	117.8	225	50
50	7.5E7	173	475	80

To confirm the growth direction, we performed the XRD ω - 2θ scan for all three samples. Due to the small amount of the C1 and C10 samples we could not get any diffraction. For the C50 sample, the growth direction is along [111] with a small peak (220), as shown in Figure 33 (a). The sharp peak intensity is observed from the substrate. The rocking curve or omega scan is a useful way to investigate the crystal quality. The small FWHM of the rocking curve indicates the less deviation of crystal planes from their ideal position. It is highly sensitive to the defects like mosaicity, dislocations, strain, and curvature because it disrupts crystal planes perfect parallelism. The FWHM of the rocking curve for the (111) plane versus the GaAs thickness is plotted in Figure 33 (b). The PL was done at 10K (Figure 33 (c)), where free exciton emission is observed at 1.514 eV. The emission also supports the high-quality GaAs islands growth, with the lower energy peaks likely due to defect states, possibly at the interface.

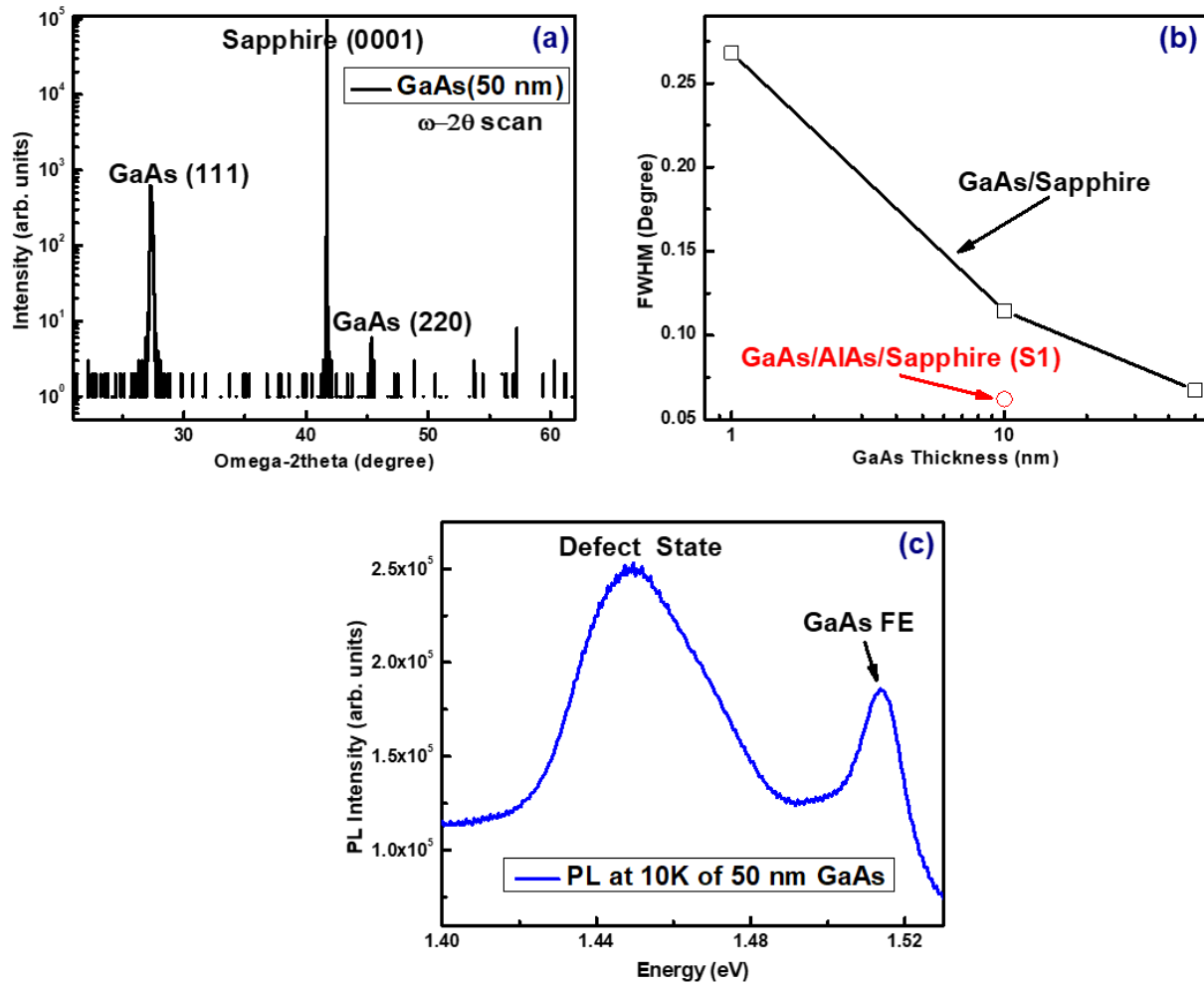


Figure 33: (a) out of plane measurements of 50 nm GaAs (b) FWHM of (111) rocking curve versus GaAs thickness (c) Low-temperature PL from 50 nm GaAs (C50). This indicated improved crystal quality with increased growth and using an AlAs 5 nm nucleation layer (in red) discussed below.

To find the in-plane correlation between film and substrate, we have done the asymmetric (220) phi scan of GaAs. As shown in Figure 34 (b), six broad peaks indicate the weak in-plane correlation between film and substrate. Since GaAs has a cubic crystal structure so it should show three-fold symmetry in 360° ϕ rotation. However, Figure 34 (b) shows six peaks are 60° separated from each other. The extra three peaks are twin domains of GaAs (111) crystal which are separated by 120° .

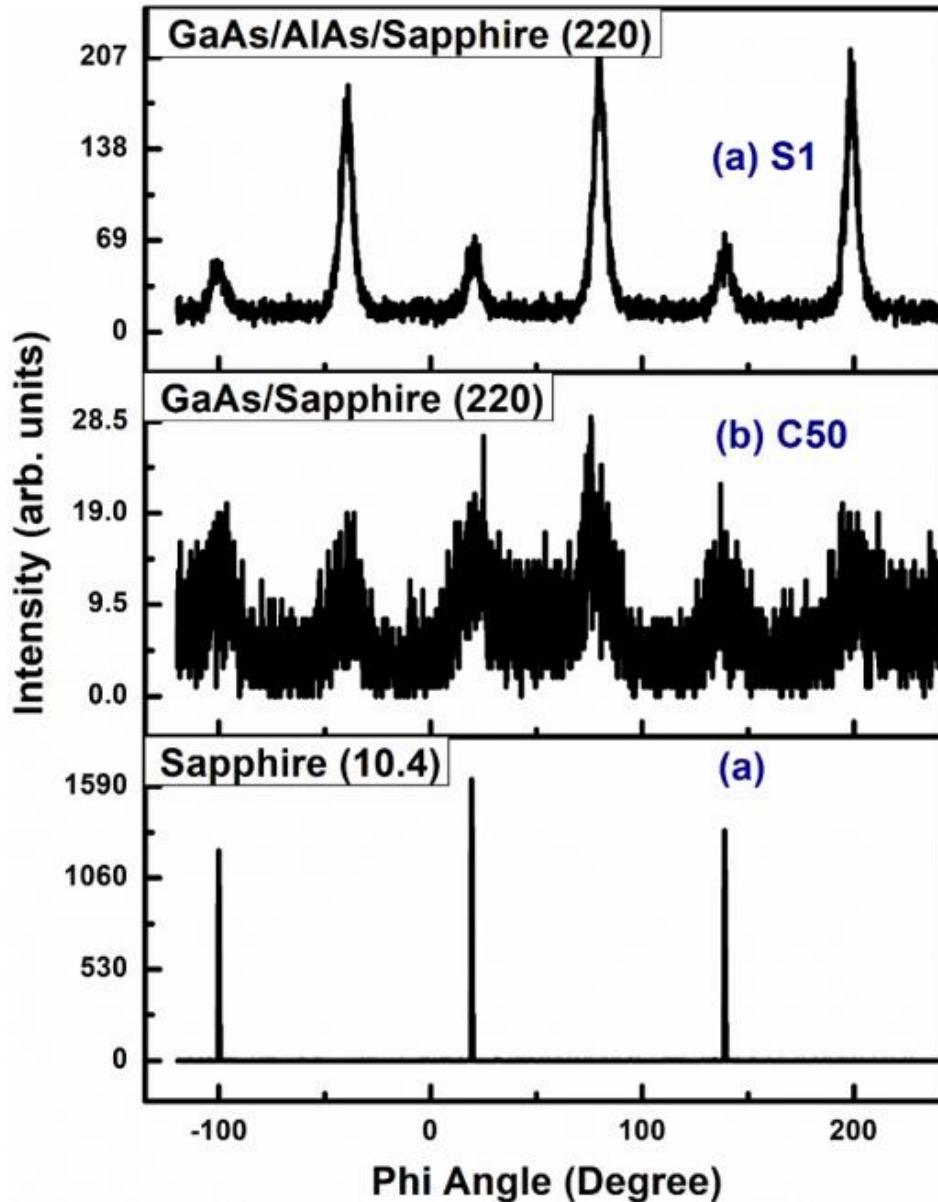


Figure 34: phi scan of (a) (10.4) plane of sapphire and (b) (220) plane of GaAs/Sapphire (C50) and (c) GaAs/AlAs/Sapphire (S1). This indicates reduced twinning with an AlAs 5 nm nucleation layer.

We assume the high-quality 3D islands of GaAs and random twin distribution are due to the weak correlation with the sapphire substrate. For example, very often during growth of semiconductor on oxide substrate with high lattice mismatch and interface energy promotes misfit dislocations at the interface as soon as critical nuclei form. After generating misfit dislocations, the growth

materials become relaxed, and the subsequent materials grow at their bulk lattice with low levels of strain [113]. Since the misfit dislocations are confined at the interface and do not propagate through the film, the result can be high-quality GaAs islands as shown by XRD images (Figure 33 (b)). Therefore, based on the lattice mismatch and the weak chemical interaction, the sapphire acts as a compliant substrate in these early investigations.

4.1.3 Introduction of thin AlAs nucleation layer

The direct growth of GaAs on c-plane sapphire produces high-quality materials. However, substrates surface coverage was low where GaAs islands had 50% twinning defect, weak interfacial correlation, and more than one growth direction. To overcome the GaAs/sapphire system's structural difficulties, we introduced a thin (5 nm) AlAs as a nucleation layer between the GaAs and sapphire substrate. The almost same lattice constant of AlAs and GaAs motivated us to choose AlAs as a nucleation layer. Figure 35 (a) and (b) show the real-time growth images of direct growth of the AlAs on sapphire and GaAs growth on top of AlAs/sapphire system. For the AlAs growth, after opening the aluminum cell shutter, a spotty pattern was observed with a gradual disappearance of sapphire substrate streaks. The instant in-plane relaxation of the AlAs was observed from the spot's position different from the sapphire substrate streak. RHEED images show two spots are very close to each other, and one has a higher intensity than another. These spots arise from a single plane and indicate the formation of one original preferential phase with a suppressed twin phase ("O" represents the original phase and "T" represents the twin phase in Figure 35 (a)). The surface morphology of these structures is studied by AFM, as shown in Figure 36, depending on the starting substrate.

not contribute to the x-ray diffraction due to the small volume. With the presence of AlAs, the FWHM of GaAs grown on sapphire is as low as 220 arcsec (shown in Figure 33 (b)). From the phi scan, as shown in Figure 34, we have observed the twining of GaAs/AlAs/sapphire system is less than GaAs/sapphire system. A better in-plane correlation between substrate and film was also observed in GaAs/AlAs/sapphire system. The reduction of twining after AlAs nucleation layer insertion could be related to the wetting and coalescence of AlAs islands. The twining during direct growth of GaAs on sapphire can be related to the individual's islands and their equal probability of being any twin phases without preference. Therefore, we have seen 50% twining in the case of GaAs/sapphire system. For the AlAs nucleation layer, small islands coalescence, and wet the substrate during the early stage of growth. The reduction of twin could happen during the coalescence of 3D islands, where one twin phase can dominate to another and expand at the expenditure of another twin phase. This is similar with the case of cubic SiGe growth on trigonal c plane sapphire, where micro-twin lamellas and a significant reduction of twin volume have been reported for thick continuous SiGe layer after island coalescence had been explained by successive gliding of the Shockley partial dislocations (surrounding each twin region) on the adjacent glide planes [115], [116]. Together, these results show that the AlAs nucleation layer in between GaAs and sapphire improves the substrates wetting, twining, in-plane correlation, and results in a better overall quality of GaAs [23]. It should be mentioned that the improvement occurs due to a better chemical interaction between the AlAs and sapphire substrate than the GaAs and sapphire substrate [23].

4.1.4 Effect of Pre-growth Substrate Surface Treatment

An atomically flat and clean substrate with step-terraces surface plays an essential role for the improvement of the crystal quality [23]. The substrate preparation before the deposition of epilayer has been effective in reducing twinning [78]. Higher step density enhances the incoming adatoms' nucleation and promotes layer-by-layer growth mode. For example, in heteroepitaxial systems, the step-terraces substrate surface is well-known to control the film's quality and orientation [117], [118]. We have noticed that the sapphire substrate treatment before the growth influences the GaAs film quality. To study the effect of the substrate surface on III-V growth, we have used three different kinds of substrate surface: (a) a corrugated substrate surface with no step-terrace structure (S1); (b) a weakly-defined step-terrace surface (S2), and (c) a well-defined step-terrace surface (S3) [23]. We have grown 5 nm AlAs as a nucleation layer followed by 10 nm GaAs on each substrate under the same growth condition. The surface morphologies are investigated by AFM images, as shown in Figure 36. Substrate surfaces cover deposited materials for all three samples, and the lowest surface roughness is observed for the substrate having a well-defined step-terrace surface. Also, from the comparison of real-time growth as shown in Figure 36 (row III and IV), the streakier RHEED pattern is observed for the well-defined step-terrace substrate sample. During growth on the step-terrace surface, the surface reconstruction was observed for both AlAs and GaAs. For the GaAs (111) crystal plane, there are two surface reconstructions, GaAs (111)A and GaAs (111)B, which are observed. In GaAs (111)A and GaAs (111)B, the surface is Ga and As is terminated, respectively. Between these the surface reconstruction of GaAs (111)B changes with growth temperature while the surface reconstruction of GaAs (111)A remains invariant. For GaAs (111)B (1×1) , (2×2) , and $(\sqrt{19}\times\sqrt{19})$ are the usual surface reconstruction but for GaAs (111)A only (2×2) surface reconstruction is observed [119]–

[127]. During GaAs growth on sapphire, a (2×2) surface reconstruction is observed, and it remains invariant at different growth temperatures, which is similar to the homoepitaxial growth of GaAs (111)A [128]. Therefore, for our grown samples, the orientation of the GaAs layer is $(111)A$.

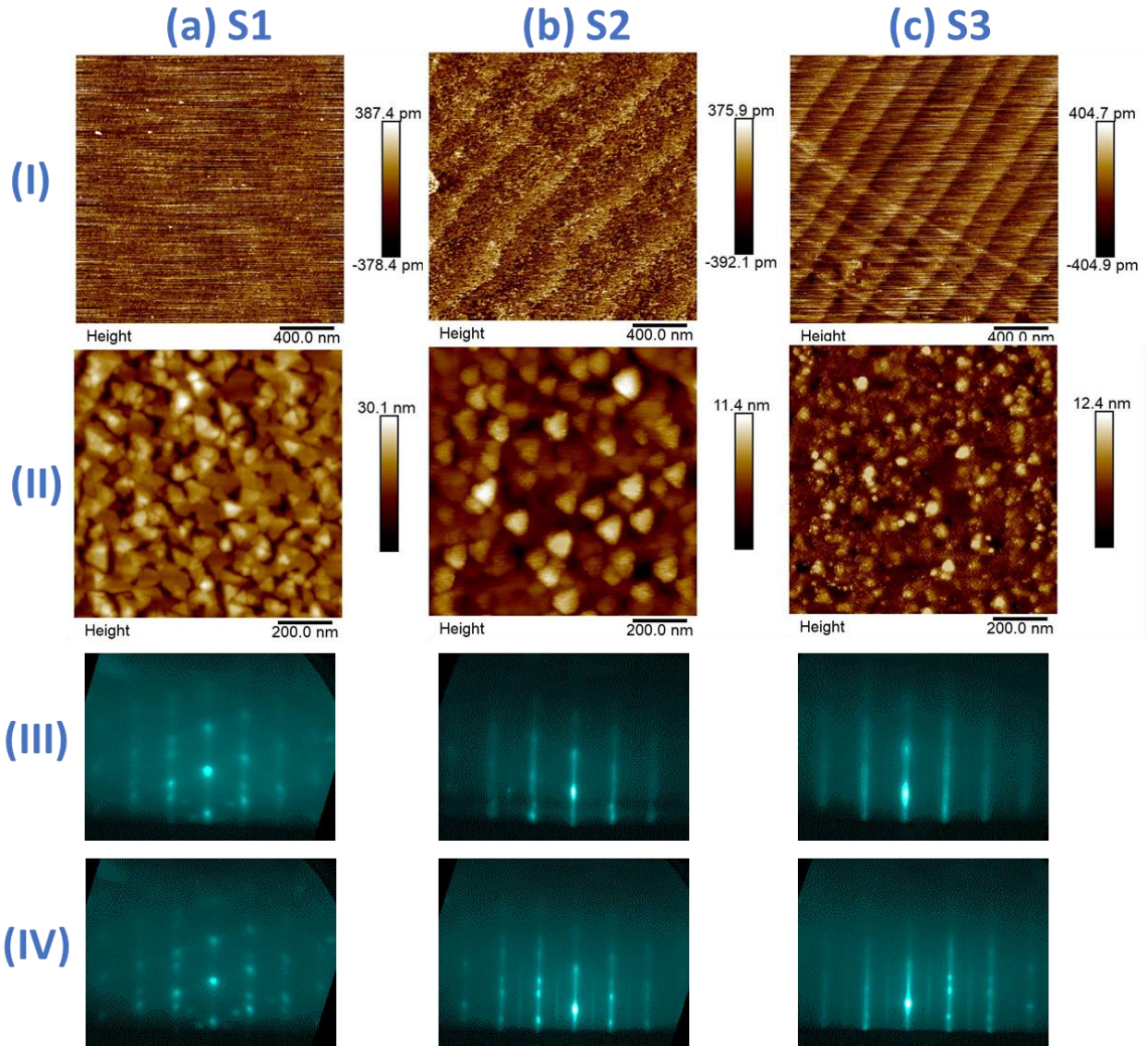


Figure 36: Columns show the data for (a) corrugated surface sample, (b) weakly defined step-terrace surface sample, and (c) well-defined step-terrace surface sample. Row (I) is an AFM image of the initial sapphire substrate; Row (II) is an AFM images of the GaAs film; Row (III) is the RHEED pattern after AlAs growth, while Row (IV) is the RHEED pattern after GaAs growth. Both (a) and (b) RHEED patterns indicating twinning, while the RHEED pattern in (C) indicate that twinning is absent only for AlAs (row III) growth.

The twin volume of all three samples of GaAs (220) crystal plane is determined from the phi scan as shown in Figure 37 (a). It shows the twin volume is the same for all samples. Therefore, we can conclude that the twinning of the GaAs/sapphire system does not affect that much by the initial substrate surface. If we closely look at the (220) peak is sharper for the well-defined step-terrace substrate sample than the other two. It indicates a stronger in-plane correlation between substrate and film. This finding also is supported by the ω - 2Θ scan of three samples where fringes are observed only for the surface with step-terraces (Figure 37 (b)). Fringes arise from the higher quality heterointerfaces. Rocking curves (Figure 37 (c)) show the intensity dispersion at the base for all three samples. The highest dispersion is observed for GaAs on the corrugated substrate, and the lowest dispersion is observed for GaAs on a well-defined step-terrace surface. Each rocking curve can be fitted with two Gaussian curves: one is having smaller intensity and larger linewidth while the second is having larger intensity and smaller linewidth (shown in the inset of Figure 37(c) for sample S1) [23]. The most reasonable explanation for this behavior is that two peaks arise from two different materials. The broader peak originates from a thin AlAs nucleation layer and a sharp peak from the thicker GaAs. This is difficult to test but the fitting consistently shows a small shift for the broader peak towards large lattice constant [23]. The GaAs on step-terrace substrate shows better in-plane correlation and higher quality heterointerface, which can be explained by nucleation via stronger interaction with the substrate at step edges.

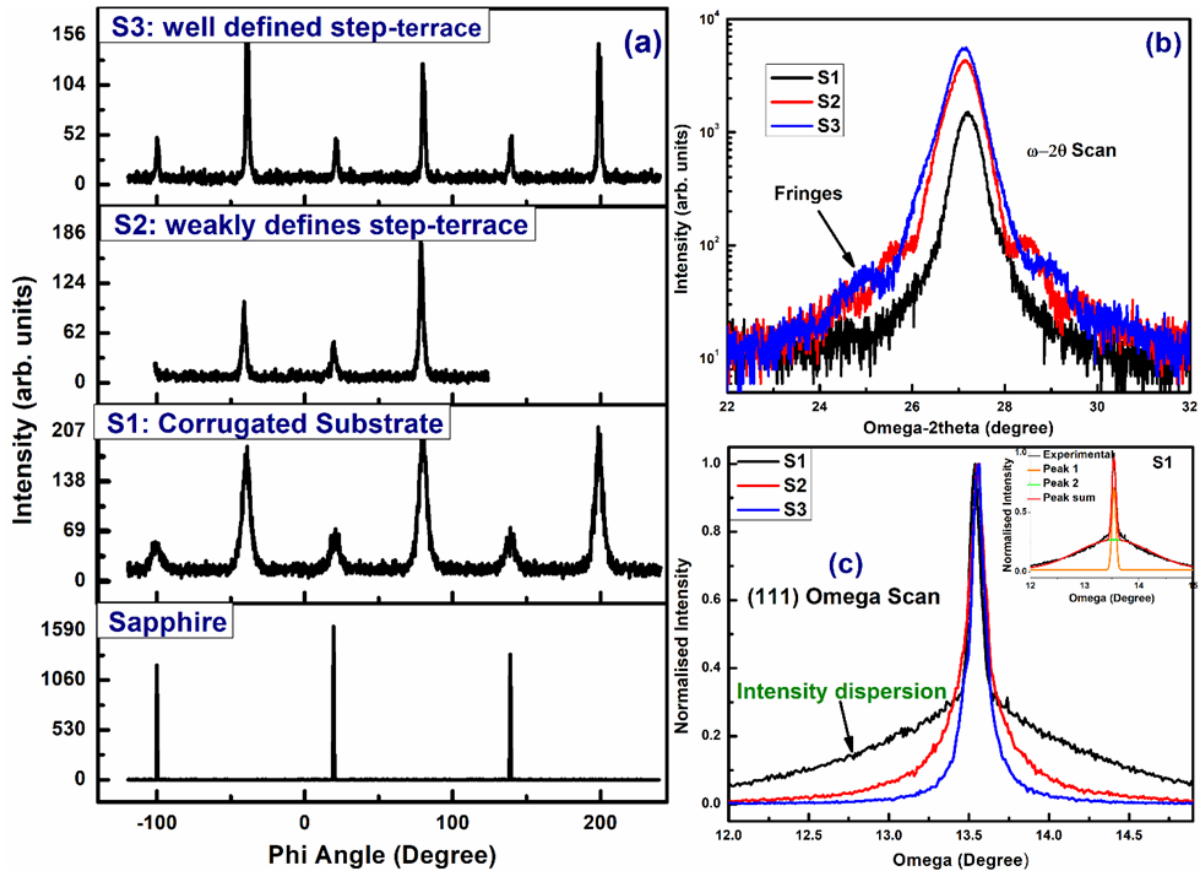


Figure 37: (a) phi-scan, (b) (111) omega-2theta scan, and (c) (111) omega-scan of samples grown on the different starting substrate surfaces. Inset in the Figure 37(c) shows the Gaussian fitting of omega-scan of S1 into two peaks having different broadness.

4.1.5 Effect of growth temperature

The quality of epitaxial layers is influenced by different growth parameters such as growth temperatures, V/III ratio of beam fluxes, growth rate, and an atomically flat substrate. Early reports of homoepitaxial growth of GaAs (111) give evidence of the importance of growth parameters, predominantly temperature, for the high-quality materials growth [129]–[131]. To study the effect of growth temperatures on the GaAs film quality, twinning, surface morphology, and film substrate correlation, 50 nm GaAs on AlAs/sapphire was grown at three different growth temperatures which were chosen: namely, 600°C (T1), 550°C (T2), and 500°C (T3). The 2 μm × 2 μm AFM

images show the surface morphology of these samples, as shown in Figure 38. The triangular-shaped hillocks are observed on these samples, which are characteristic of GaAs (111) growth [128][132]. The root mean square roughness of these samples grown at 600°C, 550°C, and 500°C, are 4.59, 1.7, and 3.72 nm, respectively. Among these samples, the lower density of hillocks and smooth surface is observed for the sample grown at 550°C.

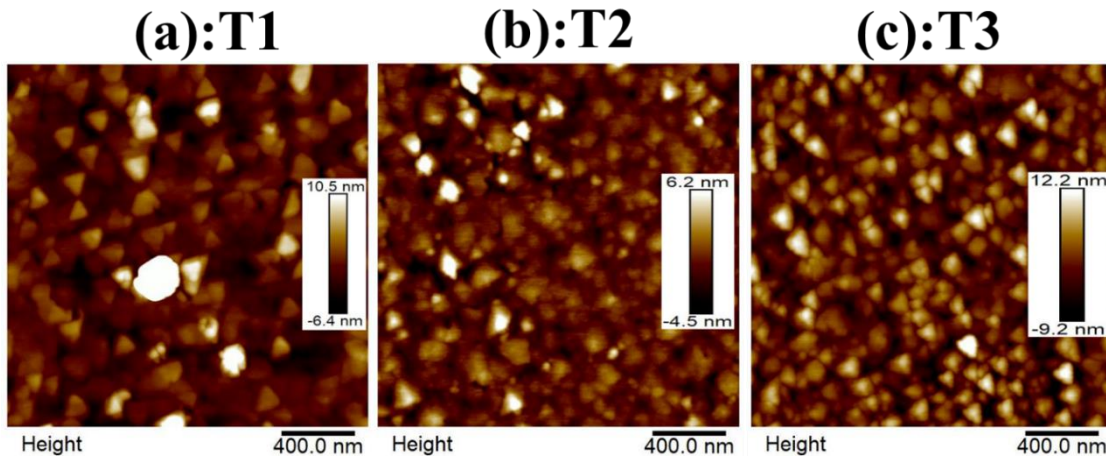


Figure 38: AFM images of GaAs samples grown at three different growth temperature (a) 600°C (T1), (b) 550°C (T2) and (c) 500°C (T3).

Phi-scans (Figure 39) show that twinning existed in all three samples, and the growth temperature affect twinning considerably. The highest twin volume is observed for the sample grown at relatively low temperature (500°C). Out of plane measurements in Figure 39 (b) show only (111) crystal orientation. The abrupt heterointerface can be confirmed in all three samples from the fringes. It is also noted that the fringe spacing decreases with the temperature indicating that the thickness of the GaAs layer is certainly dependent on the growth temperature. The FWHM of the rocking curves (Figure 39 (c)) of GaAs around [111] direction has almost the same value, which indicates that the crystal quality is the same in all three samples.

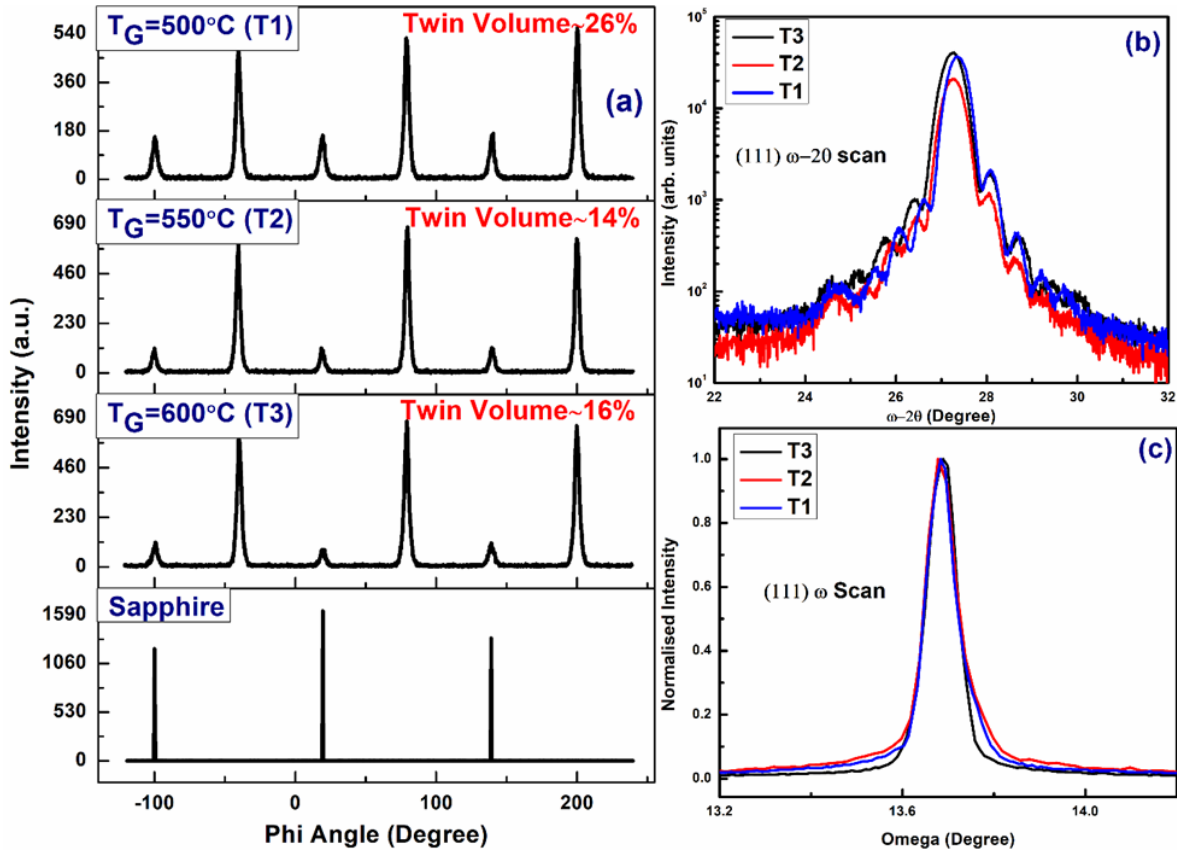


Figure 39: (a) (220) phi-scan, (b) (111) omega-2theta scan, and (c) (111) omega-scan of samples grown on different growth temperatures.

4.1.6 Effect of in-situ annealing

The annealing can improve both the surface and the bulk of the grown film of heteroepitaxial systems [133]–[135]. In this work, in-situ annealing was performed at the end of GaAs (50 nm) growth on AlAs/sapphire under As₂ overpressure to investigate its effect on crystal quality, twinning, surface, and bulk properties of GaAs. Figure 40 (a) and (b) show the RHEED patterns before and after in-situ annealing of 50 nm GaAs on the AlAs/sapphire (S50). The annealing was done at 800°C for 1 minute under arsenic overpressure. The RHEED image shows a spotty and twinning before annealing, while the streaky plus spotty RHEED pattern is observed after annealing. The streaky plus spotty pattern indicates the rough surface with a large flat area. After

annealing, no observable twinning is observed in the RHEED pattern, and the reconstruction streaks appear, which indicate a quality smooth surface. AFM image of S50, shown in Figure 40 (c), shows the characteristic pyramidal features. AFM images in Figure 40 (d) and (e) show the same in-situ annealed samples' surface morphology. The in-situ annealed sample shows the appearance of surface pits with an otherwise smooth surface. Spots in the RHEED for this surface is due to the surface pits.

Triangular (which is small in size) and irregular-shaped (big in size) pits are observed in the AFM images of the S50 annealed sample. The possible reason for the larger irregular pits is the agglomeration of multiple triangular-shaped pits or expansion of these triangular pits laterally due to desorption [23]. The triangular base stacking fault is very common during the growth on GaAs (111)A, and it grows into 3d stacking fault tetrahedron (SFT) [136]. Twin features are observed due to these SFTs, and they are thermodynamically unstable possibly due to their small size and defect boundary. As a result, the SFTs region material can be evaporated at the annealing temperature and formed triangular pits. Supporting this explanation, the pits surface area is a similar fraction of the total surface area indicating that the minor twin has evaporated leaving only the original phase behind.

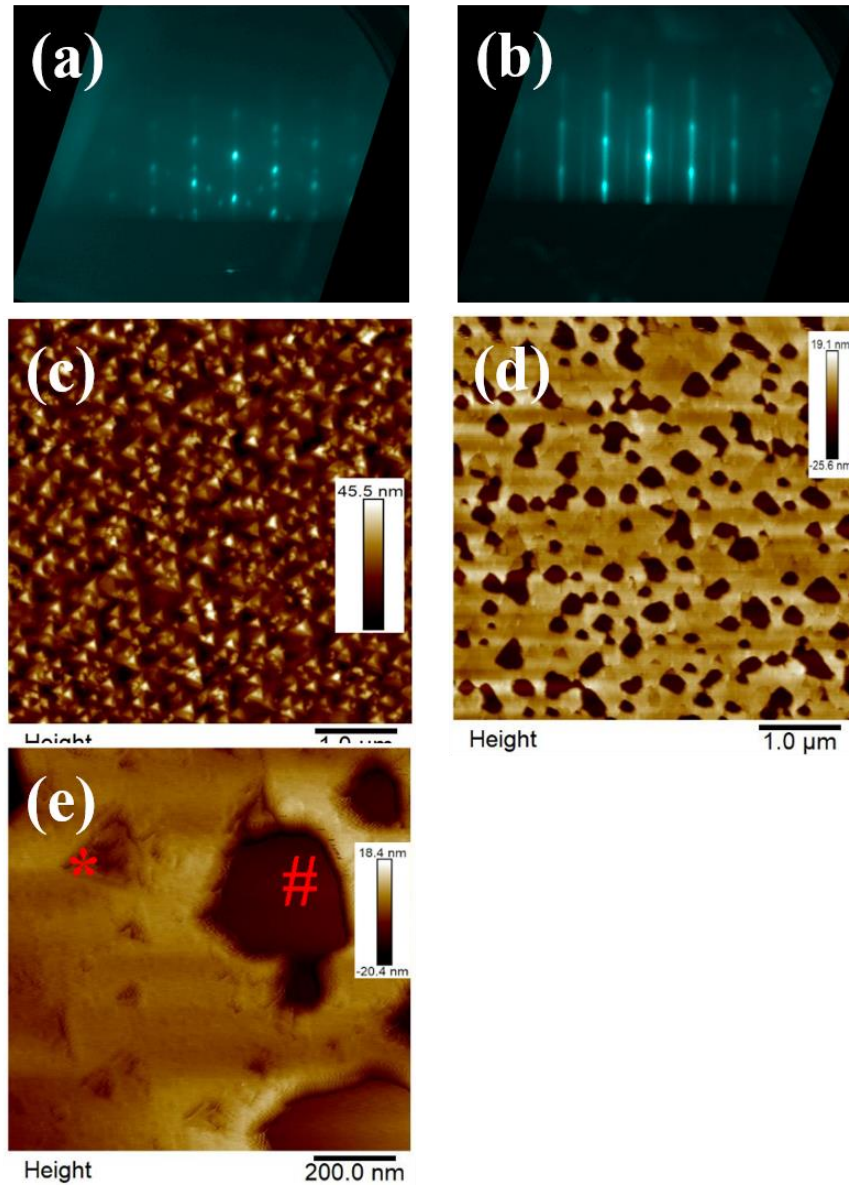


Figure 40: RHEED pattern from sample A1 (a) after the GaAs growth and (b) after in-situ annealing; 5 μm x 5 μm AFM image of (c) 50 nm GaAs (S50), (d) after in-situ annealed sample (S50-annealed) (e) 1 μm x 1 μm AFM images of the in-situ annealed sample. Symbol “*” shows a triangular pit whereas symbol “#” shows an irregular shape pit.

Phi-scan of the in-situ annealed sample (Figure 41) shows that the twin volume is now less than 2%. This is consistent with our explanation that the triangular shape of the stacking fault can be the reason for the formation of triangular pits [23].

Given that the material from SFTs evaporates during annealing and the in-situ annealed sample shows only one phase remaining, optimization of the annealing temperature and time, can result in a twin free GaAs layer. This can be used as an initial template for high-quality GaAs growth for electronic and optoelectronic applications. Further studies will focus on optimizing growth and annealing parameters for obtaining twin-free GaAs template for device quality GaAs growth [23].

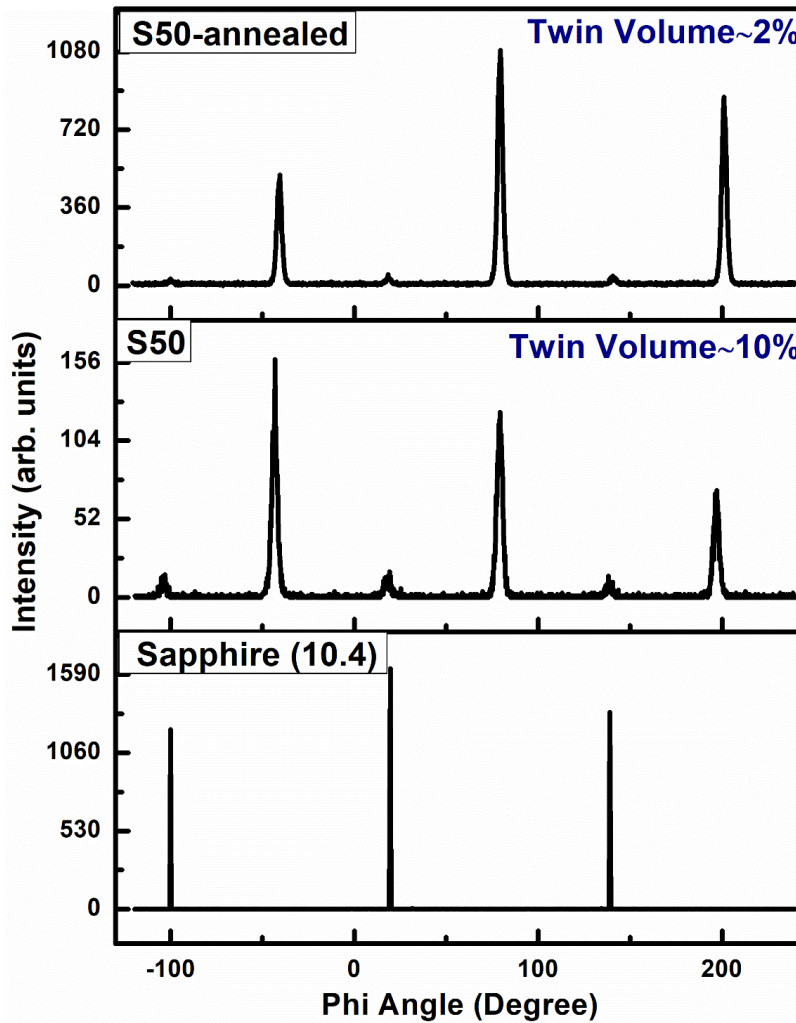


Figure 41: Phi scan of (10.4) plane of Sapphire and (220) plane of 50 nm GaAs sample (S50) and in-situ annealed sample (S50-annealed).

4.2 Two-step growth

We observed that GaAs direct growth on c plane sapphire follows 3D growth mode with 50% twin formation, poor wetting of the surface, and the weak interaction between film and substrate. The presence of AIAs thin nucleation layer improves the wetting of the surface and reduces twinning. Clean atomically flat sapphire substrate enhances the heterointerface interaction between film and substrate. Likewise, twinning and GaAs surface morphology are very sensitive to the growth temperature and in-situ annealing. Until now, the knowledge of the GaAs/sapphire growth system gives us enough confidence that further optimization of growth parameters and annealing parameters (annealing time and temperature) can result in high-quality twin-free GaAs film. Also, for the growth of high-quality film in a high lattice mismatch system, the different growth strategies are familiar such as-(1) two-step growth [137]–[140], multiple annealing, and strained-layer superlattices (SLS) [140], [141]. These strategies improve the crystal quality by suppressing defects in the epitaxial layer. In the following section, the discussion will be focused on the importance of two-step growth and growth parameters for the growth of GaAs on c plane sapphire. A low temperature (LT) GaAs layer is used as a first step in two-step growth mode, followed by a higher temperature (HT) growth layer of GaAs. The mechanism of the two-step growth mode to reduce the dislocation density is discussed by different models in the literature. The most familiar model is the bending of dislocation at the interface of LT GaAs and HT GaAs due to the sudden transition in stress. It is known from the literature that low-temperature GaAs has a lattice constant larger than the lattice constant of high temperature GaAs [26], [142]. The excess As₂ adsorption at low temperature is the main reason for the lattice parameter difference. As a result, the interface between the low-temperature GaAs and the high-temperature GaAs generates misfit dislocation, suppresses the threading dislocations by bending. The dislocation blocking model states that island

coalescence blocks the dislocation in the low-temperature buffer layer, as shown in Figure 42 (a), (b), and (c) [39]. Figure 42 (a) shows a high-magnification cross-sectional TEM image of $\text{In}_{0.78}\text{Ga}_{0.22}\text{As}/\text{LT-InGaAs}/\text{GaAs}$ interface region. This image is used to interpret the mechanism for the dislocation density reduction by the LT-buffer. A brief model of dislocation bending is shown in Figure 42 (c) where a large island buries the small island, and the dislocation line bends at the interface back and forth. Therefore, many dislocations of small islands will be blocked down [143]. For example, Figure 42 (b) shows that the red dislocation line bending towards the right and blocks the right neighboring small island. After that, when the former island meets with a larger island that has a faster lateral growth rate the dislocation line bends towards small island. The large island buries the small island and as well as the dislocations are located in small islands [143].

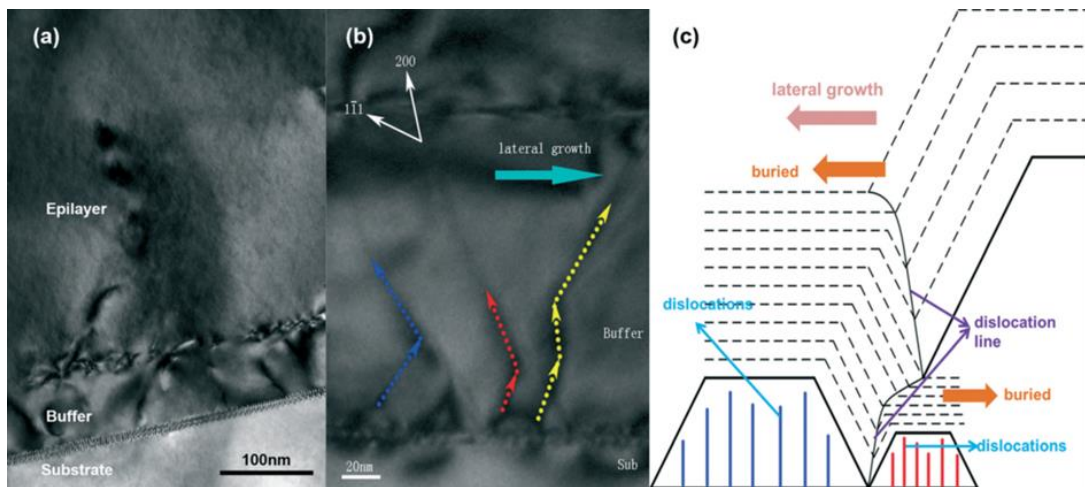


Figure 42: (a) High-resolution cross-sectional TEM image of the $\text{In}_{0.78}\text{Ga}_{0.22}\text{As}/\text{LT-InGaAs}/\text{GaAs}$ interface regions, (b) dislocation bending is shown by green, red and yellow lines, (c) a brief schematic model of dislocation bending [143].

The generation of dislocation model states that the dislocation starts before or after island coalescence as shown in Figure 43 (a-g) [144]. At high-temperatures, defective islands are formed

even before they coalesce, (Figure 43(b)). Many immobile defects are formed when such islands coalesce (Figure 43 (c)), and difficult to remove such defects by further operations like annealing, the growth of higher-thickness layer, etc. At low-temperatures, many small islands are formed, and defects are introduced during the coalescence of islands, as shown in Figure 43 (d-g). Since at low-temperature case the island density is higher than the high temperature, so the number of defects is higher at low-temperature growth.

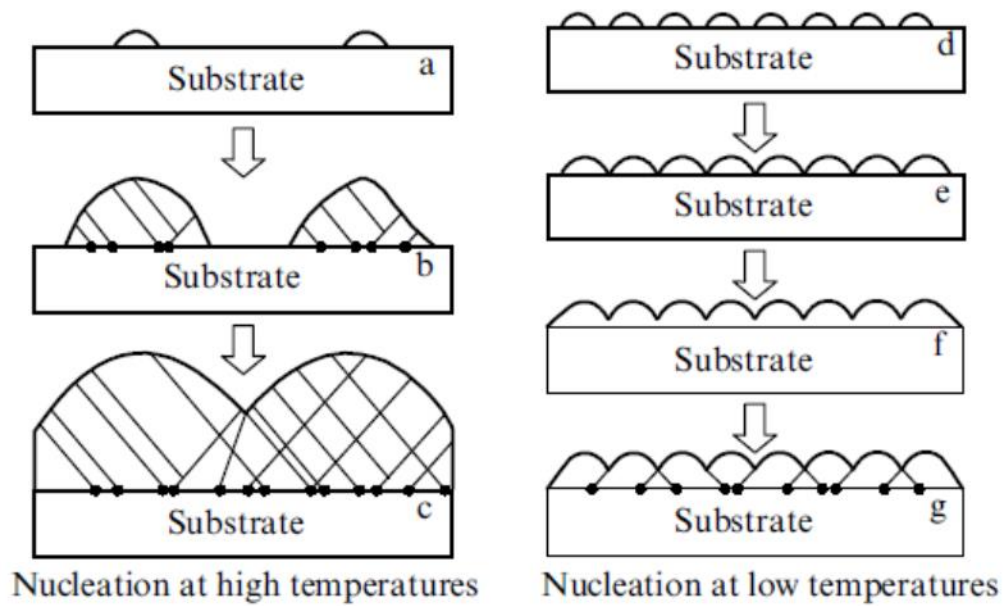


Figure 43: Schematic diagrams of misfit dislocations generation. Left: defects are introduced before the island’s coalescence. Right: defects are introducing after the island’s coalescence [41].

From the above knowledge, we were encouraged to investigate the effects of two-step growth, the thickness of the low-temperature layer, and multiple annealing in our GaAs/sapphire system. More specifically, the schematic diagram of the structure is investigated, with a total growth time of about 1 hour, is shown in Figure 44 (a) [39].

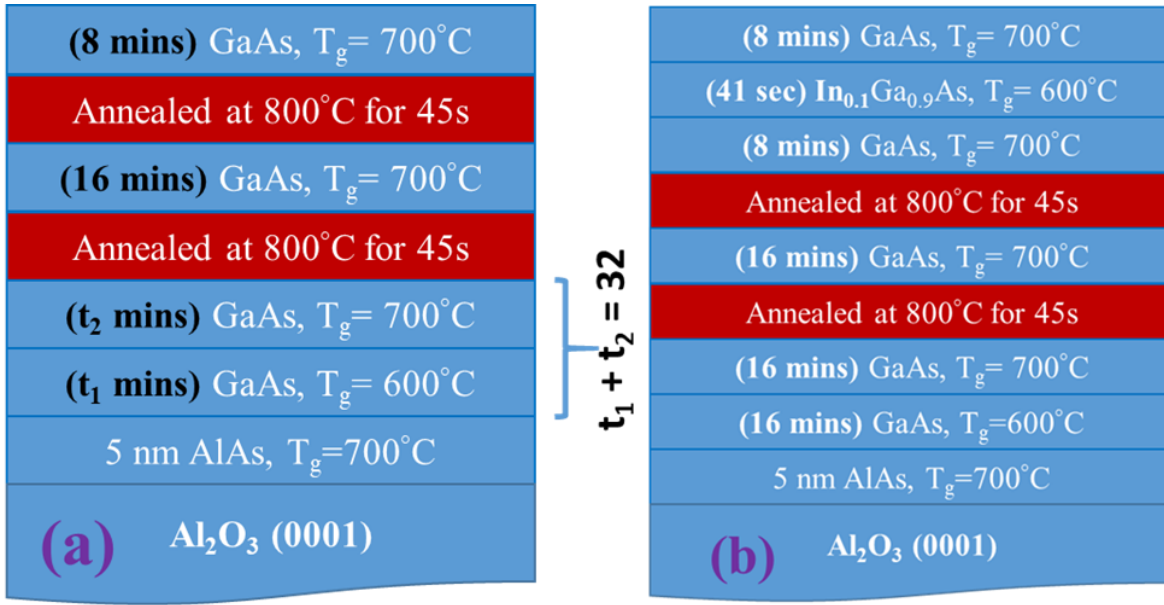


Figure 44: (a) Schematic diagram of sample structure presented in this work; (b) schematic structure of InGaAs QW.

Three different samples with different thicknesses corresponding to the growth time of 16 mins (S1), 8 mins (S2), and 0 mins (S3) are grown to study the effectiveness of the added growth of an LT GaAs layer. The low-temperature GaAs layer growth temperature is 600°C , and the subsequent GaAs layer growth temperature is 700°C .

4.2.1 Surface characterization

The surface morphology of these samples is shown in Figure 45 (a-c). Pyramidal hillocks are present on the surface of all samples. For the sample without an LT layer (S3), random-shaped large and deep pits are also observed. The penetration depth of these pits is up to 60 nm of GaAs film. The RHEED images shown are taken at the end of the growth of these samples (Figure 45 (d) and (e)). A streaky RHEED pattern with clear spots on the streaks, is observed for the sample without LT layer GaAs growth or $t_1 = 0$ (S3) sample. The (2×2) streaky RHEED patterns after the growth for samples with LT layer (S1 and S3) indicate a smooth surface compared to the rougher

surface for S3. The root mean square surface roughness of samples S1, S2 and S3 is observed from the $5\ \mu\text{m}\times 5\ \mu\text{m}$ AFM images are 1.76 nm, 1.55 nm, and 9.46 nm, respectively. Therefore, the LT GaAs layer's presence improves the surface morphology which is confirmed from both AFM and RHEED images. Even though, the RMS roughness value of S1 is higher than S2, the pyramidal hillock density is the smallest in S1.

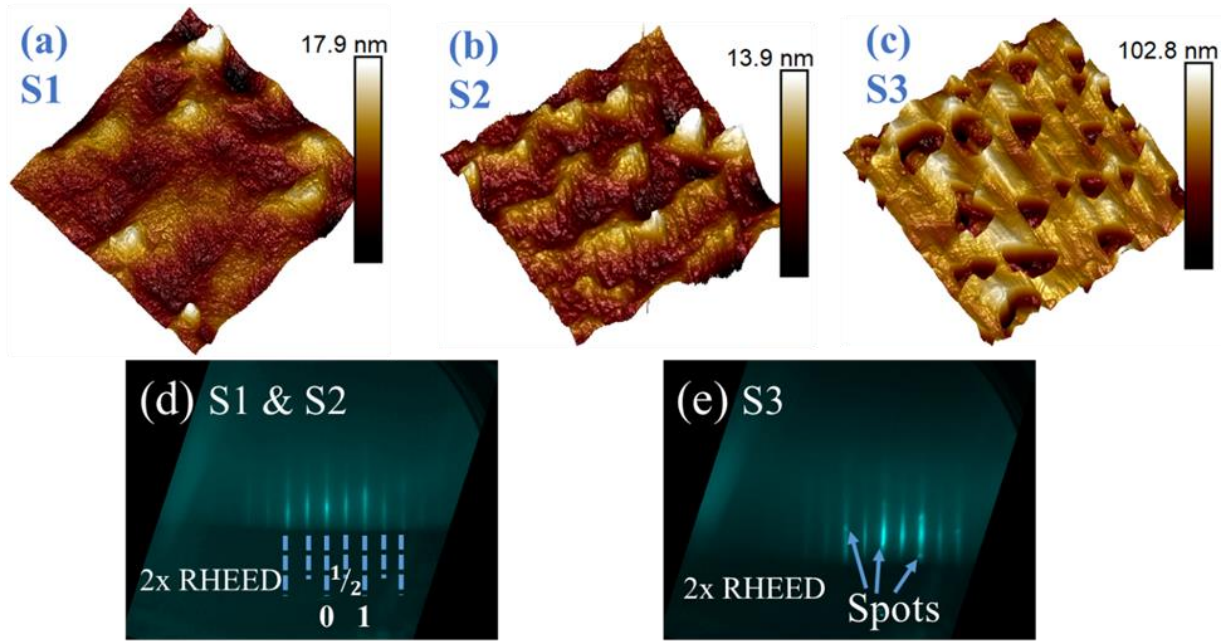


Figure 45: AFM images ($5\ \mu\text{m} \times 5\ \mu\text{m}$) of (a) S1, (b) S2, (c) S3; RHEED images along $[1\bar{1}0]$ direction of GaAs (d) after growth of entire structure of S1 and S2, 0^{th} , $1/2^{\text{th}}$ and 1^{st} order RHEED streaks are marked, longer broken lines show the integer-order RHEED streaks whereas shorter broken lines show fractional-order RHEED streaks; and (e) after growth of S3, spots riding on streaks can be seen, few spots are shown by arrows.

The pyramidal features of GaAs (111)A are related to the Ehrlich-Schwoebel (ES) barrier or by adatom motion in the presence of stacking faults [132], [136], [145]. According to the ES barrier, when an adatom diffuses from step to edge, it experiences a high energy barrier due to fewer neighbor atoms [146]. At low temperatures, adatoms reflect from the high-energy barrier and grow

like 3D growth mode. On the other hand, high temperature helps to overcome the high-energy barrier and grows like 2D mode as shown in Figure 46.

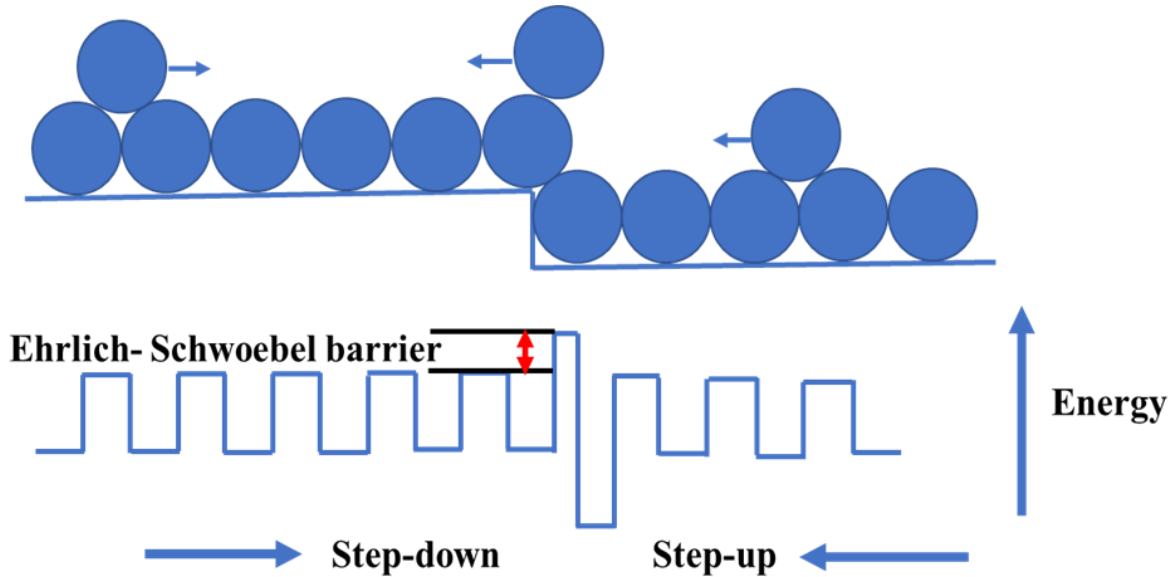


Figure 46: Ehrlich-Schwoebel barrier shows the high-energy barrier at the step.

Surface pits are unusual for the homoepitaxial GaAs (111)A growth. It likely has a different origin than hillock formation. It has been reported that on GaAs (111), surface etch pits are formed due to thermal or chemical etching [147], [148]. It is well known that these etch pits are related to defects in the crystalline film [148]–[150]. For the sample with no LT GaAs (S3), the pits on the surface indicate high defect density in the film during growth and pits' formation by etching during the growth and/or annealing processes. For example, during growth, Ga droplets can be formed due to the low sticking coefficient of arsenic on a GaAs (111)A surface which can etch on the epitaxial film [39]. The thickness of the samples is calculated from the XRD and ellipsometry. The lower sticking coefficient of As on GaAs (111)A surface compared to GaAs (100) surface is responsible for the lower actual thickness than the nominal thickness [125]. The low As

incorporation to GaAs (111)A crystal plane can be explained in terms of dangling bonds. Figure 47 shows the side view of GaAs (111)A, where the surface Ga makes three bonds to the bulk GaAs in the GaAs (111)A and two bonds to the bulk GaAs (100). Therefore, each Ga atom on the surface has only one dangling bond in GaAs (111)A and two dangling bonds in GaAs (100) [120]. The smaller number of dangling bonds of Ga atoms on GaAs (111)A surface is responsible for the low sticking coefficient of As. For each sample, the thickness is obtained around 70 nm, far less than the nominal thickness we expected. Thickness values for samples S1, S2 and S3 are listed in Table 3.

Table 3: Thickness of III-As film on sapphire.

Measurement method	S1	S2	S3
XRD	71 nm	72 nm	NA
Ellipsometry	61 nm	69 nm	62 nm

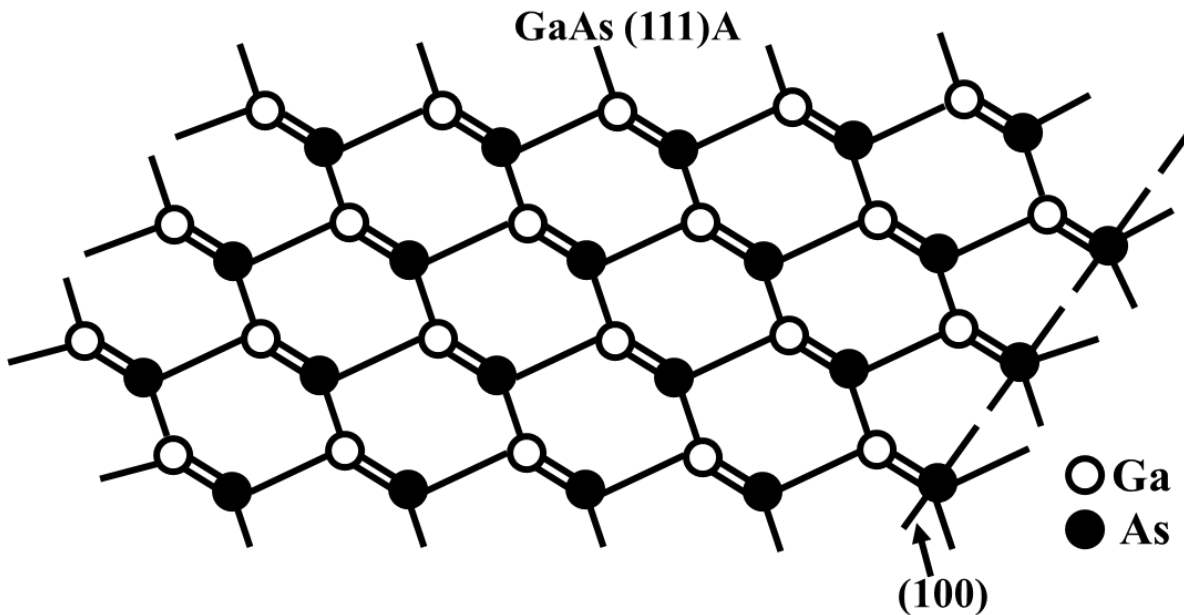


Figure 47: Side view of GaAs (111)A surface. In the (111)A plane each surface Ga atom bonded to the bulk crystal with three bonds and As atom bonded with only one bond to the bulk GaAs. For the (100), Ga and As are bonded to the bulk GaAs with two bonds.

The pits' depth in the S3 sample is almost the same of GaAs thickness. The observed pits in the AFM image of S3 may have penetrated down to the thin AlAs nucleation layer. This could happen either due to the weakly bonded atoms near defected regions, which evaporates during annealing and/or a lower growth rate on top of the defected region.

4.2.2 Structural characterization

Only (111) crystal orientation was observed from out-of-plane measurements of all three samples, as shown in Figure 48 (a, b). If we closely look at Figure 48 (a), thickness fringes are observed for samples with the LT GaAs layer (S1 and S2). Fringes arise due to the interference of the diffracted beam from smooth surfaces. The absence of fringes for sample S3 indicates the rougher surface morphology with nonuniform thickness. If we compare the fringes nature of sample S1 and S2, then prominent fringes are observed for sample S1 than the sample S2, although the RMS roughness of S1 is higher than S2. This could be due to the low density of pyramidal hillocks or, in other words, S1 has a larger surface area of high smoothness. Importantly, the thickness was calculated from the fringes of both samples and listed in Table 3.

Samples show the peak shift from the bulk GaAs peak position, as observed in Figure 48 (b). Such peak shift can happen either due to strain or crystallographic tilt in an epitaxial film [105], [151]. Hence, it is difficult to conclusively state that the strain in GaAs film from these ω -2 Θ scans. Raman spectroscopy is used to measure the strain in thin films. Figure 48 (c) shows the longitudinal optical (LO) peak and transverse optical (TO) peaks of Raman spectroscopy of samples S1, S2, and S3 along with GaAs (111)A substrate. The LO peak position of S1 sample and GaAs (111)A substrate, is almost the same. For S2 and S3, the LO peaks are shifted towards the left. The highest peak shift and the lowest phonon frequency for the GaAs LO peak is observed

for sample S3. These results suggest that S1 has the least strain, whereas S3 is the most tensile strained among all three samples.

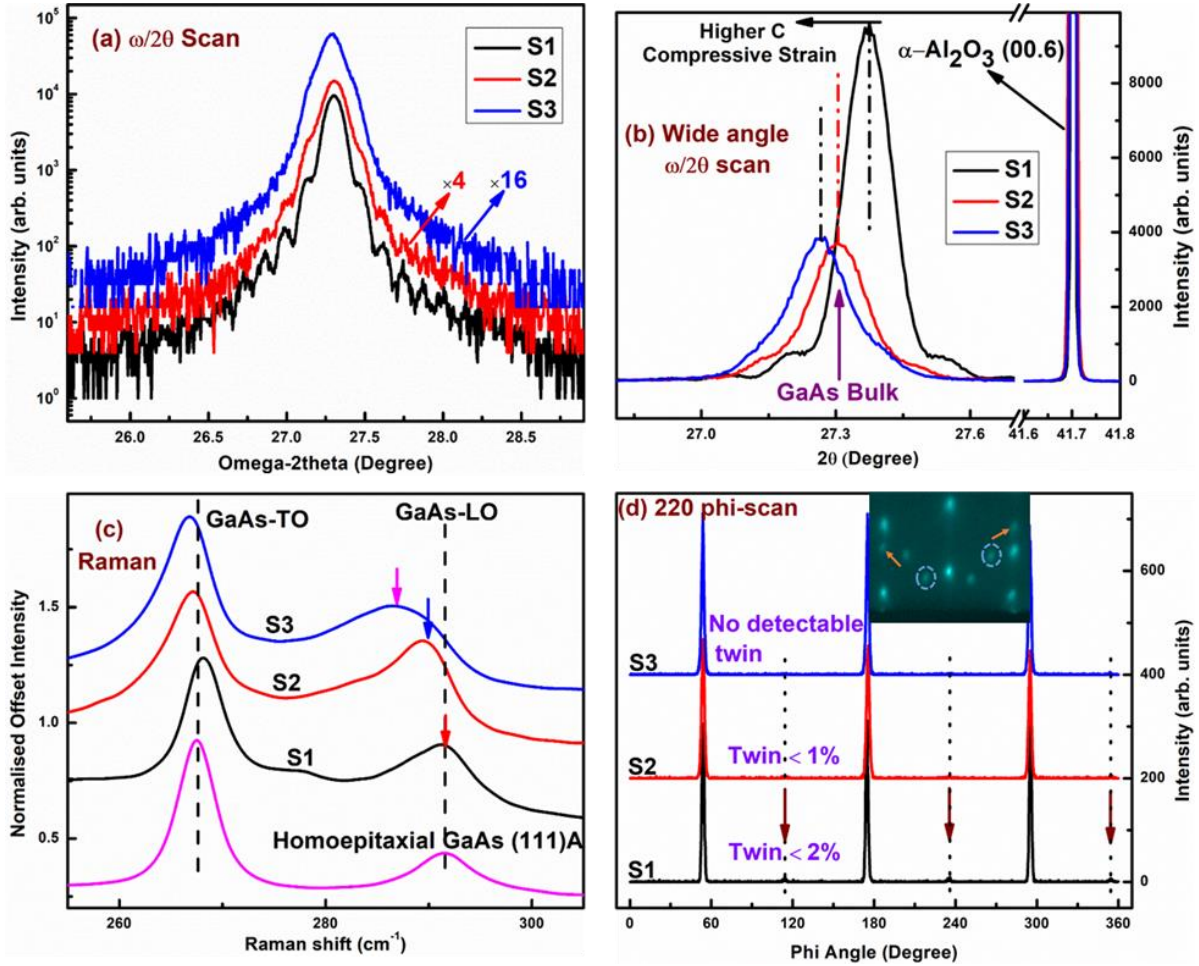


Figure 48: (a) Omega/2theta scan of samples grown with three different LT layer thickness', GaAs peak is centered at same 2θ angle to show the shape variation and fringes of GaAs (111) plane diffraction peak in three samples; (b) (111) symmetric Omega/2theta scan showing the shift of GaAs (111) peak with respect to sapphire (0006) peak; (c) Raman spectra of these samples with homoepitaxial GaAs (111)A sample, arrows pointing the GaAs longitudinal optical (LO) phonon peaks of these three samples show the gradual shift of LO peak from homoepitaxial GaAs, TO stands for transverse optical phonon peak; and (d) phi-scan of (220) plane for these three samples showing the twinning in GaAs film, dotted line show the peak position for 60° twins, Arrows show the peak positions of (10.4) planes of sapphire, the Inset shows the representative RHEED along [1 $\bar{1}$ 0] direction after LT GaAs growth in S1 and S2, some spots corresponding to rotational twins have been shown by arrows while spots corresponding to reflection twins have been shown by dashed circles.

Phi-scans of sapphire (10.4) plane and GaAs (220) plane have been done as shown in Figure 48 (d). Three arrow signs correspond to three sapphires (10.4) crystal planes, which are separated 120° degrees from each other. This indicates trigonal space symmetry of sapphire substrate. In-plane epitaxial relationship between the sapphire substrate and GaAs is confirmed from the phi scan (and also from RHEED), and it is found to be $[11\bar{2}0]_{\text{sapphire}} \parallel [1\bar{1}0]_{\text{GaAs}}$. From the phi scans, almost no twinning is observed for all three samples. A slight hump is observed in the phi scan of sample S1 which indicates the presence of twinning. This can be explained as due to the low growth temperature, during LT GaAs growth, a large amount of twins are generated which can be seen in the RHEED image (shown in the inset of Figure 48 (d)). The RHEED image shows a rough surface and the presence of twinning. However, the higher intensity of emitted photons in PL measurements and the small linewidth of the diffracted beam in RC measurements (shown in later sections) indicates that the top GaAs layers are free from twinned materials. This also confirms the effectiveness of the annealing steps to suppress twins [39].

The HRTEM was used to investigate the interface between the GaAs film and sapphire substrate. Figure 49 (a) shows the HRTEM image of sample S1 near the interface. The high-quality sapphire substrate is confirmed from the sharp film/substrate interface. As expected, the highly defective interface of film/substrate is observed. Broken lines in the image indicate the stacking fault. It is important to closely observe that most of the defects are confined at the film/substrate interface, and such defects do not propagate to the top GaAs layer. As a result, high-quality GaAs is obtained after only 70 nm of GaAs growth. This proves the high effectiveness of the LT GaAs layer to confine defects within itself. Figure 49 (c) shows the effect of defect propagation on the films' surface to cause a pit at the surface.

The RC measurements of these three samples are shown in Figure 49 (b). It is a great way to assess the quality of the crystal materials. More specifically, the lower FWHM of the rocking curve indicates the less deviation of the crystal planes from the growth direction. Each RC curve shows a sharp peak with broadening at the base, suggesting that the curve is the sum of two effects. Two Gaussian curves are fitted with each RC curve: one with a lower linewidth and the other with a higher linewidth. The Gaussian fittings results of each sample are listed in Table 4. The highest ratio of integrated intensity between the broader and sharper peak is observed for the sample with no LT layer (S3), while the lowest ratio is observed for sample S1. The most likely reason for this RC base broadening is the presence of point defects in GaAs. The point defects in the epitaxial layers often contribute to the broadening of the peak [152]. A second possible explanation is two different regions of different GaAs quality that making-up the film constructs these two curves. We have observed from the HRTEM image that the material near the film-substrate interface has poorer quality than the region away from the interface. In S3, the higher integrated area of the broader peak with respect to the sharper peak indicates that this sample has either a higher volume of low-quality GaAs or simply has more point defects. Both sharper and broader peaks of the S1 sample indicate that the LT layer improves the crystallinity of GaAs. Judging from HRTEM, GaAs' higher quality in S1 might be related to efficient bending of dislocations along the LT GaAs/GaAs interface to form misfit dislocations (MDs). This is reasonable since there is higher stress accumulation at the interface due to the higher thickness of the LT layer in S1 [39].

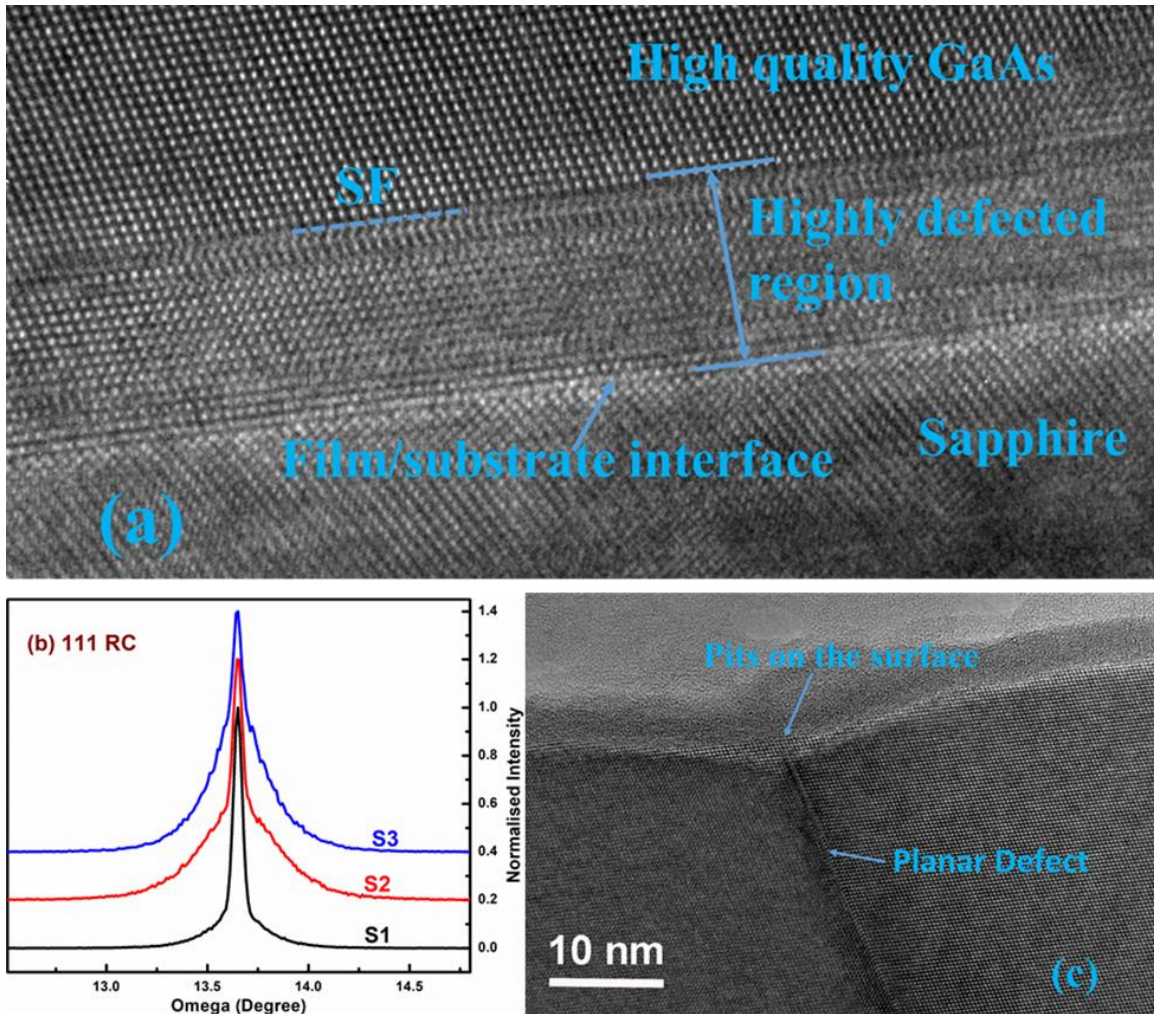


Figure 49: (a) Cross-sectional HRTEM image of S1 near film/substrate interface, SF is the abbreviation for stacking fault; (b) RC of all three samples (c) HRTEM image showing the formation of a pit on the surface due to extended defect.

Table 4: Linewidth and integrated intensity ratio of broader and sharper curves from Gaussian fitting of RC for samples S1, S2, and S3

Sample ID	Linewidth of sharper peak (arcsec)	Linewidth of broader peak (arcsec)	Integrated intensity ratio of broader to sharper peak
S1	187.2	1195	1
S2	187.2	1710	5.2
S3	212.4	1364	6.6

4.2.3 Photoluminescence (PL)

The PL measurements of three samples are also performed to investigate the crystal quality as shown in Figure 50 (a). The highest PL peak intensity among three samples is observed for sample S1. This indicates the highest quality GaAs material for S1 sample which is consistent with the result of AFM and XRD. From the images for all three samples the PL peak does not occur at the same energy. This may occur due to the background noise, especially in the case of S3.

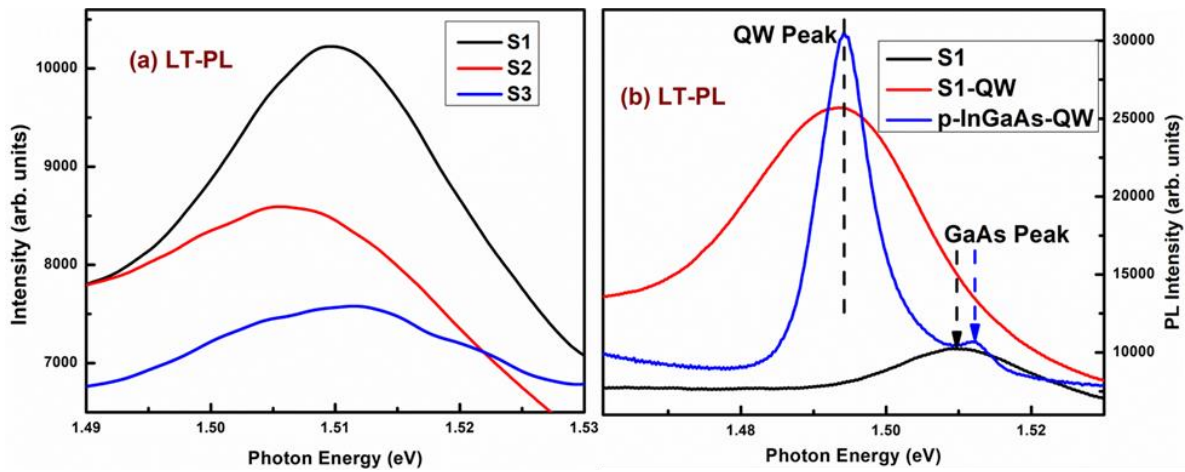


Figure 50: (a) PL spectra of samples having three different thicknesses of LT layer and (b) PL of GaAs buffer (S1), InGaAs QW on sapphire (S1-QW), and InGaAs QW on GaAs substrate (p-InGaAs-QW). S1 PL repeated to show the shift of QW peak from GaAs, dashed arrow shows the GaAs PL peak position from homoepitaxial GaAs and GaAs on sapphire samples.

In summary, the S1 sample has the narrower PL, RC linewidths and a higher PL intensity, indicating that near the top GaAs layer of the S1 sample has less defect density, and it would be the best candidate to grow active device layers on it. With this in mind, on top of the S1 sample, we grew a 10 nm wide $\text{In}_{0.1}\text{Ga}_{0.9}\text{As}/\text{GaAs}$ QW (S1-QW). The composition and thickness values of the QW are nominal. To compare it with the homoepitaxial system, we also grew the same QW on a GaAs (111)A substrate (p-InGaAs-QW). The comparison of PL spectra of homoepitaxial QW and the QW on the S1 sample is shown in Figure 50 (b). Theoretical PL peak position for electron

energy level to heavy-hole energy level is near 1.37 eV. However, in this case, the observed PL peak position of QW occurs at 1.49 eV. We have already seen the small actual thickness of the GaAs compared to the nominal thickness, likely due to the different sticking co-efficient. In Table 5, we have listed the PL linewidth, peak position, and integrated intensity of both samples. The InGaAs QW's PL intensity on sapphire is of the same order as observed for the QW on the GaAs substrate. However, the QW peak broadening in the case of GaAs on sapphire is higher. This can be due to the surface roughness and/or higher defect density resulting from the substrate and film material properties mismatch. Both can be improved and is the focus of our future work. While more research is required, we have presented the potential to realize an integrated microwave photonic chip on a sapphire platform.

Table 5: Integrated intensity, linewidth, and peak position of QW PL peak from both QW samples.

Sample ID	Integrated intensity (arb. units)	Linewidth (meV)	Peak position (meV)
S1-QW	550	32.53	1491.2
p-InGaAs-QW	192	9.12	1494.4

4.3 Thickness Optimization

4.3.1 Growth temperature variation

From the previous section, we have observed that grown GaAs' actual thickness on the c-plane sapphire substrate is less than the nominal thickness. The low As_2 incorporation on the GaAs (111)A crystal plane, higher growth temperature, and annealing temperature can be the reasons of thickness reduction reasons. The thickness improvement is essential for the GaAs/sapphire system due to the higher thickness improves the crystal quality and the light emission property of material. To improve the thickness, we have reduced the growth temperature from $X=700^\circ C$ (S1) to $X=650^\circ C$ (S2). Schematic diagram of the samples is shown Figure 51.

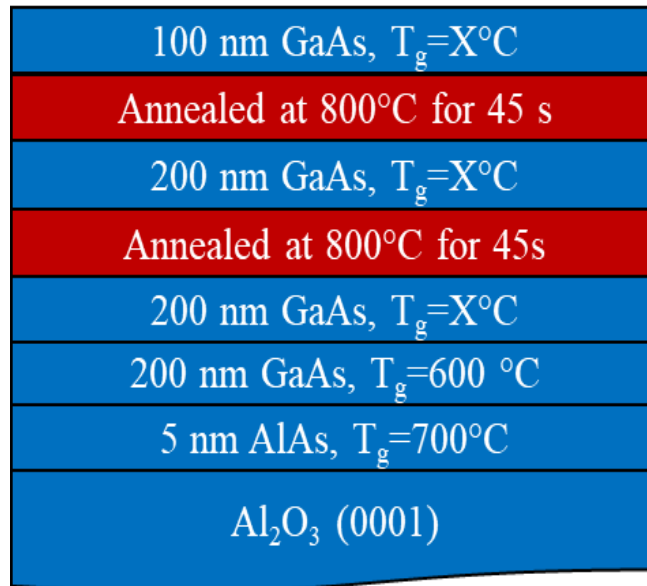


Figure 51: Schematic diagram of the sample structure.

The AFM ($5\ \mu m \times 5\ \mu m$) and RHEED images are shown in Figure 52. Streaky RHEED pattern is observed for sample S1, indicating the smooth surface. Streaky plus spotty pattern is observed for sample S2, indicating the rough surface. The (2×2) surface reconstruction is observed for both

samples, and it remains invariant irrespective of growth temperatures. The pyramids and the truncated pyramids are observed for samples S1, and S2, respectively. The sample's surface roughness is 1.76 nm (S1) and 47 nm (S2) is determined from the AFM images. The truncated pyramids density is higher in the S2 sample than the pyramids of sample S1.

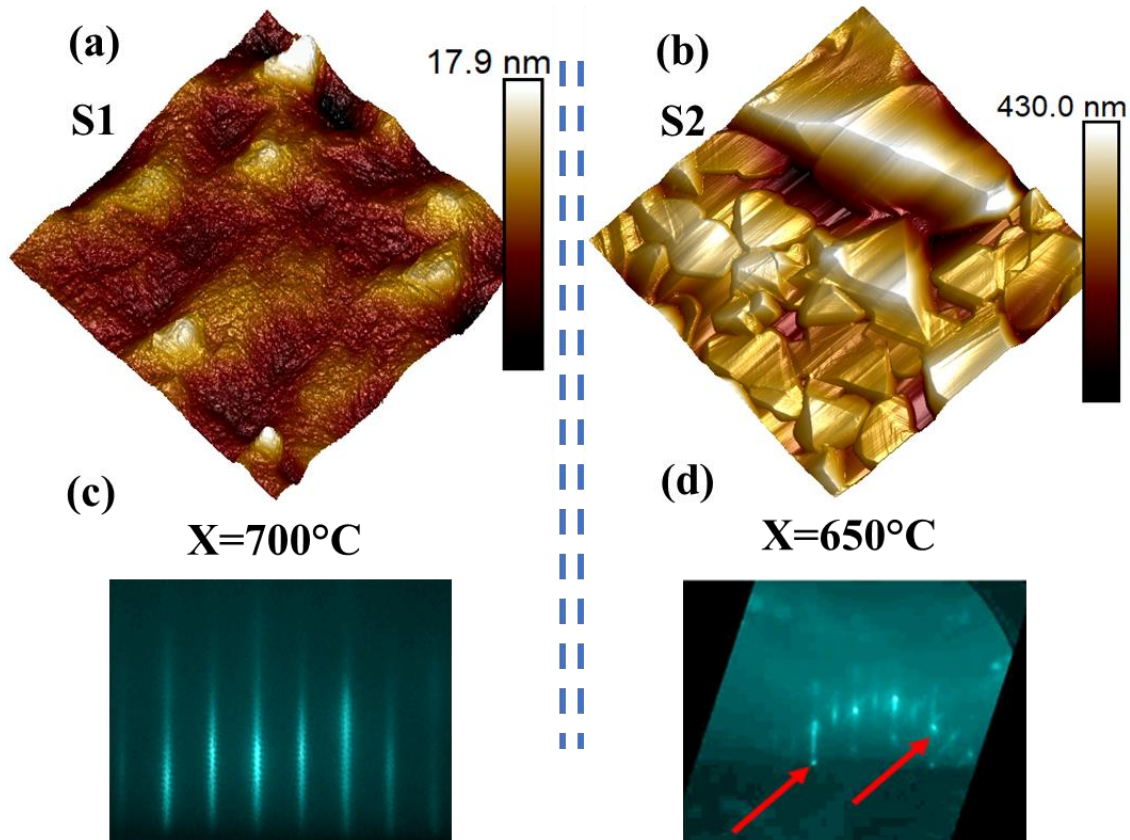


Figure 52: Surface morphologies of the samples grown at (a) 650°C and (c) 700°C. Real time growth image after the growth at (b) 650°C and (d) 700°C. Red arrows show the spots on the streaks.

The stacking fault is responsible for the pyramids and the truncated pyramids. The excess vacancy agglomeration along the $\langle 110 \rangle$ of $\{111\}$ planes generates a Frank sessile dislocation loop [153], [154]. The high energy triangular Frank sessile dislocation may dissociate into stair-rod dislocations along the $\langle 110 \rangle$ edges and Shockley-partial dislocations along the three remaining

{111} planes [155], [156]. The partial dislocations will bow out in their slip planes due to the repulsion by stir-rod dislocations. The stacking faults increase the energy in the different faces. If the energy is low then stacking fault tetrahedron (SFT) is formed, otherwise Frank loop partly dissociate and forms truncated pyramids [132], [156], [157].

Omega/2theta measurements were performed to determine the crystal growth direction of both the samples. Figure 53 (a) shows, only (111) crystal orientation is observed. For the S1 sample, prominent fringes are observed but not for the S2 sample. The S1 sample thickness is 75 nm, measured from the XRD fringes and ellipsometry whereas the S2 sample thickness is 270 nm, measured from the ellipsometry. The lattice mismatch, thermal mismatch and residual contamination introduces interface roughness. If the interface or surface is not smooth, X-ray scattering loses coherency, and fringes disappear. Figure 53 (b) shows the normalized rocking curves of the samples S1 and S2. The sample S2 has higher surface roughness, but a smaller FWHM of the rocking curve than S1. The possible reason for the smaller FWHM can be the higher thickness of the film, which reduces the inhomogeneous strain distribution and an increase of coherence length [158]. The phi scan (Figure 53 (c)) shows the twinning has increased at low-temperature growth, which is similar to our previous study [23]. The low-temperature PL was measured at 10 K, and the FE emission was observed for both samples, as shown in Figure 53 (d). The FE for S1 was shifted 4 meV from the ideal FE position, and the local stress can be responsible for shifting the FE emission peak. For sample S2, the defect state peak arises from the recombination of free or donor bound electron to acceptor recombination [159].

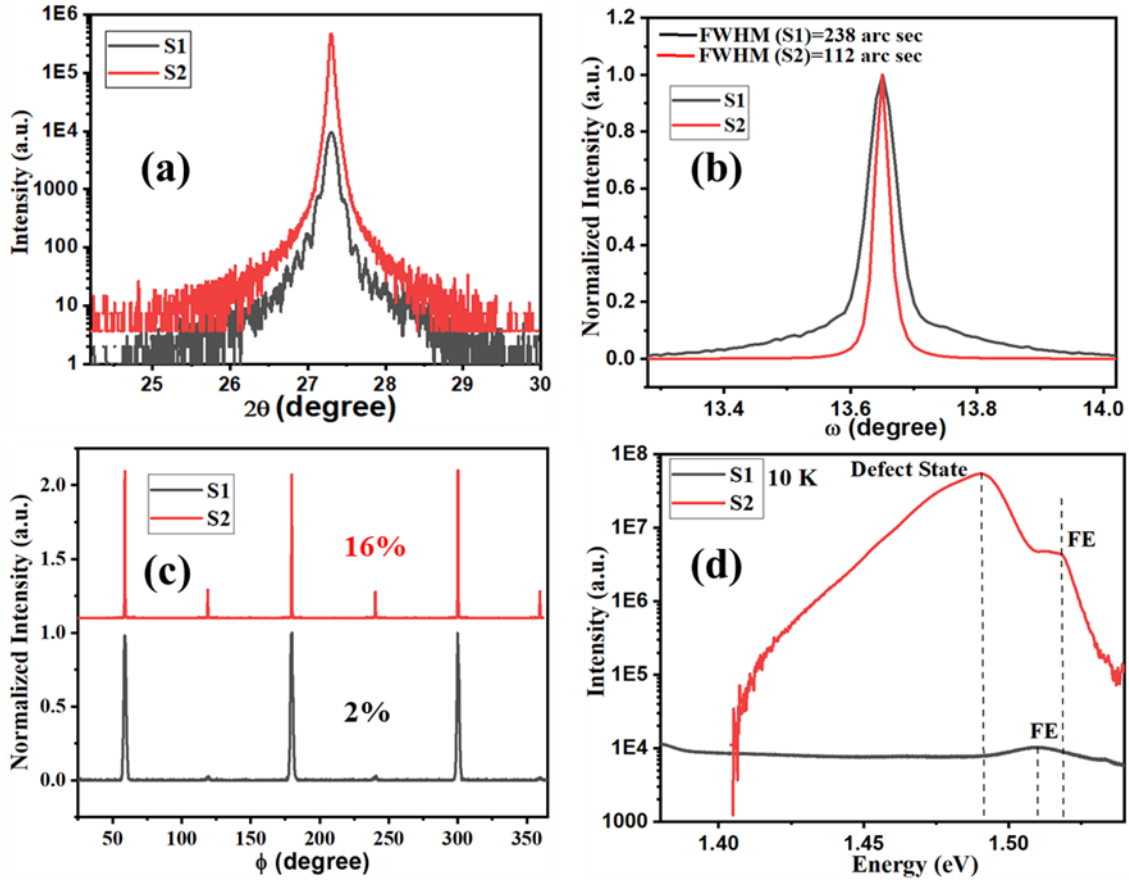


Figure 53. (a) only (111) crystal orientation is observed in out of plane measurements; (b) Sample S2 shows the lowest FWHM; (c) Phi scan shows the twinning on both samples; (d) PL measurements of both samples at 10 K.

Room temperature PL emission was observed for the sample S2, as shown in Figure 54.

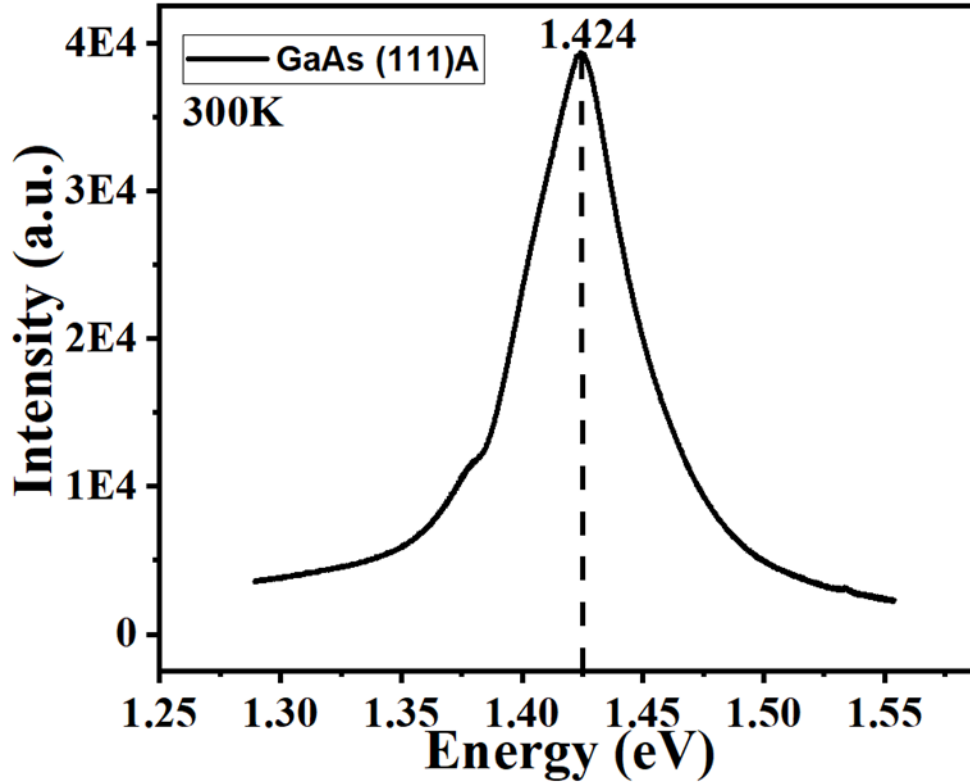


Figure 54: Room temperature PL from sample S2.

4.3.2 Effects of annealing

Three samples A1, A2, and A3 are grown to study the effects of annealing on the crystal quality. The schematic diagrams of the samples are shown in Figure 55. The sample A1 was grown without annealing ($X=0$ s), A2 was annealed two times at 800°C for 45 s with the presence of As_2 as shown in the schematic diagram Figure 55 (a), A3 was annealed by thermal cycle annealing (TCA), and the TCA steps are shown in Figure 55 (b). The TCA temperature range was selected from the promising results of GaAs grown on Si by TCA to construct the InGaAs/AlGaAs quantum-well lasers [160].

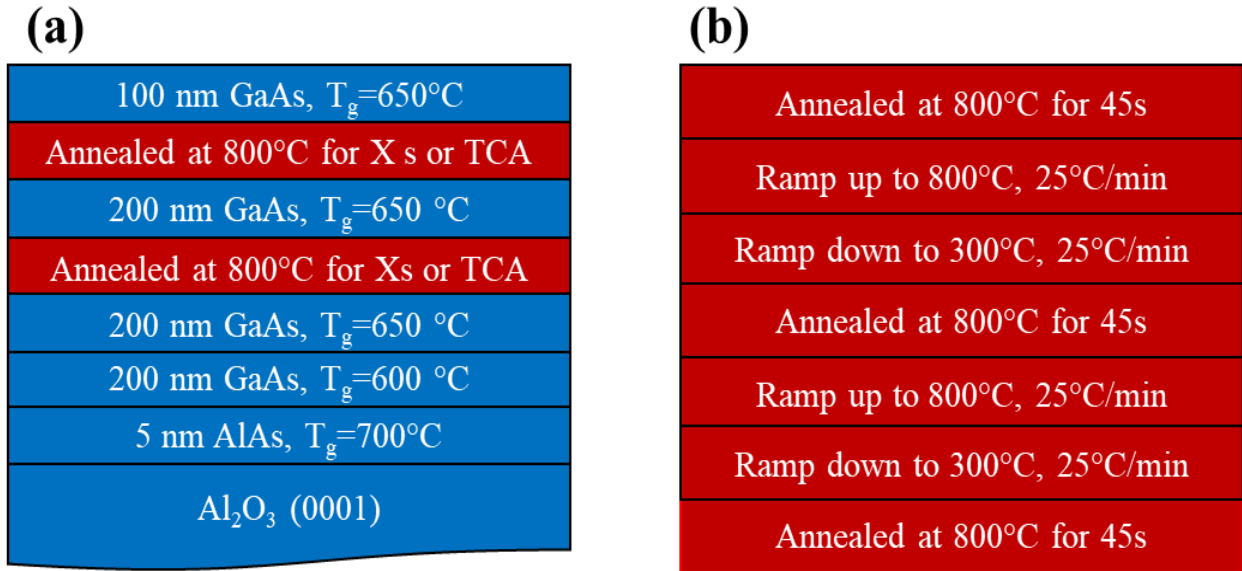


Figure 55: (a) schematic diagrams of the samples A1, A2 and A3; (b) TCA steps.

The surface morphology of the samples A1, A2, and A3 are shown in AFM images (Figure 56). The truncated pyramids are observed for all the samples. For sample A1, highly dense truncated pyramids are observed. The top flat area of the pyramids increased after introducing annealing and TCA. The edges of the pyramids suffer from dislocations, and during annealing, under thermal stress, the top flat area can be increased by the coalescence of the dislocations edges [25], [133]. In sample A3, the materials desorption or etching generates valleys, as shown in Figure 56 (c). The noncongruent evaporation at high temperatures in GaAs (111)A is observed where arsenic evaporates more intensively than gallium atoms [161]. The excess of metal atoms leads to the formation of Ga droplets and etches the materials.

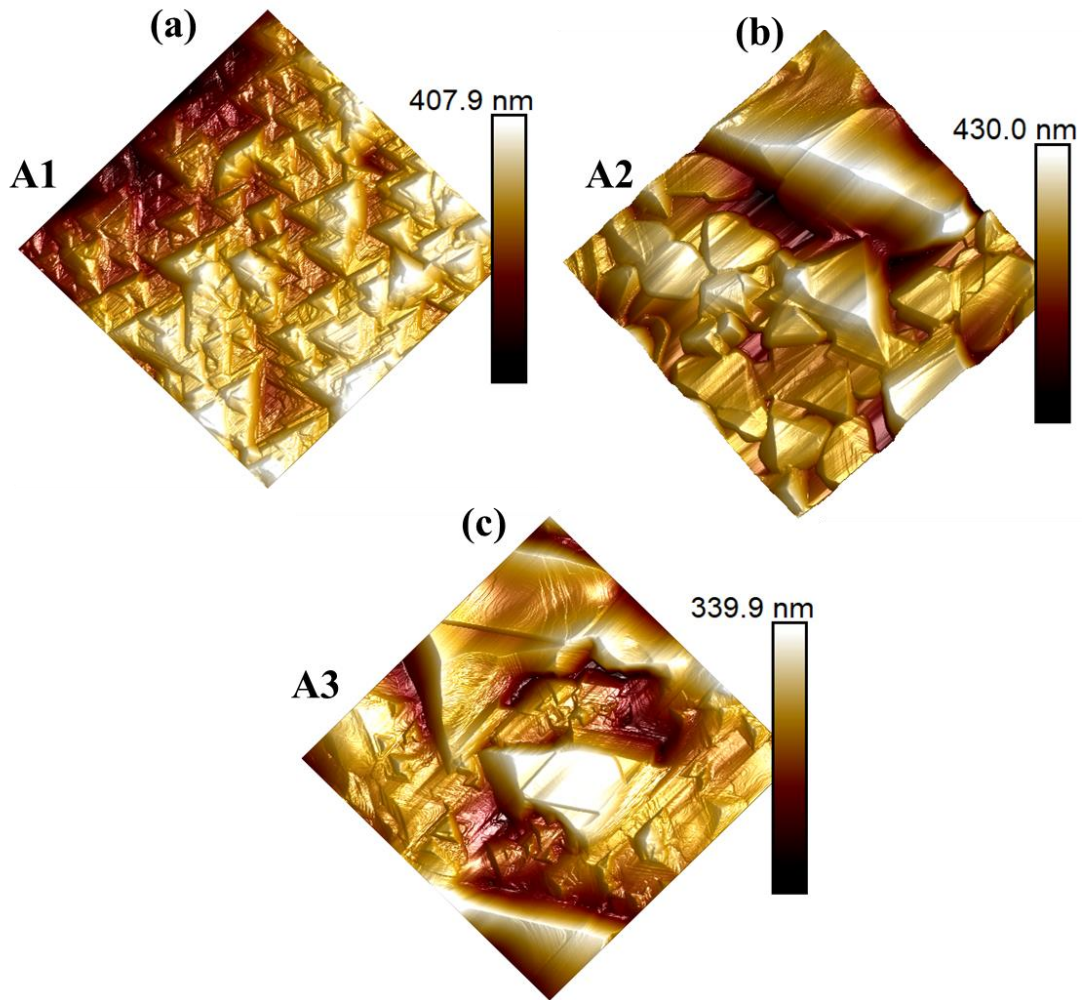


Figure 56: AFM images of samples grown (a) without annealing; (b) two times annealing; (c) TCA.

Only (111) crystal orientation was confirmed from the out-of-plane measurements (Figure 57 (a)).

The FWHM from the rocking curve is listed in Table 6.

Table 6: Surface roughness, thickness, and FWHM of the samples A1, A2 and A3 are listed.

Samples	Surface Roughness (nm)	Thickness (nm)	FWHM
A1	44	496	818
A2	47	270	112
A3	21.6	89	103

The A1 sample without annealing shows the maximum FWHM among three samples as shown in Figure 57 (b). The FWHM of A2 and A3 samples is reduced and almost the same, indicating that high crystallinity with a low orientational spread from the surface normal direction for both the samples. Therefore, annealing is essential to improve the crystal quality of the GaAs/sapphire system. Phi scan shows the twinning is observed for all samples, as shown in Fig. Figure 57 (c).

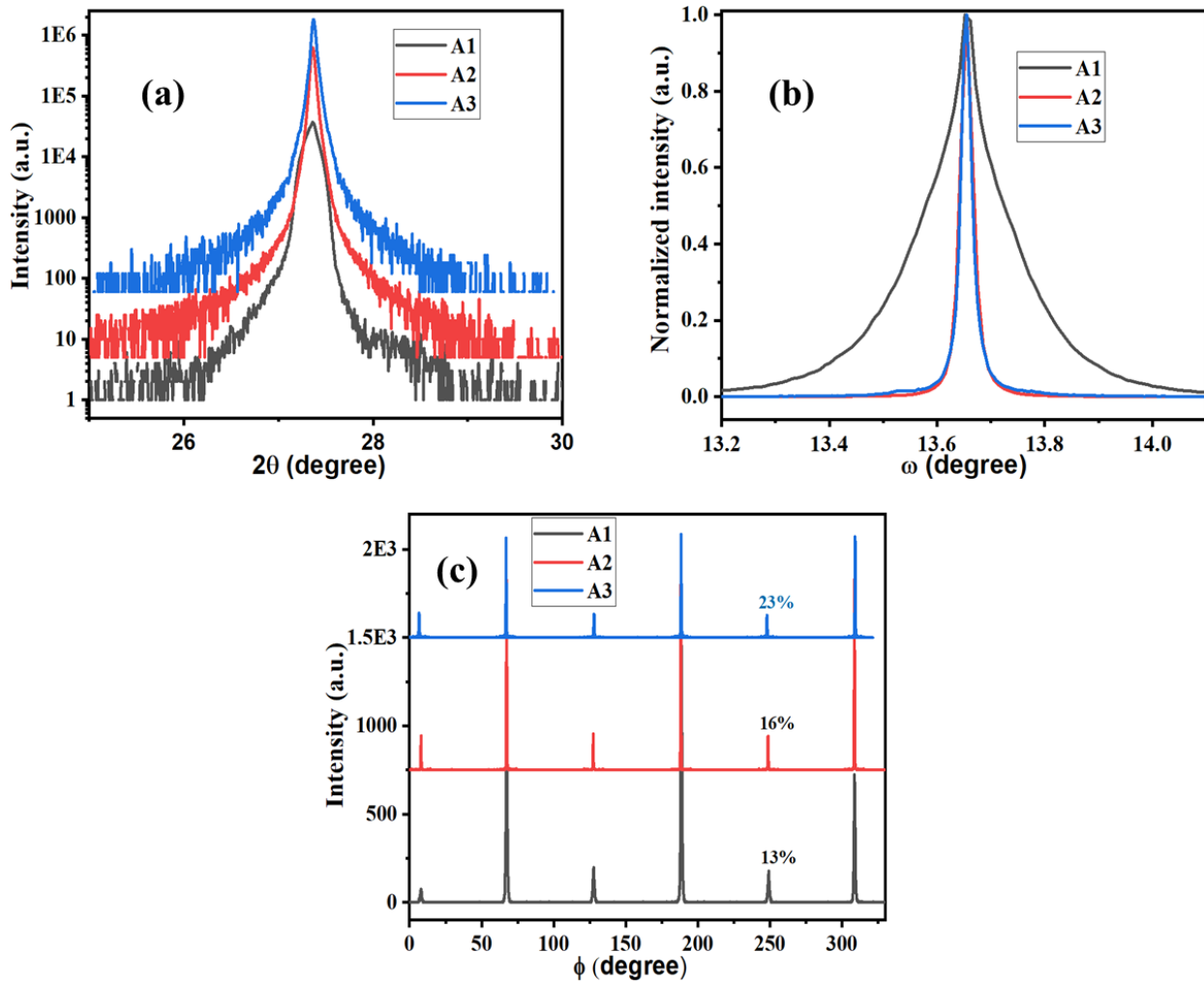


Figure 57: (a) Out of plane orientation confirmed only (111) single crystal orientation; (b) sample A1 shows the highest FWHM from the rocking curve measurements; (c) Twinning is observed from all samples; (d) RT PL emission from A1, A2 and A3 samples.

The PL emission was measured at both LT and RT as shown in Figure 58 (a, b). The FE emission was observed for samples A2 and A3 at LT. In addition to FE emission a defect state is observed due to a replacement of C_{As} or in other words due to free electron to acceptor, and/or donor-bound electron to acceptor recombination [159], [162]. A broad peak around 1.46 eV is observed for sample A1 which may be related to gallium vacancies, arsenic interstitials, or As_{Ga} antisite defects [162]. The RT PL measurements show a broad defect state emission for sample A1, for A2 and A3 is shifted towards high energy Figure 58 (b).

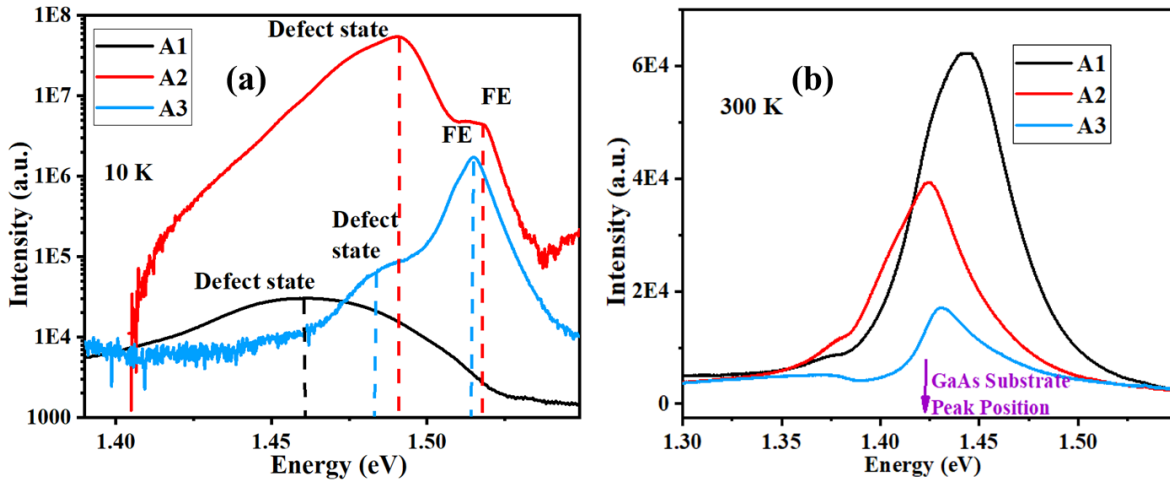


Figure 58: PL measurements of samples A1, A2 and A3 at (a) LT, (b) RT.

4.3.3 Micro disk laser characterization

The high crystal quality and RT PL of GaAs film encouraged us to fabricate a microdisk laser from GaAs/sapphire system. The samples A2 and A3 are both used for the fabrication of the 16 μm microdisk lasers. After the fabrication to characterize, the samples micro-PL set up was used. Until now, the laser structure from sample A3 is characterized, and the results are discussed below.

Two different types of lasers, 532 nm cw, and 700 nm pulsed lasers are used to characterize the microdisk lasers. The lasing was not successful. High surface roughness may be the possible reason for this. The PL emission from the microdisk with different pumping power for both cw, and the pulsed laser at 77 K is shown in Figure 59. The PL intensity increases with increasing pumping power. The possible reason for the bandgap shrinks or redshifted PL signals at 77 K than 10 K measurements for both cw and pulsed laser is local lattice heating. The substrate's low thermal conductivity is also responsible for increasing the system's temperature and hence, bandgap shrinks.

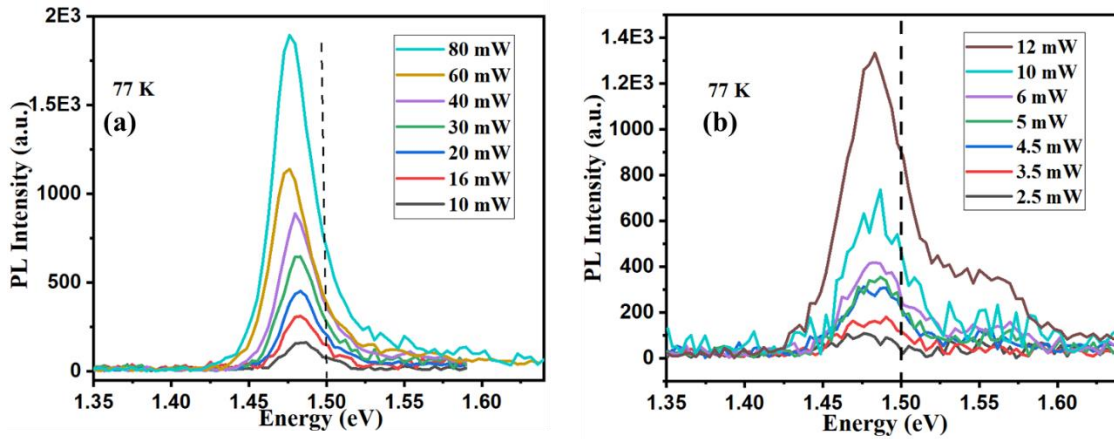


Figure 59: Power dependent PL spectra for two lasers (a) 532 nm cw; (b) 700 nm fs.

The integrated PL intensity for two lasers with incident power is shown in Figure 60. The integrated PL intensity follows the power law, $I_{PL} \propto L^n$, where I_{PL} =integrated PL intensity, L =excitation power, n reflects the various recombination process. For exciton recombination, the PL intensity is proportional to the excitation intensity ($n=1$). For free electron-hole pair recombination, the PL intensity is proportional to the square of excitation intensity ($n=2$). For cw laser, bound exciton states are formed at low and intermediate electron concentrations by the Coulomb interaction whereas for fs laser the recombination is dominant by free electron-hole

because higher densities cause a static screening of the of the electron-hole Coulomb potential. The phase space filling up to the Fermi energy also leads to a strong decrease of the exciton binding energy as free electron concentration increases [163], [164].

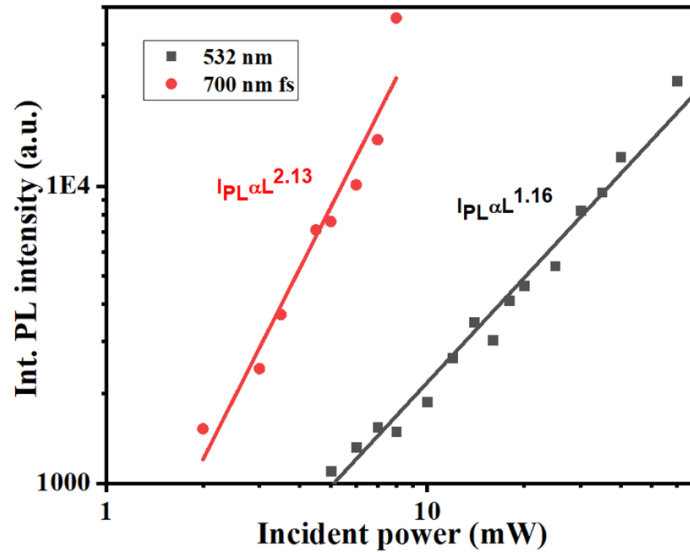


Figure 60: Integrated PL intensity vs incident power for two cw laser and pulsed laser.

Until now, we have been focusing on the growth of the GaAs buffer layer on c-plane sapphire substrates. Now, the knowledge and experience we have achieved from GaAs/c-plane sapphire system will transfer for the growth of GaAs on the r-plane sapphire substrate. The advantage of the r-plane sapphire substrate over the c-plane sapphire substrate is its crystal structure. The rectangular crystal structure of r-plane sapphire makes it feasible to successfully grow silicon on sapphire (SOS), which is part of the silicon-on-insulator (SOI) family of CMOS technologies. Therefore, if we successfully grow GaAs on an r-plane sapphire substrate, then we can take advantage of CMOS technology, where it would be possible to integrate both laser and amplifier with corresponding RF electronics [24]. While there are few reports of heteroepitaxial system of cubic Si(Ge) on both c and r plane sapphire [78], [107], [165], [166] and cubic III-As on c-plane

sapphire [23], [39], [109], [167]–[171], to the best of our knowledge, there are no reports about epitaxial growth of III-As on r plane sapphire as a substrate.

4.4 GaAs growth on R-plane sapphire

As we have already discussed, the growth of GaAs on sapphire substrates is a dissimilar materials system. Consequently, it is not trivial to grow or predict the GaAs film's growth direction on r plane sapphire substrate. For example, the rectangular crystal structure of r plane sapphire substrate may influence the rectangular (110) crystal plane of GaAs for the atomic alignment, while the sapphire substrate's hexagonal crystal nature can force GaAs to grow along [111] direction, or GaAs may take totally different growth direction. In the following section, the discussion will be focused on the growth III-As on r plane ($1\bar{1}02$) sapphire.

For the study of the possible growth directions of GaAs on the r-plane sapphire substrate the atomic arrangements of the r-plane sapphire, the (111) plane, and (110) plane of GaAs are shown in Figure 61. The lattice constants of each crystal plane are also mentioned. The lattice mismatches of (111) and (110) crystal planes of GaAs are calculated with r plane sapphire substrate by considering each different potential alignment. The (111) GaAs crystal plane has compressive (35.2%) and tensile (16.2%) strain in the two perpendicular directions. For the (110) crystal plane, it has compressive strain (10.7%) and tensile strain (16.2%).

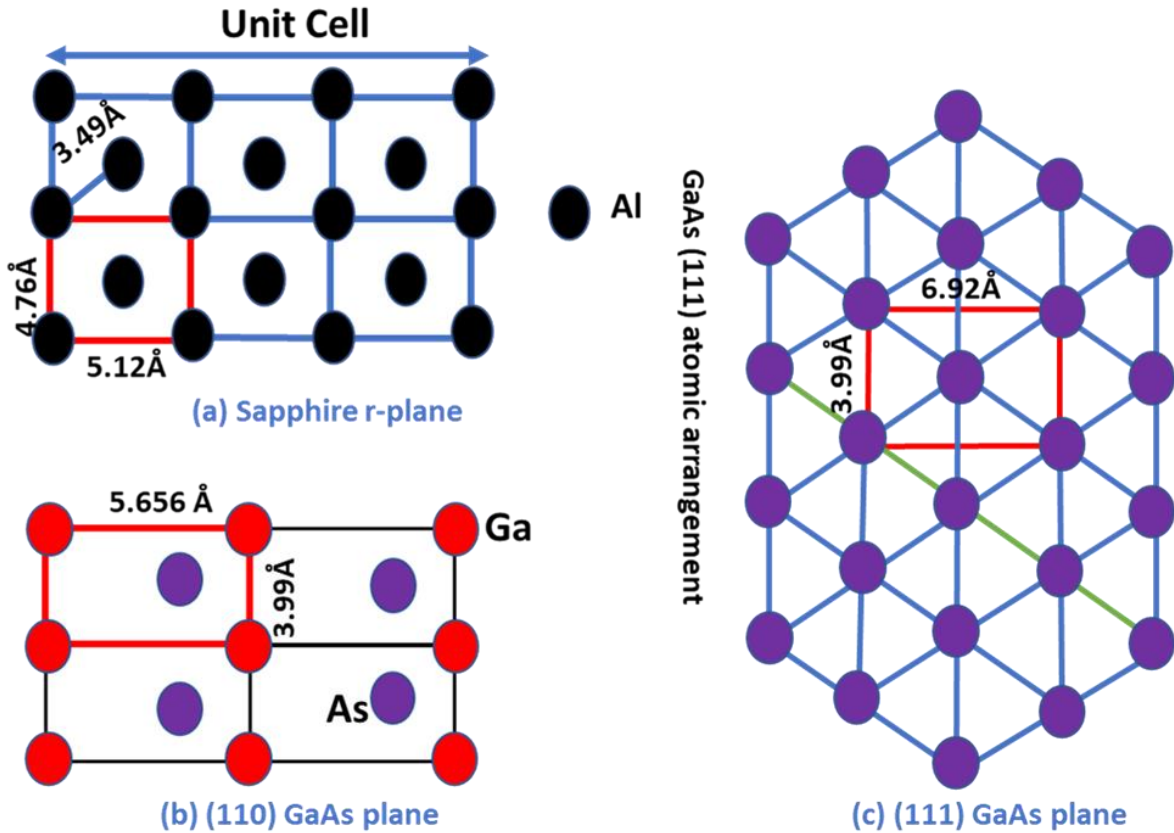


Figure 61: Atomic arrangement of (a) r-plane sapphire, (b) GaAs (110) plane, and (c) GaAs (111) plane.

In addition to the lattice mismatch, the substrate surface energy is also an important role in deciding the orientation and quality of the epitaxial film [172]. We have already discussed, for a 2D epitaxial material growth of GaAs material, and the energy dynamics should maintain the following inequality:

$$\gamma_s \geq \gamma_i + \gamma_e \quad \text{Equation 19}$$

where, γ_s , γ_i , and γ_e are substrate surface energy, interface energy between substrate and film, and film surface energy, respectively. The relaxed c plane and r plane substrates surface energy are 1.85 and 2.26 Jm^{-2} , respectively [173], [174]. Interestingly, a better film and substrate interaction

is observed for GaAs growth on r plane sapphire substrate over c plane sapphire substrate [24]. In the following sections, we will discuss the comparison of GaAs growth on c plane and r plane sapphire substrate, the effect of growth parameters, and AlAs nucleation layer on GaAs film surface morphology on the r plane sapphire substrate.

The substrates were used in this experiment possessed by a well-defined step-terrace structure. The surface morphology of the c and r plane sapphire substrate are shown in $2\ \mu\text{m} \times 2\ \mu\text{m}$ AFM images (Figure 62). The characteristics parameters of c and r plane sapphire substrates used in this investigation are calculated from AFM images and listed in Table 7. The inset RHEED images for both surfaces show narrow streaks and kikuchi lines, which confirmed each substrate's flatness and cleanliness.

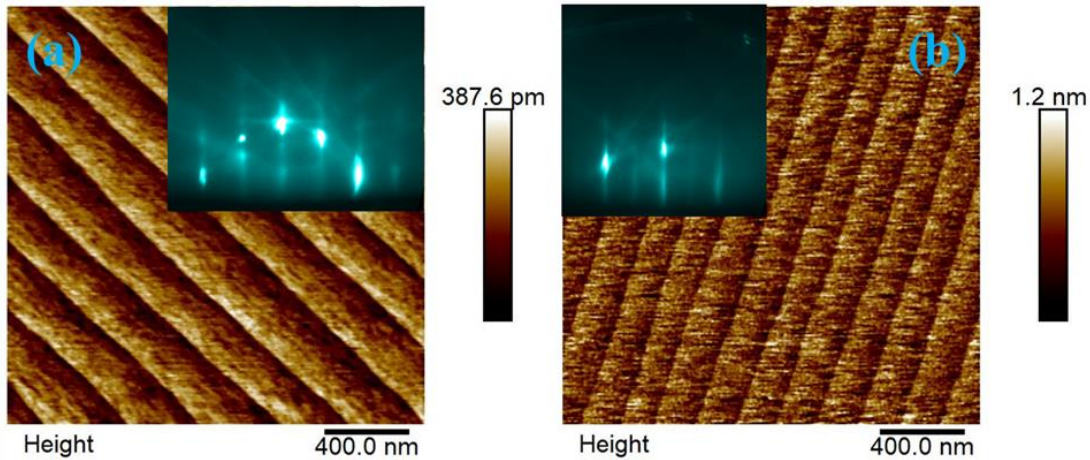


Figure 62: AFM images of (a) c plane and (b) r plane sapphire substrates. Inset shows the substrate RHEED just before the growth.

Table 7: Step height, terrace width, and unintentional miscut angle of c and r plane substrates are listed.

Substrates	Step height (nm)	Terrace width (nm)	Unintentional miscut angle (degree)
C plane	0.22	236	0.06
R plane	0.76	198	0.2

4.4.1 Comparison of GaAs growth on c and r-plane sapphire

To compare the GaAs growth on c and r plane sapphire substrates, two samples, C-600, and R-600, were grown at $T_g = 600^\circ\text{C}$. The nominal thickness was 10 nm, and the thickness was calibrated for homoepitaxial GaAs (100). The growth conditions were identical for both samples. For the surface morphology study, we have performed AFM measurements, and the AFM images are shown in Figure 63 (a, b). The 3D islands are observed for both samples indicate the direct growth of GaAs on both c and r plane sapphire substrate that follow VW or 3D growth mode. High lattice mismatch and dissimilar crystal structure in both cases promote 3D growth. From 2×2 AFM images of both samples, the island's height, density, and volume of GaAs material deposited are listed in Table 8. The higher surface energy of r- plane sapphire than the c-plane sapphire enhances GaAs' interaction on the r plane sapphire, which has increased GaAs island's density in the r-plane. Basically, the diffusion and ripening of GaAs islands is slower on r plane sapphire substrate. Phi scans of the GaAs (220) crystal plane of both samples are shown in Figure 63 (c). The arrow signs indicate GaAs (220) peaks of the C-600 sample. The sharp GaAs (220) peaks are from the R-600 sample, whereas peaks are broad in C-600. The sharp peaks of the R-600 sample indicate a well-defined in-plane correlation between film and substrates as opposed to the C-600 sample, where the weak in-plane correlation is observed. Moreover, six peaks are observed in the phi scan

of the C-600 sample which are separated by 60° degrees to each other. Six peaks indicate six-fold symmetry where three primary domains and three rotated twins are separated by 120° . In the R-600 sample, six peaks corresponding to GaAs (220) are also observed, but these peaks are not exactly separated by 60° . This indicates two different primary domains of [111] oriented crystals that maintain two different in-plane crystal orientation relationships with the r-plane sapphire substrate. The equal intensity of both types of peaks shows that both orientation relationships are equally preferable. Inset RHEED images are after the growth of GaAs from C-600 and R-600 [39]. Two different RHEED patterns are observed for two samples. For the C-600 RHEED image, rings and spots are observed. The RHEED image rings indicate the growth film is in weak in-plane correlation with the substrate, which is also confirmed from the XRD result, whereas the spotty pattern indicates the 3D growth mode. Meanwhile, only spots without a ring pattern are observed in the RHEED image of the R-600 sample. Therefore, GaAs' better in-plane relationship with r plane sapphire substrate than c plane sapphire substrate is observed. All results are consistent with the expectations based on the equation.

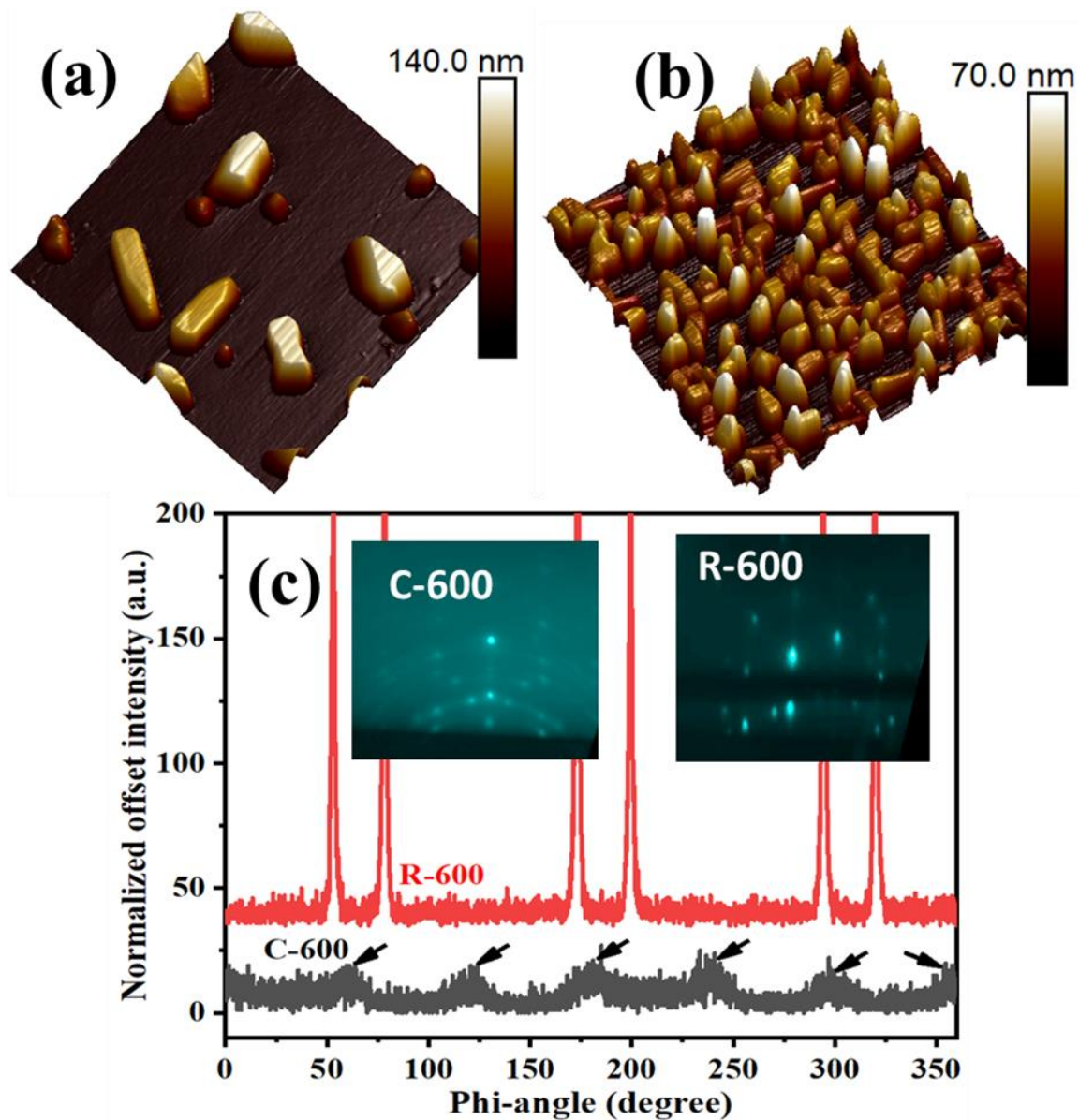


Figure 63: AFM Surface morphology on $2\ \mu\text{m} \times 2\ \mu\text{m}$ scan area of 10 nm GaAs growth on (a) c-plane (C-600) and (b) r-plane sapphire substrate (R-600); (c) Phi-scans of both samples, arrows (red for R-600 and black for C-600) showing GaAs (220) peaks, corresponding RHEED images after the growth are shown in the inset of figure.

Table 8: Island height, density, and total volume on $2\ \mu\text{m} \times 2\ \mu\text{m}$ AFM scan area.

Sample ID	Average Height (nm)	Density (cm^{-2})	Volume of 3D islands (m^3)
C-600	85	4.25×10^8	4×10^{-20}
R-600	40	4.35×10^9	4.3×10^{-20}

To confirm the out of plane orientation, we have performed the symmetric ω - 2Θ scans as shown in Figure 64. During the growth of GaAs on c-plane sapphire the crystal follows only [111] growth direction, whereas GaAs crystal follows both [111] and [220] growth direction on r-plane sapphire substrate. A higher angle tail in the GaAs (111) peak for R-600 is also observed, perhaps due to the strain difference in the two orientations of GaAs observed in phi-scan.

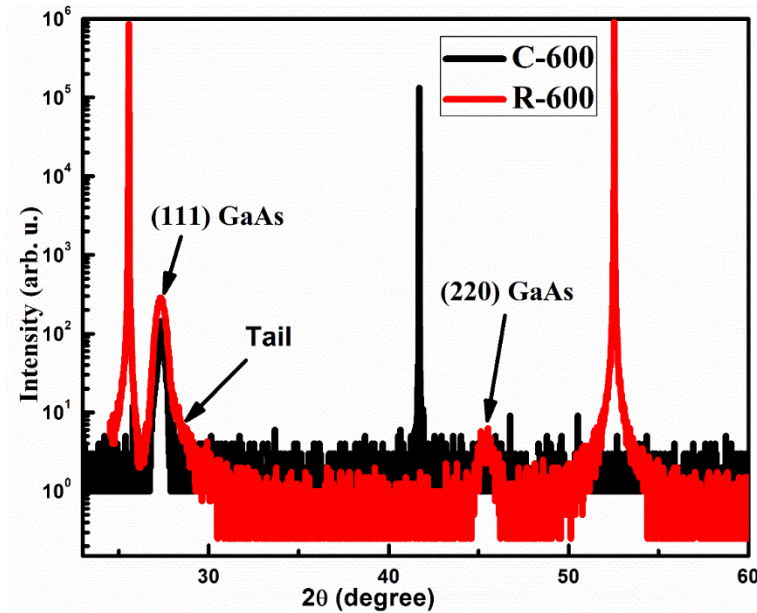


Figure 64: XRD omega-2theta scan of C-600 and R-600. Sharp and intense peaks are related to sapphire substrates.

4.4.2 Effect of growth temperature on GaAs/r-plane sapphire

The growth temperature influences the diffusion length of deposited adatoms on the substrate surface. At higher growth temperatures, adatoms experience more energy, and the diffusion length increases. Therefore, it is essential to study the effect of growth temperature on surface morphology and crystal quality. We grew four samples at four different growth temperature 500°C (R-500), 600°C (R-600), 650°C (R-650), and 700°C (R-700). The nominal thickness of GaAs was

10 nm for each sample. At 700°C, we observed no deposition of GaAs on r plane sapphire substrate. However, the surface morphology and crystal quality were investigated by the deposited GaAs at 500°C, 600°C, and 650°C growth temperatures. The surface morphologies of these three samples are shown in Figure 65.

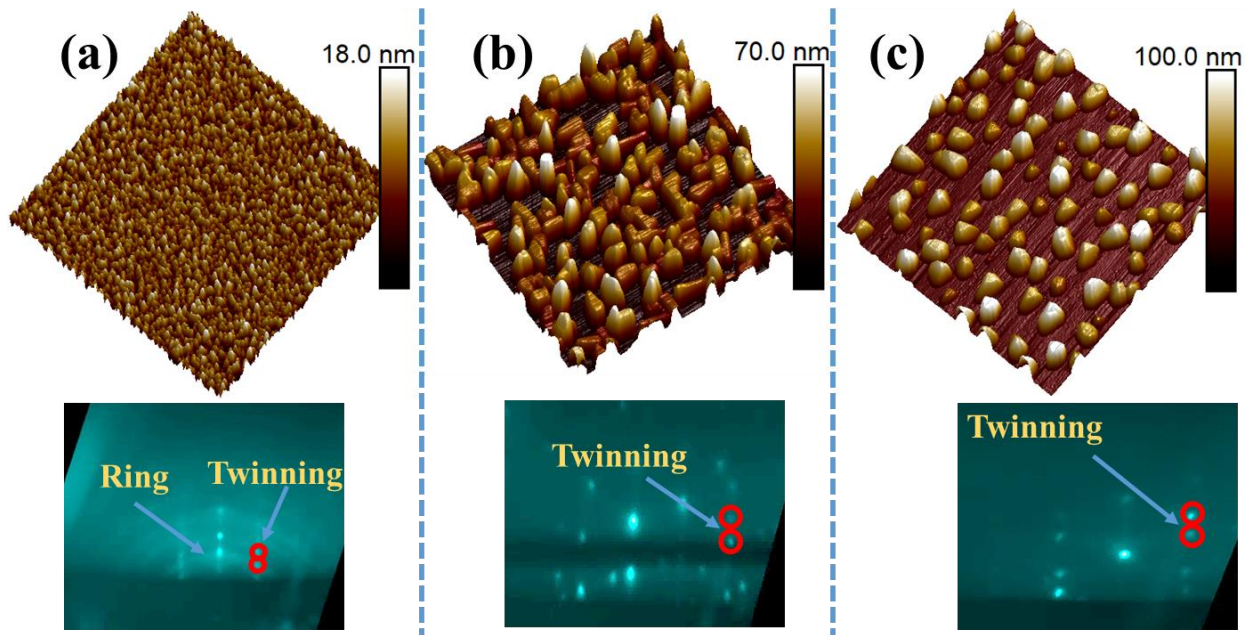


Figure 65: AFM and RHEED of (a) R-500 (b) R-600 (c) R-650.

From the AFM images, the best surface coverage is observed for the sample R-500. The 3D islands are observed for all samples. The islands size and density are listed in Table 9. The size of islands increases, and the density of the islands decrease with increasing growth temperature. These results are consistent with ripening [175], [176]. Three RHEED images of three samples are taken just after the growth. The ring pattern in the RHEED image is observed for R-500, indicating a weak in-plane correlation between the film and the substrate. The ring pattern vanishes with increasing growth temperature, and spotty RHEED images are observed for R-600 and R-650. The twinning is observed in the RHEED images of both samples R-600 and R-650.

Table 9: Growth temperature, GaAs Island height and density for three GaAs/r-plane sapphire samples.

Sample ID	Growth Temperature (°C)	Height (nm)	Density (/cm ²)
R-500	500	9	NA
R-600	600	40	4.35 x 10 ⁹
R-650	650	52.6	3.4 x 10 ⁹

The symmetric ω -2 Θ scans of three samples are shown in Figure 66 (a). Single crystallinity of GaAs on r plane sapphire substrate is observed for samples R-500 and R-650. Meanwhile, two crystal orientations: (111) and (110) are observed for the sample R-600. The phi scans of the GaAs (220) crystal plane for three samples are shown in Figure 66 (b). The in-plane correlation between film and substrate remains invariant with the growth temperature. From the phi scan, we observed the higher growth temperature improves the in-plane correlation. The phi scan is broad and diffused for the sample (R-500) growth at low temperature, indicating the weak in-plane correlation between film and substrate, and this result is also in agreement with RHEED. The sharp and well define phi scans are observed for the samples (R-600 and R-650) growth at high temperature. Therefore, the high growth temperature is necessary for the better in-plane correlation between GaAs film and r-plane sapphire substrate.

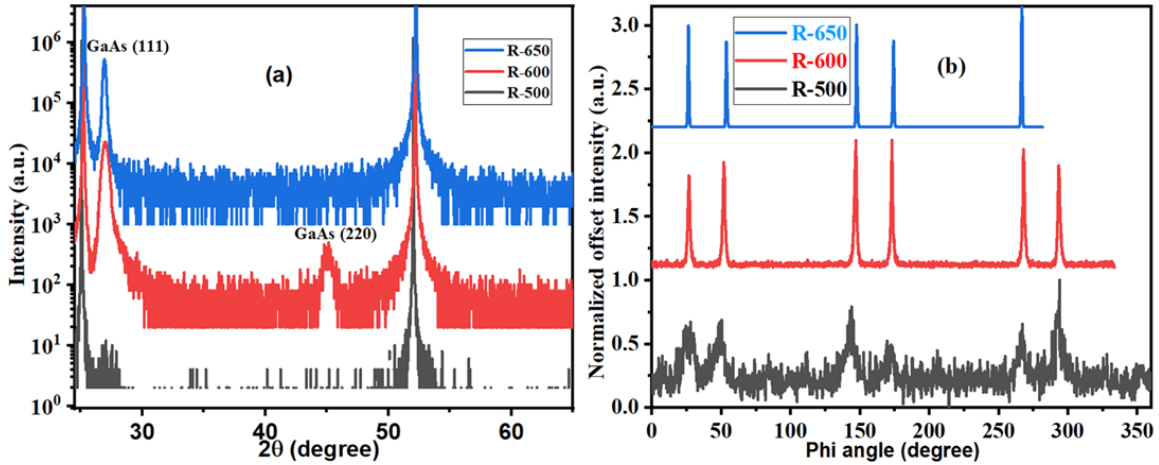


Figure 66: (a) Omega-2theta scan of R-500, R-600 and R650; (b) phi-scan of R-600 and R-650.

4.4.3 Introduction of AlAs layer

At different growth temperatures, the direct growth of GaAs does not wet the r plane sapphire substrate very well. During the growth of GaAs on c-plane sapphire, we observed a thin nucleation layer of AlAs which improved the chemical interaction and the quality of the GaAs film. Therefore, we are encouraged and motivated to introduce a thin 5 nm AlAs as a nucleation layer before the growth of GaAs on r plane sapphire. Three different samples are grown with the presence of AlAs at three different arsenic fluxes: 1×10^{-6} (RA-1), 3.5×10^{-6} (RA-3.5), and 6×10^{-6} (RA-6). The growth temperature $T_g = 600^\circ\text{C}$ was fixed for all samples. The surface morphologies of these samples are shown in AFM images (Figure 67). The highly dense 3D islands are observed for all three samples. The root mean square surface roughness of the samples was measured from the AFM images. The surface roughness of these samples is increased with increasing arsenic partial pressure, and the roughness values are 2.53 nm (RA-1), 2.86 nm (RA-3.5), and 3.68 nm (RA-6). The presence of AlAs improves the wetting of the substrate than the direct growth of GaAs. This is consistent with our observation on the c-plane sapphire substrate. The wetting of the

substrate improves with the presence of AlAs because of the higher bond strength of Al-O (502 kJ/mol) compared to Ga-O (374 kJ/mol) and As-O (374 kJ/mol) [114].

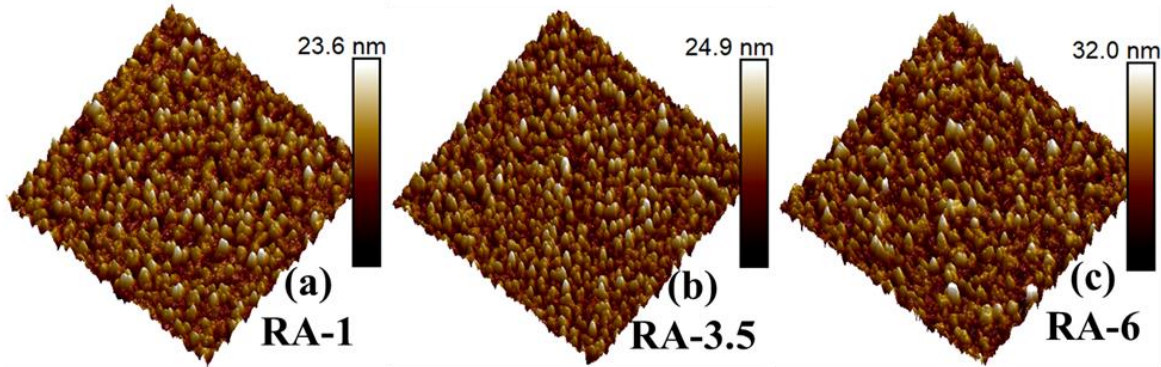


Figure 67: AFM surface morphology of (a) RA-1 (b) RA-3.5 (c) RA-6.

Figure 68 (a) shows the out-of-plane measurements of these three samples. Single crystallinity is observed for all three samples, and the out-of-plane orientation is GaAs (111). On the right side of the GaAs (111) peak, we have observed a clear peak instead of a tail that was observed for direct growth of GaAs on r plane sapphire. The higher angle peak arises from the tensile strain of GaAs/AlAs material. The phi scan of GaAs (220) and r plane sapphire are performed to investigate the in-plane correlation between substrate and film.

The GaAs have a zinc blend crystal structure. Ideally, in the phi scan, the (220) crystal plane of GaAs shows three equally separated peaks representing three-fold symmetry. There are six equally separated peaks observed with the presence of 60° twins. However, in this case, the phi scan of GaAs (220) gives 12 distinct peaks, which is not typical for a cubic zinc blende system (shown in Figure 68 (b)). These 12 peaks arise from the two major orientations. The two major orientations are shifted by approximately $\pm 14^\circ$ with respect to the 0006 reflections of the r-plane sapphire. The 60° rotated twins of both orientations produce total 12 (220) peaks. The inset pole figure also

shows a total of 12 reflection spots which is consistent with the phi measurement. Among 12 spots six are brighter than the other six.

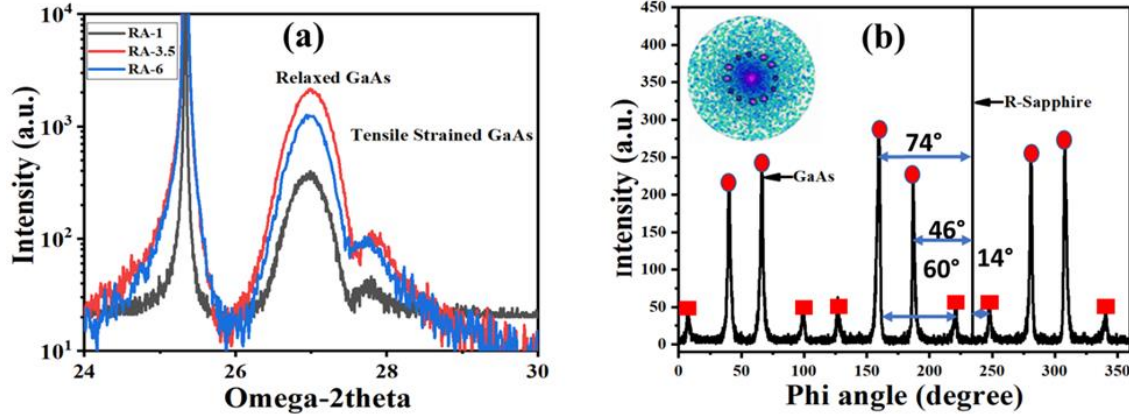


Figure 68: (a) Omega-2theta scan and (b) phi-scan of RA-1, twin peaks are denoted by rectangles, angles between different types of peaks are shown in the figure. Pole figure of the same sample is shown in the inset with sample tilt ranging from 0-70°.

In Figure 69, the major two orientations are depicted by two hexagons O1 and O2. Atomic distances are to the scale with small errors. The 110 axes of GaAs of these two orientations make an angle of approximately $\pm 14^\circ$ with respect to the [100] in-plane direction of r-plane sapphire. It is possible that initially, with smaller coverage of GaAs, only one orientation of GaAs existed where [100] in-plane direction of sapphire was aligned to [110] in-plane direction of GaAs. In other words, the GaAs hexagon was sitting on seed hexagon (shown by green dashed lines in

Figure 69). As the coverage of GaAs increases, the strain also increases, and the initial orientation is splitted in two orientations O1 and O2, by a 14° twist to minimize the strain.

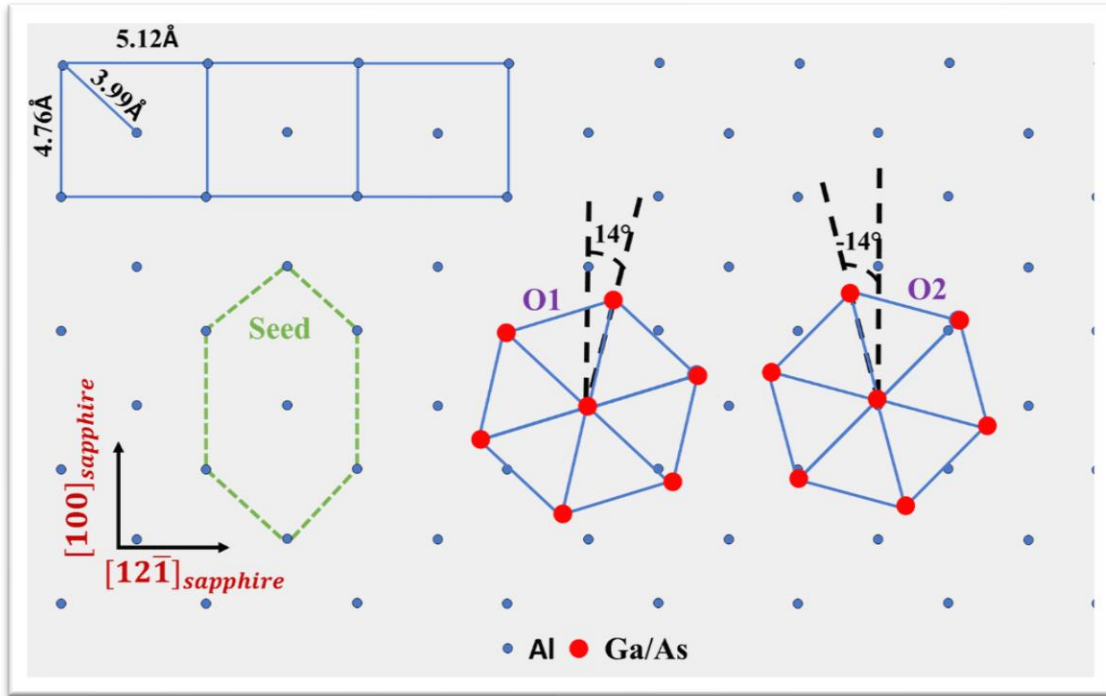


Figure 69: Arrangement of Al atoms in r plane sapphire (blue dots) and two possible in-plane orientations of GaAs separated by approximately 28° .

Chapter 5: Conclusions and Future work

5.1. Conclusions

The highly dissimilar material system of GaAs on c and r-plane sapphire has been grown. The direct growth of GaAs on both substrates are compared. The 3D growth mode and poor wetting of both substrates are observed. Due to the higher surface energy of r plane sapphire, the interaction between GaAs films and r-plane sapphire is better than c-plane sapphire. A weak in-plane correlation between substrate and film, and the formation of twin structures is observed in c-plane sapphire substrates. Two in-plane correlations are observed for GaAs films with r-plane sapphire, which is $\sim 28^\circ$ apart, irrespective of growth temperatures. The introduction of a thin AlAs nucleation layer between the sapphire substrates (c and r-plane) and GaAs film, improved the wetting of the surfaces. The improvement of the wetting of the substrates is explained by the higher bond strength of Al-O. The observed twin ratio reduction in c-plane sapphire is likely correlated to the coalescence of small AlAs 3D islands. To uncover the control of twinning, we investigated the role of the starting substrate on nucleation by examining the pre-growth substrate treatment on the GaAs growth. The better heterointerface formation and improved surface morphology is observed in the case of well-defined c-plane step-terrace substrate surface than corrugated and weakly defined step-terrace substrate. Likewise, in-situ annealing, and growth temperature influenced the twin formation and GaAs surface morphology. In-situ annealing was very effective to reduce the twinning. We were able to reduce the GaAs twin volume less than 2% by in-situ annealing on c-plane sapphire substrate.

Two-step growth was employed to investigate the effectiveness of LT GaAs layer on the quality of GaAs buffer on c-plane sapphire. The LT GaAs, at the early stage of growth, results in smooth

surface morphology. Pyramidal mounds and randomly shaped pits are also observed on the surface. Ehrlich-Schwöbel (ES) barriers and adatom motion in the presence of stacking faults are responsible for the formation of pyramids, while the pits are attributed to thermal etching by Ga droplets which form due to the lower sticking coefficient of arsenic on a GaAs (111)A surface. Compressively strained GaAs is observed without LT GaAs layer from the XRD omega-2theta scan and Raman measurements which matches our speculation on the atomic arrangement. The GaAs film was almost twin free. The HRTEM confirmed abrupt interface between film and substrate with very defects mostly confined near film/substrate interface. Two different regions of different quality materials are confirmed by HRTEM and rocking curves. Together, these observations indicate that the GaAs buffer with the LT layer is effective in achieving high-quality GaAs on c-plane sapphire.

The thickness of the GaAs film was improved by reducing the growth temperatures on c-plane sapphire. At the low growth temperature, the density of truncated pyramids is increased. The dissociation of Frank sessile dislocation generates either pyramids or truncated pyramids depend on the stacking fault energy on the three {111} planes. We were able to get the RT PL from the GaAs/sapphire system. Microdisk lasers were fabricated after getting high quality and RT PL of GaAs. The spontaneous emission was observed from the micro-PL measurement. The higher surface roughness can be the possible reason for not getting the lasing from the GaAs on c-plane sapphire systems.

5.2. Future work

High-quality GaAs film on c-plane sapphire substrate shows the significant potential of GaAs/c-plane sapphire system for integrated microwave photonics. Still there are scopes for the improvement of the crystal quality and surface roughness of the GaAs film. The following study could be focused on making GaAs/sapphire as a platform of integrated microwave photonic systems.

The effectiveness of the strained layer superlattice as a defect layer to improve the surface roughness of GaAs film on c-plane sapphire substrates should be further investigated. The AlGaAs/GaAs or InGaAs/GaAs strained layer superlattices will be employed to reduce the defects at the interface by bending and coalescence. After getting a smooth surface of GaAs, we will be able to fabricate laser, modulator, waveguide, photodiode, and RF circuits for the integrated microwave photonics.

The influences of two-step growth, multiple annealing, and strained layer superlattice on GaAs film on r-plane sapphire should be investigated. We are optimistic that the combined effects of two-step growth, multiple annealing, and strained layer superlattice will result in a quality GaAs surface as demonstrated for GaAs on c-plane sapphire. After getting a high quality and smooth surface of GaAs on r-plane sapphire, we will take the advantage of SOS CMOS technology to integrate optoelectronic devices.

References

- [1] J. Capmany and D. Novak, "Microwave photonics combines two worlds," *Nat. Photonics*, vol. 1, no. 6, pp. 319–330, 2007.
- [2] J. S. Fandiño, P. Muñoz, D. Doménech, and J. Capmany, "A monolithic integrated photonic microwave filter," *Nat. Photonics*, vol. 11, no. 2, pp. 124–129, 2017.
- [3] J. Yao, "Photonic generation of microwave arbitrary waveforms," *Opt. Commun.*, vol. 284, no. 15, pp. 3723–3736, 2011.
- [4] D. Marpaung and C. Roeloffzen, "Integrated microwave photonics for phase modulated systems," *2012 IEEE Photonics Conf. IPC 2012*, pp. 84–85, 2012.
- [5] A. J. Seeds, "Microwave photonics," *IEEE Trans. Microw. Theory Tech.*, vol. 50, no. 3, pp. 877–887, 2002.
- [6] K. J. Williams, "Microwave photonics," *Conf. Proc. - Int. Conf. Indium Phosphide Relat. Mater.*, vol. 27, no. 3, pp. 212–214, 2012.
- [7] C. Cox, "Techniques and performance of intensity-modulation direct-detection analog optical links," *IEEE Trans. Microw. Theory Tech.*, vol. 45, no. 8 PART 2, pp. 1375–1383, 1997.
- [8] E. I. Ackerman *et al.*, "Signal-to-noise performance of two analog photonic links using different noise reduction techniques," *IEEE MTT-S Int. Microw. Symp. Dig.*, pp. 51–54, 2007.
- [9] J. D. McKinney, M. Godinez, V. J. Urick, S. Thaniyavarn, W. Charczenko, and K. J. Williams, "Sub-10-dB noise figure in a multiple-GHz analog optical link," *IEEE Photonics Technol. Lett.*, vol. 19, no. 7, pp. 465–467, 2007.
- [10] D. Jäger and A. Stöhr, "Microwave Photonics – From Concepts to Applications," *Architecture*, no. December, pp. 1–4, 2005.
- [11] D. Marpaung, J. Yao, and J. Capmany, "Integrated microwave photonics," *Nat. Photonics*, vol. 13, no. 2, pp. 80–90, 2019.
- [12] X. Xu, M. Tan, J. Wu, R. Morandotti, A. Mitchell, and D. J. Moss, "Microcomb-Based Photonic RF Signal Processing," *IEEE Photonics Technol. Lett.*, vol. 31, no. 23, pp. 1854–1857, 2019.
- [13] M. Smit *et al.*, "An introduction to InP-based generic integration technology," *Semicond. Sci. Technol.*, vol. 29, no. 8, 2014.
- [14] L. M. Augustin *et al.*, "InP-Based Generic Foundry Platform for Photonic Integrated

- Circuits,” *IEEE J. Sel. Top. Quantum Electron.*, vol. 24, no. 1, 2018.
- [15] W. Zhang and J. Yao, “Silicon-based integrated microwave photonics,” *IEEE J. Quantum Electron.*, vol. 52, no. 1, 2016.
- [16] S. Ibrahim *et al.*, “Demonstration of a fast-reconfigurable silicon CMOS optical lattice filter,” *Opt. Express*, vol. 19, no. 14, p. 13245, 2011.
- [17] K. Wörhoff, R. G. Heideman, A. Leinse, and M. Hoekman, “TriPleX: A versatile dielectric photonic platform,” *Adv. Opt. Technol.*, vol. 4, no. 2, pp. 189–207, 2015.
- [18] J. F. Bauters *et al.*, “Planar waveguides with less than 01 dB/m propagation loss fabricated with wafer bonding,” *Opt. Express*, vol. 19, no. 24, p. 24090, 2011.
- [19] X. Ji *et al.*, “Ultra-low-loss on-chip resonators with sub-milliwatt parametric oscillation threshold,” *Optica*, vol. 4, no. 6, p. 619, 2017.
- [20] D. Pérez *et al.*, “Multipurpose silicon photonics signal processor core,” *Nat. Commun.*, vol. 8, no. 1, pp. 1–9, 2017.
- [21] C. G. H. Roeloffzen *et al.*, “Low-loss si3n4 triplex optical waveguides: Technology and applications overview,” *IEEE J. Sel. Top. Quantum Electron.*, vol. 24, no. 4, 2018.
- [22] J. Kischkat *et al.*, “Mid-infrared optical properties of thin films of aluminum oxide, titanium dioxide, silicon dioxide, aluminum nitride, and silicon nitride,” *Appl. Opt.*, vol. 51, no. 28, pp. 6789–6798, 2012.
- [23] S. K. Saha *et al.*, “Crystalline GaAs Thin Film Growth on a c-Plane Sapphire Substrate,” *Cryst. Growth Des.*, vol. 19, no. 9, pp. 5088–5096, 2019.
- [24] S. K. Saha *et al.*, “GaAs epitaxial growth on R-plane sapphire substrate,” *J. Cryst. Growth*, vol. 548, no. August, p. 125848, 2020.
- [25] M. Yamaguchi, A. Yamamoto, M. Tachikawa, Y. Itoh, and M. Sugo, “Defect reduction effects in GaAs on Si substrates by thermal annealing,” *Appl. Phys. Lett.*, vol. 53, no. 23, pp. 2293–2295, 1988.
- [26] D. S. Abramkin *et al.*, “Influence of a Low-Temperature GaAs Dislocation Filter on the Perfection of GaAs/Si Layers,” *Optoelectron. Instrum. Data Process.*, vol. 54, no. 2, pp. 181–186, 2018.
- [27] N. A. El-Masry, J. C. Tarn, and N. H. Karam, “Interactions of dislocations in GaAs grown on Si substrates with InGaAs-GaAsP strained layered superlattices,” *J. Appl. Phys.*, vol. 64, no. 7, pp. 3672–3677, 1988.
- [28] J. S. Blakemore, “Semiconducting and other major properties of gallium arsenide,” *J. Appl.*

- Phys.*, vol. 53, no. 10, 1982.
- [29] N. Moll, A. Kley, E. Pehlke, and M. Scheffler, “GaAs equilibrium crystal shape from first principles,” *Phys. Rev. B - Condens. Matter Mater. Phys.*, vol. 54, no. 12, pp. 8844–8855, 1996.
- [30] K. Seeger, *Semiconductor Physics*, 9th ed. Springer, 1991.
- [31] J. W. and S. Sze, S.M., *physics of Semiconductor Devices*. .
- [32] V. Dobrovinskaya, E. R.; Lytvynov, L. A; Pischik, *Sapphire: Material, Manufacturing, Applications*. Springer Science + Business Media, 2009.
- [33] F. Cuccureddu *et al.*, “Surface morphology of c-plane sapphire (α -alumina) produced by high temperature anneal,” *Surf. Sci.*, vol. 604, no. 15–16, pp. 1294–1299, 2010.
- [34] R. Chandrasekaran, A. S. Ozcan, D. Deniz, K. F. Ludwig, and T. D. Moustakas, “Growth of non-polar (1120) and semi-polar (1126) AlN and GaN films on the R-plane sapphire,” *Phys. Status Solidi Curr. Top. Solid State Phys.*, vol. 4, no. 5, pp. 1689–1693, 2007.
- [35] P. Vogt, A. Trampert, M. Ramsteiner, and O. Bierwagen, *Domain matching epitaxy of cubic In2O3 on r-plane sapphire*, vol. 212, no. 7. 2015.
- [36] V. Cimalla *et al.*, “Growth of cubic InN on r-plane sapphire,” *Appl. Phys. Lett.*, vol. 83, no. 17, pp. 3468–3470, 2003.
- [37] T. Lei, K. F. Ludwig, and T. D. Moustakas, “Heteroepitaxy, polymorphism, and faulting in GaN thin films on silicon and sapphire substrates,” *J. Appl. Phys.*, vol. 74, no. 7, pp. 4430–4437, 1993.
- [38] J. M. Chauveau, P. Venúgùs, M. Laügt, C. Deparis, J. Zuniga-Perez, and C. Morhain, “Interface structure and anisotropic strain relaxation of nonpolar wurtzite (11 2- 0) and (10 1- 0) orientations: ZnO epilayers grown on sapphire,” *J. Appl. Phys.*, vol. 104, no. 7, 2008.
- [39] R. Kumar *et al.*, “GaAs Layer on c-plane Sapphire for Light Emitting Sources,” *Appl. Surf. Sci.*, p. 148554, 2020.
- [40] A. Biermanns, “X-ray diffraction from single GaAs nanowires,” 2012.
- [41] Yu.B.Bolkhovityanov and O.P.Pchelyakov, “GaAs epitaxy on Si substrates:modern status of research and engineering,” *Uspekhi Fiz. Nauk*, vol. 51, no. 5, pp. 437–456, 2008.
- [42] C. C. R. Lorraine F. Francis, Bethanie J H Stadler, *Materials Processing: A Unified Approach to Processing of Metals, Ceramics and Polymers*. Elsevier Inc., 2016.
- [43] E. R. S. C.L.Claeys, *Stress-induced Defect Generation*. Elsevier, 2016.

- [44] P. Parajuli *et al.*, “MICROSTRUCTURAL EVOLUTION AND ATOMIC-LEVEL SEGREGATION IN METALLIC ALLOY FILMS : AN APPROACH TOWARDS GRAIN BOUNDARY ENGINEERING by Presented to the Graduate Faculty of The University of Texas at San Antonio In Partial Fulfillment Of the Requirements For t,” no. May 2019.
- [45] Y. Wang, W. Chen, B. Wang, and Y. Zheng, “Ultrathin ferroelectric films: Growth, characterization, physics and applications,” *Materials (Basel)*., vol. 6, no. 9, pp. 6377–6485, 2014.
- [46] F. Wu, “Planar Defects in Metallic Thin Film Heterostructures,” no. April, 2014.
- [47] M. S. Muthuvalu and J. Sulaiman, “Journal of Fundamental Sciences,” vol. 6, no. 2, pp. 104–110, 2010.
- [48] S. P. Minor, “Growth of Indium Nitride Quantum Dots by Molecular Beam Epitaxy by,” 2019.
- [49] K. Hermann, *Crystallography and Surface Structure: An Introduction for Surface Scientists and Nanoscientists*. John Wiley & Sons, 2017.
- [50] N. Kaiser, *Review of the fundamentals of thin-film growth*. 2002.
- [51] D. F. and S. Thin Film Materials: Stress, *Thin Film Materials: Stress, Defect Formation and Surface evolution*. Cambridge University Press, 2004.
- [52] John A. Venables, *Introduction to Surface and Thin Film Processes*. Cambridge University Press, 2000.
- [53] Robert S. Feigelson, *Handbook of Crystal Growth*. Elsevier, 2015.
- [54] C.-Y. Chou, “III-V Semiconductor Materials Grown by Molecular Beam Epitaxy for Infrared and High-Speed Transistor Applications,” 2016.
- [55] T. A. Morgan, “Self-Assembled Barium Titanate Nanoscale Films by Molecular Beam Epitaxy,” 2018.
- [56] R. B. Lewis, “Molecular Beam Epitaxy Growth Technology and Properties of GaAsBi Alloys,” 2014.
- [57] A. V. Vasev, M. A. Putyato, and V. V. Preobrazhenskii, “Some geometrical aspects of diffracted waves formation on a reconstructed crystal face at RHEED,” *Surf. Sci.*, vol. 677, pp. 306–315, 2018.
- [58] B. Müller and M. Henzler, “SPA-RHEED - A novel method in reflection high-energy electron diffraction with extremely high angular and energy resolution,” *Rev. Sci. Instrum.*, vol. 66, no. 11, pp. 5232–5235, 1995.

- [59] J. M. Van Hove, P. Pukite, P. I. Cohen, and C. S. Lent, "RHEED streaks and instrument response," *J. Vac. Sci. Technol. A Vacuum, Surfaces, Film.*, vol. 1, no. 2, pp. 609–613, 1983.
- [60] A. Fluri, "Metal Oxide-Based Thin Film Structures," pp. 109–132, 2018.
- [61] M. O. Steen, *Molecular Beam Epitaxy*. Elsevier, 2018.
- [62] S. Abdulrahman and A. Abdulrahman, "ANALYSIS OF CuCl THIN-FILM DEPOSITION AND GROWTH BY CLOSE-SPACE SUBLIMATION," 2018.
- [63] Z. L. Wang, "Reflection high-energy electron diffraction," *Reflect. Electron Microsc. Spectrosc. Surf. Anal.*, pp. 31–59, 2010.
- [64] G. L. Price, "Reflection High Energy Electron Diffraction," pp. 307–318, 2003.
- [65] S. Johnson, "In situ temperature control of molecular beam epitaxy growth using band-edge thermometry," *J. Vac. Sci. Technol. B Microelectron. Nanom. Struct.*, vol. 16, no. 3, p. 1502, 1998.
- [66] I. Farrer, J. J. Harris, R. Thomson, D. Barlett, C. A. Taylor, and D. A. Ritchie, "Substrate temperature measurement using a commercial band-edge detection system," *J. Cryst. Growth*, vol. 301–302, no. SPEC. ISS., pp. 88–92, 2007.
- [67] R. N. Sacks, D. Barlett, C. A. Taylor, and J. Williams, "Growth related interference effects in band edge thermometry of semiconductors," *J. Vac. Sci. Technol. B Microelectron. Nanom. Struct.*, vol. 23, no. 3, p. 1247, 2005.
- [68] M. Aliofkhaezai, *Comprehensive Materials Processing*. Elsevier, 2014.
- [69] M. Farré, *Comprehensive Analytical Chemistry*. 2012.
- [70] B. S. Hameed, *Nanomaterials in Chromatography*. Elsevier, 2018.
- [71] Y. F. Dufrêne, "Atomic force microscopy, a powerful tool in microbiology," *J. Bacteriol.*, vol. 184, no. 19, pp. 5205–5213, 2002.
- [72] Y. F. Dufrêne *et al.*, "Imaging modes of atomic force microscopy for application in molecular and cell biology," *Nat. Nanotechnol.*, vol. 12, no. 4, pp. 295–307, 2017.
- [73] R. Splinter, "Action potential transmission and volume conduction," *Handb. Phys. Med. Biol.*, vol. 56, no. 9, pp. 5-1-5–9, 2010.
- [74] G. Zeng, Y. Duan, F. Besenbacher, and M. Dong, "Nanomechanics of Amyloid Materials Studied by Atomic Force Microscopy," *At. Force Microsc. Investig. into Biol. - From Cell to Protein*, 2012.

- [75] A. Kühle, *Advanced Techniques for Assessment Surface Topography*. Elsevier, 2003.
- [76] M. Frentrop *et al.*, “X-ray diffraction analysis of cubic zincblende III-nitrides,” *J. Phys. D. Appl. Phys.*, vol. 50, no. 43, 2017.
- [77] V. Vishwakarma, *Smart Nanoconcretes and Cement-Based Materials*. Elsevier, 2020.
- [78] H. J. Kim, Y. Park, H. Bin Bae, and S. H. Choi, “High-electron-mobility SiGe on sapphire substrate for fast chipsets,” *Adv. Condens. Matter Phys.*, vol. 2015, 2015.
- [79] K. Inaba, S. Kobayashi, K. Uehara, A. Okada, S. L. Reddy, and T. Endo, “High Resolution X-Ray Diffraction Analyses of (La,Sr)MnO₃ZnOSapphire(0001) Double Heteroepitaxial Films,” *Adv. Mater. Phys. Chem.*, vol. 03, no. 01, pp. 72–89, 2013.
- [80] K. Maria; V. Maria, *Polymer Science and Nanotechnology*. Elsevier, 2020.
- [81] P. S. Kumar; K. G. Pavithra; Mu.Naushad, *Nanomaterials for Solar Cell Applications*. Elsevier, 2019.
- [82] C. A. English, *Structural Alloys for Nuclear Energy Applications*. Elsevier, 2019.
- [83] N. G. Orji *et al.*, “TEM calibration methods for critical dimension standards,” *Metrol. Insp. Process Control Microlithogr. XXI*, vol. 6518, p. 651810, 2007.
- [84] B. ThoriharaTomoda, *Biopolymer Membranes and Films*. Elsevier, 2020.
- [85] Maria Kaliva, *Polymer Science and Nanotechnology*. Elsevier, 2020.
- [86] B. Saad Alharthi, “Growth and Characterization of Silicon-Germanium-Tin Semiconductors for Future Nanophotonics Devices,” 2018.
- [87] D. D. L. Pevelen, *Encyclopedia of Spectroscopy and Spectrometry*. Elsevier, 2017.
- [88] J.N.Hilfiker, *Encyclopedia of Modern Optics*. Elsevier, 2005.
- [89] J.N.Hilfiker, *Encyclopedia of Modern Optics*. Elsevier, 2005.
- [90] T. Pham, “Si-based Germanium Tin Photodetectors for Short-Wave and Mid-Wave Infrared Detections Part of the Electronic Devices and Semiconductor Manufacturing Commons,” 2018.
- [91] HuaiyuWang, *Characterization of Biomaterials*. Elsevier, 2013.
- [92] D.W.Grainger, *Comprehensive Biomaterials*. Elsevier, 2011.
- [93] D. K. Schroder, *Semiconductor Material and Device Characterization*,. John Wiley & Sons,

- InC, 2015.
- [94] J. Abraham, *Phytonanotechnology*. Elsevier, 2020.
- [95] F. Wang, *Advanced Nanomaterials for Solar Cells and Light Emitting Diodes*. Elsevier, 2019.
- [96] J. M. Grant, *Investigation of Critical Technologies of Chemical Vapor Deposition for Advanced (Si) GeSn Materials*. 2019.
- [97] S. H. S. Al-Kabi, *Si-Based Germanium Tin Semiconductor Lasers for Optoelectronic Applications*. 2017.
- [98] S. P. Minor, "Plasma-Assisted Molecular Beam Epitaxial Growth of Indium Nitride for Future Device Fabrication," p. 93, 2012.
- [99] A. P. Kirk, *Solar Photovoltaic Cells*. Elsevier, 2015.
- [100] H. Fu, *Nitride Semiconductor Light-Emitting Diodes (LEDs)*. Elsevier, 2018.
- [101] P. C. Grant, *GeSn Thin Film Epitaxy and Quantum Wells for Optoelectronic Devices*. 2018.
- [102] Wei Dou, *High-Sn-content GeSn Alloy towards Room-temperature Mid Infrared Laser*. 2018.
- [103] C. Steve, "The Setup , Design , and Implementation of a Photoluminescence Experiment on Quantum Wells University of Rochester Class of 2014 University of Colorado REU Program Summer 2011," 2014.
- [104] C.L. Claeys, *Materials Science and Materials Engineering*. Elsevier, 2016.
- [105] R. Kumar, A. Bag, P. Mukhopadhyay, S. Das, and D. Biswas, "Comparison of Different Grading Schemes in InGaAs Metamorphic Buffers on GaAs Substrate: Tilt Dependence on Cross-Hatch Irregularities," *Appl. Surf. Sci.*, vol. 357, pp. 922–930, Sep. 2015.
- [106] R. Kumar *et al.*, "Excitation intensity and thickness dependent emission mechanism from an ultrathin InAs layer in GaAs matrix," *J. Appl. Phys.*, vol. 124, no. 23, 2018.
- [107] Y. Park, G. C. King, and S. H. Choi, "Rhombohedral epitaxy of cubic SiGe on trigonal c-plane sapphire," *J. Cryst. Growth*, vol. 310, no. 11, pp. 2724–2731, 2008.
- [108] H. J. Kim, A. Duzik, and S. H. Choi, "Lattice-alignment mechanism of SiGe on Sapphire," *Acta Mater.*, vol. 145, pp. 1–7, 2018.
- [109] C. A. S. and C. J. M. T. P. Humphreys, N. R. Parikh, K. Das, J. B. Posthill, R. J. Nemanich, M. K. SummerVile, "Molecular Beam Epitaxial Growth and Characterization of GaAs on

- Sapphire and Silicon-on-Sapphire Substrates,” *J. Chem. Inf. Model.*, vol. 53, no. 9, pp. 1689–1699, 2013.
- [110] and T. M. A. Koma, K. Sunouchi, “Physics of Semiconductors,” 1985, p. 1465.
- [111] and T. M. A. Koma, K. Sunouchi, *Microelectronic Engineering*. Elsevier, 1984.
- [112] A. Koma, “Van der Waals epitaxy for highly lattice-mismatched systems,” *J. Cryst. Growth*, vol. 201–202, 1999.
- [113] G. Saint-Girons, J. Cheng, P. Regreny, L. Largeau, G. Patriarche, and G. Hollinger, “Accommodation at the interface of highly dissimilar semiconductor/oxide epitaxial systems,” *Phys. Rev. B - Condens. Matter Mater. Phys.*, vol. 80, no. 15, pp. 1–6, 2009.
- [114] Y.-R. Luo, *Comprehensive Handbook of Chemical Bond Energies*. Boca Raton, 2007.
- [115] W. Wegscheider, K. Eberl, G. Abstreiter, H. Cerva, and H. Oppolzer, “Novel relaxation process in strained Si/Ge superlattices grown on Ge (001),” *Appl. Phys. Lett.*, vol. 57, no. 15, pp. 1496–1498, 1990.
- [116] W. Wegscheider, “Effect of compressive and tensile strain on misfit dislocation injection in SiGe epitaxial layers,” *J. Vac. Sci. Technol. B Microelectron. Nanom. Struct.*, vol. 11, no. 3, p. 1056, 1993.
- [117] H. K. T. Maeda, M. Yoshimoto, T. Ohnishi, G. H. Lee, “Orientation-defined molecular layer epitaxy of α -Al₂O₃ thin films,” *J. Cryst. Growth*, vol. 177, no. 1–2, pp. 95–101, 1997.
- [118] I. M. Y. Shun-ichi, K. Shunsuke, F. Masanori, “Self-formed silicon quantum wires on ultrasmooth sapphire substrates,” *Appl. Phys. Lett.*, vol. 71, no. 1409, 1997.
- [119] A. Ohtake and T. A. T. Ito, “As-rich (2 × 2) surface reconstruction on GaAs(111)A,” *Surf. Sci.*, vol. 606, no. 23–24, pp. 1864–1870, 2012.
- [120] D. A. Woolf, Z. Sobiesierski, D. I. Westwood, and R. H. Williams, “The molecular beam epitaxial growth of GaAs/GaAs(111)B: Doping and growth temperature studies,” *J. Appl. Phys.*, vol. 71, no. 10, pp. 4908–4915, 1992.
- [121] A. Kawaharazuka and Y. Horikoshi, “Behavior of Ga atoms deposited on GaAs (111)B and (111)A surfaces,” *J. Cryst. Growth*, vol. 477, pp. 25–29, 2017.
- [122] S. Y. Tong, G. Xu, and W. N. Mei, “Vacancy-buckling model for the (2×2) GaAs(111) surface,” *Phys. Rev. Lett.*, vol. 52, no. 19, pp. 1693–1696, 1984.
- [123] H. Li, Y. Sun, C. Law, B. Visbeck, and F. Hicks, “Reconstructions of the InP(111)A surface,” *Phys. Rev. B - Condens. Matter Mater. Phys.*, vol. 68, no. 8, 2003.

- [124] M. R. Fahy, K. Sato, and B. A. Joyce, “Reflection high-energy electron diffraction intensity oscillations during the growth by molecular beam epitaxy of GaAs (111)A,” *Appl. Phys. Lett.*, vol. 64, no. 2, pp. 190–192, 1994.
- [125] C. D. Yerino, B. Liang, D. L. Huffaker, P. J. Simmonds, and M. L. Lee, “Review Article: Molecular beam epitaxy of lattice-matched InAlAs and InGaAs layers on InP (111)A, (111)B, and (110),” *J. Vac. Sci. Technol. B, Nanotechnol. Microelectron. Mater. Process. Meas. Phenom.*, vol. 35, no. 1, p. 010801, 2017.
- [126] K. Yang and L. J. Schowalter, “Surface reconstruction phase diagram and growth on GaAs(111)B substrates by molecular beam epitaxy,” *Appl. Phys. Lett.*, vol. 60, no. 15, pp. 1851–1853, 1992.
- [127] J. W. Kim, S. Kim, and J. M. Seo, “Surface core-level shift of InSb(111)-2×2,” *Phys. Rev. B - Condens. Matter Mater. Phys.*, vol. 54, no. 7, pp. 4476–4479, 1996.
- [128] D. A. Woolf, D. I. Westwood, and R. H. Williams, “The homoepitaxial growth of GaAs(111)A and (111)B by molecular beam epitaxy: An investigation of the temperature-dependent surface reconstructions and bulk electrical conductivity transitions,” *Semicond. Sci. Technol.*, vol. 8, no. 6, pp. 1075–1081, 1993.
- [129] L. Esposito, S. Bietti, A. Fedorov, R. Nötzel, and S. Sanguinetti, “Ehrlich-Schwöbel effect on the growth dynamics of GaAs(111)A surfaces,” *Phys. Rev. Mater.*, vol. 1, no. 2, 2017.
- [130] Y. Park *et al.*, “Analysis of twin defects in GaAs(111)B molecular beam epitaxy growth,” *J. Vac. Sci. Technol. B Microelectron. Nanom. Struct.*, vol. 18, no. 3, p. 1566, 2000.
- [131] K. Sato, M. R. Fahy, and B. A. Joyce, “The growth of high quality GaAs on GaAs (111)A,” *Jpn. J. Appl. Phys.*, vol. 33, no. 7, pp. L905–L907, 1994.
- [132] Y. Horikoshi, T. Uehara, T. Iwai, and I. Yoshida, “Area selective growth of GaAs by migration-enhanced epitaxy,” *Phys. Status Solidi Basic Res.*, vol. 244, no. 8, pp. 2697–2706, 2007.
- [133] M. Yamaguchi, M. Tachikawa, Y. Itoh, M. Sugo, and S. Kondo, “Thermal annealing effects of defect reduction in GaAs on Si substrates,” *J. Appl. Phys.*, vol. 68, no. 9, pp. 4518–4522, 1990.
- [134] N. C. Patra, S. Bharatan, J. Li, and S. Iyer, “Annealing studies of heteroepitaxial InSbN on GaAs grown by molecular beam epitaxy for long-wavelength infrared detectors,” *J. Appl. Phys.*, vol. 112, no. 8, pp. 2010–2015, 2012.
- [135] N. El-Masry *et al.*, “Defect Reduction in GaAs Epilayers on Si Substrates Using Strained Layer Superlattices,” *MRS Proc.*, vol. 91, pp. 99–103, 1987.
- [136] T. Uehara, T. Iwai, I. Yoshida, and Y. Horikoshi, “Area-selective epitaxial growth of GaAs

- on GaAs(111)A substrates by migration-enhanced epitaxy,” *Japanese J. Appl. Physics, Part 1 Regul. Pap. Short Notes Rev. Pap.*, vol. 46, no. 2, pp. 496–501, 2007.
- [137] N. Gopalakrishnan, K. Baskar, H. Kawanami, and I. Sakata, “Effects of the low temperature grown buffer layer thickness on the growth of GaAs on Si by MBE,” *J. Cryst. Growth*, vol. 250, no. 1–2, pp. 29–33, 2003.
- [138] M. Yamaguchi, M. Sugo, and Y. Itoh, “Misfit stress dependence of dislocation density reduction in GaAs films on Si substrates grown by strained-layer superlattices,” *Appl. Phys. Lett.*, vol. 54, no. 25, pp. 2568–2570, 1989.
- [139] J. W. Z Liliental-Weber, ER Weber, “Heteroepitaxy of GaAs on Si: Methods to decrease the defect density in the epilayer,” no. July, pp. 35–43, 2010.
- [140] C. C. Phua, T. C. Chong, and W. S. Lau, “Improved crystalline quality of molecular beam epitaxy grown gaas-on-si epilayer through the use of low-temperature gaas intermediate layer,” *Jpn. J. Appl. Phys.*, vol. 33, no. 3, pp. L405–L408, 1994.
- [141] N. Chand, R. People, F. A. Baiocchi, K. W. Wecht, and A. Y. Cho, “Significant improvement in crystalline quality of molecular beam epitaxially grown GaAs on Si (100) by rapid thermal annealing,” *Appl. Phys. Lett.*, vol. 49, no. 13, pp. 815–817, 1986.
- [142] M. O. Petrushkov *et al.*, “Impact of LT-GaAs layers on crystalline properties of the epitaxial GaAs films grown by MBE on Si substrates,” *J. Phys. Conf. Ser.*, vol. 741, no. 1, 2016.
- [143] J. Li, G. Miao, Z. Zhang, and Y. Zeng, “Experiments and analysis of the two-step growth of InGaAs on GaAs substrate,” *CrystEngComm*, vol. 17, no. 30, pp. 5808–5813, 2015.
- [144] Yu. B. Bolkhovityanov and O. P. chelyakov, “GaAs epitaxy on Si substrate: Modern status of research an dengineering,” *Uspekhi Fiz. Nauk*, vol. 178, no. 5, p. 459, 2008.
- [145] L. Esposito, S. Bietti, A. Fedorov, R. Nötzel, and S. Sanguinetti, “Ehrlich-Schwöbel effect on the growth dynamics of GaAs(111)A surfaces,” *Phys. Rev. Mater.*, vol. 1, no. 2, pp. 2–9, 2017.
- [146] S. J. Liu, H. Huang, and C. H. Woo, “Schwoebel-Ehrlich barrier: From two to three dimensions,” *Appl. Phys. Lett.*, vol. 80, no. 18, pp. 3295–3297, 2002.
- [147] M. S. Abrahams and C. J. Buiocchi, “Etching of dislocations on the low-index faces of GaAs,” *J. Appl. Phys.*, vol. 36, no. 9, pp. 2855–2863, 1965.
- [148] S. Kanjanachuchai and C. Euaruksakul, “Self-running Ga droplets on GaAs (111)A and (111)B surfaces,” *ACS Appl. Mater. Interfaces*, vol. 5, no. 16, pp. 7709–7713, 2013.
- [149] D. Zeng, W. Jie, T. Wang, J. Zhang, and G. Zha, “Type and formation mechanism of thermal etch pit on annealed (111) CdZnTe surface,” *Thin Solid Films*, vol. 517, no. 9, pp. 2896–

2899, Mar. 2009.

- [150] H. Maki *et al.*, “Control of surface morphology of ZnO (0 0 0 Γ) by hydrochloric acid etching,” *Thin Solid Films*, vol. 411, no. 1, pp. 91–95, 2002.
- [151] R. Kumar and D. Biswas, “Tilt investigation of In(Al,Ga)As metamorphic buffer layers on GaAs (001) substrate: A novel technique for tilt determination,” *Cryst. Res. Technol.*, vol. 51, no. 12, pp. 723–729, Dec. 2016.
- [152] J. P. Bosco, G. M. Kimball, N. S. Lewis, and H. A. Atwater, “Pseudomorphic growth and strain relaxation of α -Zn₃P₂ on GaAs(001) by molecular beam epitaxy,” *J. Cryst. Growth*, vol. 363, pp. 205–210, 2013.
- [153] M. Briceño, J. Kacher, and I. M. Robertson, “Dynamics of dislocation interactions with stacking-fault tetrahedra at high temperature,” *J. Nucl. Mater.*, vol. 433, no. 1–3, pp. 390–396, 2013.
- [154] D. Hull and D. J. Bacon, “Dislocations in Face-centered Cubic Metals,” *Introd. to Dislocations*, no. 110, pp. 85–107, 2011.
- [155] M. Kiritani, “Story of stacking fault tetrahedra,” *Mater. Chem. Phys.*, vol. 50, no. 2, pp. 133–138, 1997.
- [156] Y. Matsukawa and S. J. Zinkle, “Dynamic observation of the collapse process of a stacking fault tetrahedron by moving dislocations,” *J. Nucl. Mater.*, vol. 329–333, no. 1-3 PART B, pp. 919–923, 2004.
- [157] D. Punktfehler and A. Science, “of Stacking Fault,” 1966.
- [158] F. Martin, P. Mural, M.-A. Dubois, and A. Pezous, “ Thickness dependence of the properties of highly c -axis textured AlN thin films ,” *J. Vac. Sci. Technol. A Vacuum, Surfaces, Film.*, vol. 22, no. 2, pp. 361–365, 2004.
- [159] A. C. Diebold, S. W. Steinhauser, R. P. Mariella, J. Marti, F. Reidinger, and R. F. Antrim, “Growth and characterization of GaAs on sapphire (0001) by molecular beam epitaxy,” *Surf. Interface Anal.*, vol. 15, no. 2, pp. 150–158, 1990.
- [160] J. Wang *et al.*, “Extremely Low-Threshold Current Density InGaAs/AlGaAs Quantum-Well Lasers on Silicon,” *J. Light. Technol.*, vol. 33, no. 15, pp. 3163–3169, 2015.
- [161] A. A. Spirina, A. G. Nastovjak, and N. L. Shwartz, “Influence of GaAs substrate properties on the congruent evaporation temperature,” *J. Phys. Conf. Ser.*, vol. 993, no. 1, 2018.
- [162] J. Van De Ven, W. J. A. M. Hartmann, and L. J. Giling, *Photoluminescence studies of defects and impurities in annealed GaAs*, vol. 60, no. 10. 1986.

- [163] A. A. Klochikhin, V. P. Kochereshko, and S. Tatarenko, "Influence of free carriers on exciton ground states in quantum wells," *J. Lumin.*, vol. 154, pp. 310–315, 2014.
- [164] S. Jin, Y. Zheng, and A. Li, "Characterization of photoluminescence intensity and efficiency of free excitons in semiconductor quantum well structures," *J. Appl. Phys.*, vol. 82, no. 8, pp. 3870–3873, 1997.
- [165] H. J. Kim, H. Bin Bae, Y. Park, K. Lee, and S. H. Choi, "Temperature dependence of crystalline SiGe growth on sapphire (0001) substrates by sputtering," *J. Cryst. Growth*, vol. 353, no. 1, pp. 124–128, 2012.
- [166] W. . Dubbelday and K. . Kavanagh, "The growth of SiGe on sapphire using rapid thermal chemical vapor deposition," *J. Cryst. Growth*, vol. 222, no. 1–2, pp. 20–28, Jan. 2001.
- [167] A. Sugimura, T. Hosoi, K. Ishibitsu, and T. Kawamura, "Heteroepitaxial growth of GaAs on sapphire substrates by a three-step method using low pressure MOCVD," *J. Cryst. Growth*, vol. 77, no. 1–3, pp. 524–529, 1986.
- [168] K. Kasai, K. Nakai, and M. Ozeki, "Material and device properties of GaAs on sapphire grown by metalorganic chemical vapor deposition," *J. Appl. Phys.*, vol. 60, no. 1, pp. 1–5, 1986.
- [169] T. P. Humphreys *et al.*, "Heteroepitaxial growth and characterization of GaAs on silicon-on-sapphire and sapphire substrates," *Appl. Phys. Lett.*, vol. 54, no. 17, pp. 1687–1689, 1989.
- [170] T. F. Kuech, A. Segmüller, T. S. Kuan, and M. S. Goorsky, "Growth and properties of thin GaAs epitaxial layers on Al₂O₃," *J. Appl. Phys.*, vol. 67, no. 10, pp. 6497–6506, 1990.
- [171] L. C. Chuang *et al.*, "GaAs nanoneedles grown on sapphire," *Appl. Phys. Lett.*, vol. 98, no. 12, pp. 98–101, 2011.
- [172] J. E. Boschker *et al.*, "Surface reconstruction-induced coincidence lattice formation between two-dimensionally bonded materials and a three-dimensionally bonded substrate," *Nano Lett.*, vol. 14, no. 6, pp. 3534–3538, 2014.
- [173] T. Stirner, J. Sun, and M. Aust, "Ab Initio Hartree-Fock Simulation of R-Plane Sapphire," *Phys. Procedia*, vol. 32, no. August 2010, pp. 635–639, 2012.
- [174] J. Sun, T. Stirner, and A. Matthews, "Structure and surface energy of low-index surfaces of stoichiometric α -Al₂O₃ and α -Cr₂O₃," *Surf. Coatings Technol.*, vol. 201, no. 7 SPEC. ISS., pp. 4205–4208, 2006.
- [175] G. Madras and B. J. McCoy, "Temperature effects during Ostwald ripening," *J. Chem. Phys.*, vol. 119, no. 3, pp. 1683–1693, 2003.

- [176] T. Van Westen and R. D. Groot, “Effect of Temperature Cycling on Ostwald Ripening,” *Cryst. Growth Des.*, vol. 18, no. 9, pp. 4952–4962, 2018.